

POLITECNICO DI TORINO

Corso di Laurea  
in Ingegneria Aerospaziale

Tesi di Laurea Specialistica

Investigation of RANS reliability  
for transonic airfoils



**Relatori:**

Renzo ARINA  
Vincent JAUNET  
Jean-Luc HANTRAIS-GERVOIS  
Marco CARINI  
Didier BAILLY

**Candidato:**

Giovannino CIRULLO

Dicembre 2021



# Acknowledgement

Before proceeding with the discussion, I would like to express my gratitude for all the people have been part of this Master's thesis and university path.

My graditude goes to ONERA, for giving me the opportunity to work in such a dynamic and interesting workplace. I learnt many things, met a lot of beautiful people and I will keep great memories of this experience. I am incredibly grateful to the head of the ACI Unit, Michael Meheut, and my supervisors Didier Bailly, Marco Carini and in particular Jean-Luc Hantrais-Gervois, who carefully followed me throughout this internship. I would also like to thank my academic supervisors, Renzo Arina and Vincent Jaunet, for their help and support.

I would like to give a special recognition to my parents for their tireless support, both human and financial, and all the members of my family, for always being there. Without them, I would not be the person I am today.

I am extremely grateful to Politecnico di Torino for giving me the opportunity to pursue a Double Degree abroad, and ISAE-ENSMA for welcoming me. The last two years have been very intense, formative and unique.

Finally, I am deeply thankful to all the fantastic people I met during my university experience, in Turin and Poitiers, and to those I have known for a lifetime and who have always stayed by my side. Thank you for being my accomplices, each in their own way, in this intense and exciting journey, for better or for worse. There are so many memories running through my head that it is impossible to find the right words to honour them. Thanks for making this achievement incredibly special.

# Contents

<b>1</b>	<b>Introduction</b>	<b>1</b>
1.1	ONERA and Work Environment . . . . .	1
1.2	Internship Objectives . . . . .	3
1.3	Report Structure . . . . .	3
<b>2</b>	<b>Context</b>	<b>4</b>
2.1	Issue . . . . .	4
2.2	Mission . . . . .	5
2.3	State of the Art . . . . .	6
2.3.1	Introduction . . . . .	6
2.3.2	elsA . . . . .	6
2.3.3	ISES . . . . .	8
2.3.3.1	Description . . . . .	8
2.3.3.2	Boundary Condition Treatment . . . . .	9
2.3.3.3	Boundary Layer Formulation . . . . .	9
2.3.4	BIRDIE . . . . .	11
2.3.5	Wind Tunnel Tests . . . . .	13
2.3.6	Adverse Pressure Gradient Effects . . . . .	14
2.3.7	Spalart-Allmaras turbulence model . . . . .	14
2.3.8	Previous Investigations . . . . .	16
2.3.8.1	Introduction . . . . .	16
2.3.8.2	Technical Report 1 . . . . .	16
2.3.8.3	Technical Report 2 . . . . .	16
<b>3</b>	<b>Methodology</b>	<b>19</b>
3.1	Numerical Setup . . . . .	19
3.1.1	elsA . . . . .	19
3.2	Profil_12 Design . . . . .	21
3.2.1	Introduction . . . . .	21
3.2.2	Procedure . . . . .	21
3.2.2.1	Intermediate Airfoil Profil_1 Design . . . . .	21
3.2.2.2	Final Airfoil Profil_12 Design . . . . .	25
3.3	Grid Convergence . . . . .	26
3.3.1	Introduction . . . . .	26
3.3.2	Procedure . . . . .	26
3.3.2.1	Numerical Convergence Criteria . . . . .	26
3.3.2.2	Grids . . . . .	26
3.3.3	Grid Convergence Index . . . . .	26
3.3.4	Far-Field Drag Analysis . . . . .	26
3.4	Reliability mapping of the "pETW" database . . . . .	29
3.4.1	Introduction . . . . .	29
3.4.2	Procedure . . . . .	29
3.4.2.1	Aerodynamic conditions . . . . .	29
3.4.2.2	Choice of $AoA$ . . . . .	29
3.4.2.3	Discrepancy metric $\sigma$ . . . . .	30
3.5	Data Assimilation . . . . .	31
3.5.1	Introduction . . . . .	31
3.5.2	Optimisation Problem 1 . . . . .	31
3.5.3	Optimisation Problem 2 . . . . .	35

3.5.4	Optimisation Problem 3	37
3.5.5	Optimisation Problem 4	38
<b>4</b>	<b>Results</b>	<b>41</b>
4.1	Profil_12 Design	41
4.1.1	Intermediate Airfoil Profil_1 Design	41
4.1.2	Final Airfoil Profil_12 Design	45
4.1.3	Conclusion	46
4.2	Grid Convergence	47
4.2.1	Convergence Results	47
4.2.2	Flow-Field Comparison	47
4.2.3	Aerodynamic Coefficients	48
4.2.4	Grid Convergence Index	48
4.2.5	Field Drag Analysis	49
4.2.6	Conclusion	49
4.3	Reliability mapping of "pETW" database	54
4.3.1	Choice of $AoA$	54
4.3.2	Comparison between experimental and numerical data	54
4.3.3	Conclusion	56
4.4	Data Assimilation	68
4.4.1	Optimisation Problem 1	68
4.4.1.1	Convergence Criterion	68
4.4.1.2	Results	69
4.4.2	Optimisation Problem 2	74
4.4.2.1	Introduction	74
4.4.2.2	Results	74
4.4.3	Optimisation Problem 3	76
4.4.3.1	Introduction	76
4.4.3.2	Results	76
4.4.4	Optimisation Problem 4	79
4.4.4.1	Introduction	79
4.4.4.2	Assimilated Parameters Effects on Flate Plate Simulations	79
4.4.4.3	Results	82
4.4.5	Conclusion	83
<b>5</b>	<b>Conclusion</b>	<b>84</b>

# List of Figures

1.1	View of the historic S1 wind tunnel . . . . .	2
2.1	Exemple of elsA CFD simulation . . . . .	6
2.2	Exemple of ISES computational domain No.1 . . . . .	8
2.3	Exemple of ISES computational domain No.2 . . . . .	9
2.4	Representation of BIRDIE mathematical operations (extracted from [1]) . . . . .	12
	(a) Geometric space definition . . . . .	12
	(b) Definition of a new parameter space . . . . .	12
2.5	Pictures of wind tunnel pETW (from [2]) . . . . .	13
2.6	Turbulence model effects on $C_p$ and $C_f$ distributions . . . . .	18
	(a) Pressure coefficient distribution . . . . .	18
	(b) Skin friction coefficient distribution . . . . .	18
3.1	Exemple of mesh generated by Rizzi method [3] for an elsA RAE2822 airfoil simulation . . . . .	20
	(a) Overview . . . . .	20
	(b) Grid around the airfoil . . . . .	20
	(c) Leading edge details . . . . .	20
	(d) Trailing edge details . . . . .	20
3.2	Initialition of BIRDIE parameters . . . . .	22
	(a) Variations on the airfoil thickness . . . . .	22
	(b) Variations on the airfoil camber-line . . . . .	22
3.3	Meshes used for Profil_1 RANS calculations . . . . .	23
	(a) Coarser mesh for Profil_1 . . . . .	23
	(b) Intermediate mesh for Profil_1 . . . . .	23
	(c) Finer mesh for Profil_1 . . . . .	23
3.4	Example of polar curves of Profil_1 . . . . .	24
	(a) Lift coefficient curve of Profil_1 . . . . .	24
	(b) Drag coefficient curve of Profil_1 . . . . .	24
	(c) Moment coefficient curve of Profil_1 . . . . .	24
3.5	Instances of grids used for the Grid Convergence exercise . . . . .	28
	(a) Grid 1 . . . . .	28
	(b) Grid 4 . . . . .	28
	(c) Grid 7 . . . . .	28
	(d) Grid 12 . . . . .	28
3.6	Example of $C_p$ treatment for BIRDIE optimisation . . . . .	33
3.7	Example of $C_f$ treatment for BIRDIE optimisation . . . . .	34
3.8	$C_p$ distributions related to different aerodynamic conditions and airfoils . . . . .	36
	(a) Assimilation1 . . . . .	36
	(b) Assimilation2 . . . . .	36
	(c) Assimilation3 . . . . .	36
	(d) Assimilation5 . . . . .	36
	(e) Assimilation6 . . . . .	36
	(f) Assimilation7 . . . . .	36
3.9	Flat Plate main chacaracteristics (extracted from [4]) . . . . .	38
3.10	Example of $X_4$ and $\tilde{X}_4$ . . . . .	39
3.11	Flat Plate Grid . . . . .	40
4.1	Profil_1 Geometry . . . . .	41
4.2	Non-dimensional wall distance and equation residuals examples for Profil_1 simulations . . . . .	42
	(a) Non-dimensional wall distance . . . . .	42

(b)	Equation residuals . . . . .	42
4.3	Flow field and boundary layer characteristic of Profil_1 simulations for different grids . . . . .	43
(a)	"Mesh 2" pressure coefficient distribution . . . . .	43
(b)	"Mesh 3" pressure coefficient distribution . . . . .	43
(c)	"Mesh 2" skin friction coefficient distribution . . . . .	43
(d)	"Mesh 3" skin friction coefficient distribution . . . . .	43
(e)	"Mesh 2" kinematic shape factor distribution . . . . .	43
(f)	"Mesh 3" kinematic shape factor distribution . . . . .	43
4.4	$C_p$ distribution of Profil_1 at different aerodynamic states . . . . .	44
(a)	Pressure coefficient evolution at ( $M_a = 0.71, \alpha = -0.75^\circ$ ) . . . . .	44
(b)	Pressure coefficient evolution at ( $M_a = 0.71, \alpha = 0.75^\circ$ ) . . . . .	44
(c)	Pressure coefficient evolution at ( $M_a = 0.75, \alpha = 0.0^\circ$ ) . . . . .	44
(d)	Pressure coefficient evolution at ( $M_a = 0.75, \alpha = 2.5^\circ$ ) . . . . .	44
4.5	Intermediate and final airfoils . . . . .	45
4.6	$C_p$ distribution of intermediate and final airfoils . . . . .	46
(a)	Pressure coefficient evolution at ( $M_a = 0.75, \alpha = 0.0^\circ$ ) for Profil_4 . . . . .	46
(b)	Pressure coefficient evolution at ( $M_a = 0.75, \alpha = 0.0^\circ$ ) for Profil_6 . . . . .	46
(c)	Pressure coefficient evolution at ( $M_a = 0.75, \alpha = 0.0^\circ$ ) for Profil_9 . . . . .	46
(d)	Pressure coefficient evolution at ( $M_a = 0.75, \alpha = 0.0^\circ$ ) for Profil_12 . . . . .	46
4.7	Convergence criteria instances . . . . .	47
(a)	Equation residuals . . . . .	47
(b)	Non-dimensional wall distance . . . . .	47
(c)	Relative error of the aerodynamic coefficients . . . . .	47
4.8	Pressure coefficient and skin friction distribution along "Porfil_12" for various grids . . . . .	50
(a)	$C_p$ distribution . . . . .	50
(b)	$C_f$ distribution . . . . .	50
4.9	Illustration of extraction positions . . . . .	50
4.10	Non dimensional velocity $U^+(y^+)$ extracted from elsA simulations in various grids . . . . .	51
(a)	$x = 0.1$ on the SS . . . . .	51
(b)	$x = 0.4$ on the SS . . . . .	51
(c)	$x = 0.85$ on the SS . . . . .	51
(d)	$x = 0.4$ on the PS . . . . .	51
(e)	$x = 0.8$ on the PS . . . . .	51
(f)	$x = 0.9$ on the PS . . . . .	51
4.11	Normalised aerodynamic coefficients per each grid . . . . .	52
4.12	Pressure coefficient distribution for best and worst cases of RAE2822 and EFT airfoils . . . . .	62
(a)	smallest $\sigma$ for RAE2822 . . . . .	62
(b)	biggest $\sigma$ for RAE2822 . . . . .	62
(c)	smallest $\sigma$ for EFT . . . . .	62
(d)	biggest $\sigma$ for EFT . . . . .	62
4.13	Pressure coefficient distribution for best and worst cases of C2 and Profil_12 airfoils . . . . .	63
(a)	smallest $\sigma$ for "C2" . . . . .	63
(b)	biggest $\sigma$ for C2 . . . . .	63
(c)	smallest $\sigma$ for Profil_12 . . . . .	63
(d)	biggest $\sigma$ for Profil_12 . . . . .	63
4.14	Skin friction coefficient distribution for best and worst cases for RAE2822 and EFT airfoils . . . . .	64
(a)	smallest $\sigma$ for RAE2822 . . . . .	64
(b)	biggest $\sigma$ for RAE2822 . . . . .	64
(c)	smallest $\sigma$ for EFT . . . . .	64
(d)	biggest $\sigma$ for EFT . . . . .	64
4.15	Skin friction coefficient distribution for best and worst cases for C2 and Profil_12 airfoils . . . . .	65
(a)	smallest $\sigma$ for "C2" . . . . .	65
(b)	biggest $\sigma$ for C2 . . . . .	65
(c)	smallest $\sigma$ for Profil_12 . . . . .	65
(d)	biggest $\sigma$ for Profil_12 . . . . .	65
4.16	Kinematic shape factor distribution for best and worst cases for RAE2822 and EFT airfoils . . . . .	66
(a)	smallest $\sigma$ for RAE2822 . . . . .	66
(b)	biggest $\sigma$ for RAE2822 . . . . .	66
(c)	smallest $\sigma$ for EFT . . . . .	66
(d)	biggest $\sigma$ for EFT . . . . .	66
4.17	Kinematic shape factor distribution for best and worst cases for C2 and Profil_12 airfoils . . . . .	67

(a)	smallest $\sigma$ for "C2 . . . . .	67
(b)	biggest $\sigma$ for C2 . . . . .	67
(c)	smallest $\sigma$ for Profil_12 . . . . .	67
(d)	biggest $\sigma$ for Profil_12 . . . . .	67
4.18	Instances of good and bad convergence results . . . . .	68
(a)	Good convergence . . . . .	68
(b)	Bad convergence . . . . .	68
4.19	Comparison between $C_p$ and $C_f$ distributions obtained with SA standard coefficients and with assimilated ones in Set3 . . . . .	71
(a)	$C_p$ distribution for standard SA parameters . . . . .	71
(b)	$C_p$ distribution for Set3 SA parameters . . . . .	71
(c)	$C_f$ distribution for standard SA parameters . . . . .	71
(d)	$C_f$ distribution for Set3 SA parameters . . . . .	71
4.20	$C_p$ and $C_f$ distributions obtained with assimilated SA coefficients in Set5, Set6 and Set7 . . . . .	73
(a)	Set5 . . . . .	73
(b)	Set5 . . . . .	73
(c)	Set6 . . . . .	73
(d)	Set6 . . . . .	73
(e)	Set7 . . . . .	73
(f)	Set7 . . . . .	73
4.21	Comparison between $C_p$ and $C_f$ distributions obtained with SA standard coefficients and with assimilated ones in Assimilation4 . . . . .	75
(a)	$C_p$ distribution for standard SA parameters . . . . .	75
(b)	$C_p$ distribution for Assimilation4 SA parameters . . . . .	75
(c)	$C_f$ distribution for standard SA parameters . . . . .	75
(d)	$C_f$ distribution for Assimilation4 SA parameters . . . . .	75
4.22	Discrepancy between $C_f$ calculated with SA standard constants and with those assimilated in Set3 for RAE2822 airfoil . . . . .	76
4.23	Pressure coefficient and skin friction distribution relative to the optimised parameters . . . . .	78
(a)	$C_p$ of C2 airfoil . . . . .	78
(b)	$C_f$ of C2 airfoil . . . . .	78
(c)	$C_f$ of RAE2822 airfoil . . . . .	78
4.24	Simulations results obtained with SA standard parameters . . . . .	80
(a)	Momentum thickness . . . . .	80
(b)	Normalised velocity . . . . .	80
(c)	Non dimensional velocity . . . . .	80
(d)	Skin friction coefficient . . . . .	80
4.25	Simulations results obtained with SA standard parameters . . . . .	81
(a)	Momentum thickness . . . . .	81
(b)	Normalised velocity . . . . .	81
(c)	Non dimensional velocity . . . . .	81
(d)	Skin friction coefficient . . . . .	81
4.26	Simulations results obtained with SA standard parameters . . . . .	82
(a)	Momentum thickness . . . . .	82
(b)	Normalised velocity . . . . .	82
(c)	Non dimensional velocity . . . . .	82
(d)	Skin friction coefficient . . . . .	82

# List of Tables

2.1	Main characteristics of wind tunnel pETW (from [2]) . . . . .	13
3.1	Principal mesh characteristics for Profil_1 airfoil . . . . .	23
3.2	Aerodynamic conditions simulated for Profil_1 airfoil . . . . .	24
3.3	Principal mesh characteristics for the Grid Convergence exercise . . . . .	27
3.4	Aerodynamic conditions tested in pETW . . . . .	30
3.5	Spalart-Allmaras turbulence model constants . . . . .	32
3.6	Set of SA turbulence model constants chosen to perform the data assimilations . . . . .	32
3.7	Aerodynamic conditions of Optimisation Problem 2 . . . . .	35
4.1	$x$ coordinate of the velocity profile extraction . . . . .	48
4.2	Asymptotic value and order of convergence of each aerodynamic coefficient . . . . .	49
4.3	Aerodynamic coefficients per grid type . . . . .	52
4.4	Grid Convergence Index calculated per each aerodynamic coefficient . . . . .	53
4.5	Far-Field Drag analysis per each grid . . . . .	53
4.6	Aerodynamics conditions simulated per airfoil . . . . .	58
4.7	$\sigma$ values between numerical simulations and experimental data on PS and SS <i>separately</i> . . . . .	59
4.8	$\sigma$ values between numerical simulations and experimental data on PS and SS <i>jointly</i> . . . . .	60
4.9	$\sigma$ values between elsA and ISES numerical simulations on PS and SS <i>separately</i> and <i>jointly</i> . . . . .	61
4.10	Optimisation Problem 1 synthesis . . . . .	68
4.11	Convergence results of the SA coefficient combinations . . . . .	69
4.12	Destruction term for the assimilated set of SA model parameters . . . . .	69
4.13	Data assimilations results . . . . .	71
4.14	Convergence history of Set3 optimisation. . . . .	72
4.15	Destruction term for the different assimilations . . . . .	74
4.16	Data assimilation results of Optimisation Problem 2 . . . . .	75
4.17	Optimisation Problem 3 synthesis . . . . .	76
4.18	Convergence history of Optimisation Problem 3 . . . . .	77
4.19	Optimisation Problem 4 synthesis . . . . .	79
4.20	Convergence history of Optimisation Problem 4 . . . . .	82

# Nomenclature

## Abbreviations

<i>RMS</i>	Root Mean Square
APG	Adverse Pressure Gradient
BL	Boundary Layer
CFL	Courant-Friedrichs-Lewy
FFD	Far-Field Drag (analysis)
GCI	Grid Convergence Index
NFD	Near-Field Drag (analysis)
OP	Optimisation Problem
pETW	pilot European Transonic Wind (tunnel)
PS	(airfoil) Pressure Side
RANS	Reynolds-Averaged Navier-Stokes (equations)
RSM	Reynolds Stress (equation) Model
SA	Spalart-Allmaras (turbulence model)
SS	(airfoil) Suction Side
WT	Wind Tunnel
ZPG	Zero Pressure Gradient

## Greek Symbols

$\alpha$	angle of attack
$\delta^*$	displacement thickness
$\delta^{**}$	density thickness
$\eta$	transverse shear layer coordinate
$\rho$	density
$\sigma$	discrepancy metric
$\tau$	wall shear stress
$\theta$	momentum thickness
$\theta^*$	kinetic energy thickness
$\xi$	streamwise arc length coordinate

## Subscript

e	external
---	----------

w wall

### Other Symbols

C1 Challenge 1 airfoil (Airbus)

C2 Challenge 2 airfoil (Airbus)

m millions

### Aerodynamics

$AoA$  angle of attack

$C_D$  drag coefficient

$C_D^*$  dissipation coefficient

$C_f$  skin friction coefficient

$C_L$  lift coefficient

$C_M$  momentum coefficient

$C_p$  pressure coefficient

$H$  shape factor

$H^*$  kinematic energy shape parameter

$H^{**}$  density shape parameter

$H_k$  kinematic shape factor

$M_a$  Mach number

$Re$  Re number

$U$  absolute velocity



# Chapter 1

## Introduction

### 1.1 ONERA and Work Environment

The "**Office National d'Etudes et de Recherches Aérospatiales**" (ONERA) is the most important national aerospace research center in France.

ONERA's historic roots are in the Paris suburb of Meudon, south of Paris, where this internship has taken place. As early as 1877, this site hosted an aeronautical research center for military aerostats (balloons). Only in May 1946 ONERA was officially established, after the Second World War.

ONERA is under Minister of Defence jurisdiction and some of its key figures are:

- A budget of €228 million;
- 8 establishments in France;
- 1960 collaborators, including 1477 engineers and management staff;
- 1st European wind-tunnel collection;

In addition, ONERA has different partnerships with private and public entities. ONERA's customer and partners include Airbus (Aircraft and Helicopters), Safran, Dassault Aviation, Thales and other major industry players. Whilst main public partners are both CNES in France and the European Space Agency (ESA), as well as the French defense agency (DGA). In addition, ONERA also works with European and international research establishments (such as DLR in Germany, JAXA in Japan and NASA in the USA).

ONERA is organized into 7 different departments:

- DAAA: Aerodynamics, Aeroelasticity, Acoustics department;
- DEMR: Electromagnetism and radar department;
- DMAS: Materials and Structures Department;
- DMPE: Multi-physics Department for Energetics;
- DOTA: Optics and Associated Techniques Department;
- DPHY: Department of Physics, Instrumentation, Environment and Space;
- DTIS: Information Processing and Systems Department;

This internship has taken place in DAAA which is, in turn, subdivided in:

- Civil Aviation (ACI)
- Aerodynamics, experimental methods and wind tunnel (AMES)
- Aeroelasticity and dynamics of experimental structures (ADSE)
- Design and production of software for fluid flows (CLEF)
- Demonstrations, efficiency, reliability and interoperability of software (DEFI)
- Experimentation and flight limit (ELV)
- Lille - Kampé de Fériet fluids mechanics laboratory (LMFL)

- Helicopters, propellers, turbomachines (H2T)
- Metrology, assimilation, physics of flows (MAPE)
- Missiles, fighter aircraft, stability, hypersonic (MASH)
- Acoustic methods for experimentation and the environment (MAXE)
- Modeling and numerical simulation for aeroelasticity (MSAE)
- Advanced turbulence modeling and simulation (MSAT)
- Digital methods for fluid mechanics (NFLU)
- Aeroacoustic numerical simulation (SN2A)

This project has been held in ACI Unit, where about 20 researchers, engineers and PhD candidates are part of. ACI contributes to the development and validation of numerical tools dedicated to the assessment and analysis of phenomena specific to the external aerodynamics of aircraft configurations (commercial, business, light aviation aircraft, etc.). The unit implements these tools and exploit experimental databases to improve physical understanding of these phenomena across the entire flight domain (cruise, high-speed, low-speed, stall, manoeuvres, etc.). ACI helps improving the aerodynamic performance of aircraft through the design of optimal aerodynamic shapes and the introduction of specific technologies, such as flow control or laminarity. It also contributes with proposals and assessments regarding new concepts of future aircrafts.



Figure 1.1: View of the historic S1 wind tunnel

## 1.2 Internship Objectives

The importance of Computational Fluid Dynamics (CFD) in analysis and design of aircraft shape is well known. This now mature science has made it possible to remarkably improve project times and costs, to increase performance of vehicles, while decreasing their emissions. Nevertheless, in ACI unit an unexpected inconsistency has recently been experienced between wind tunnel tests and CFD simulations for simple profiles. In this context, the objectives of the internship are to investigate this discrepancy, analyse its reasons and propose a possible approach to improve CFD accuracy. To implement this, the main activities carried out are:

- Mapping CFD reliability: exploring its variation with aerodynamic conditions and airfoil geometrical characteristics.
- Data assimilation: turbulence model parameters will be assimilated through innovative techniques.

Furthermore, given the physics involved and strong adverse pressure gradients, the analysis of the boundary layer and its properties will be carried out during this stage.

## 1.3 Report Structure

In the second chapter of this report the issue and the mission of this internship will be presented. Afterwards, an introduction to the CFD codes used during this study will be given, as well as an introduction to the BIRDIE optimisation method. The manner of the experimental tests have been carried out will be described, as well as an introduction to the Spalart-Allmaras model. Finally, a summary of the previous investigations on the subject of the stage is given.

In the third and fourth chapters, the methodology pursued and the results obtained during this stage are described. The design of a profile challenging to predict for CFD codes, a grid convergence study, a reliability mapping of CFD codes and a data assimilation exercise will be presented.

The last chapter will draw conclusions about the work carried out and future prospects.

# Chapter 2

## Context

### 2.1 Issue

CFD is a mature tool used by aeronautical industries and research establishments. Reynolds-averaged Navier-Stokes (RANS) equations solvers are particularly effective in airfoil shape optimization and wing design in cruise conditions, providing quite accurate results in a fairly short time. However, it does have margins for improvement in off-design conditions airflow prediction, when the separation of the boundary layer puts a strain on the validity of turbulence models. In this case, large-eddy simulations (LES), direct numerical simulations (DNS) or wind tunnel (WT) tests are certainly more recommended, although at higher cost and time.

In addition, its usage is expected to grow even more in the following years. The National Aeronautics and Space Administration (NASA) in [5] recommends continued research on aerodynamics and aero-acoustics, and emphasizes the need for the use of more physics-based analysis tools, and less use of analysis or simulation approaches based on empirical methods.

The Advisory Council for Aviation Research and Innovation in Europe (ACARE) Flightpath 2050 report [6] and Clean Sky initiatives [7] also lay out a strategic vision of innovation in the aeronautical sciences to drive future civil air vehicle transportation. The Flightpath report specifically states that in 2050: "... multi-disciplinary design and development tools are used routinely and co-operatively to support a high level of integrated system design. Final product performance is achieved to within a very fine tolerance (0.5%) of design prediction based on balanced design techniques and simulations ensuring right-first-time manufacture". The Clean Sky initiative goes further and highlights the need to streamline regulatory certification by ensuring "... a fully-integrated multi-physics and multi-scale model of the complete airframe is coupled with aerodynamic and thermal models **eliminating** ground test rigs completely".

In 2017, a wind tunnel test campaign was conducted in the pETW (pilot European Transonic Wind tunnel) under Airbus direction. The performance of different airfoils were then obtained, through measurements of the pressure field around them, in different aerodynamic conditions, principally at high Reynolds and transonic Mach numbers. The main purpose of this campaign was to obtain a database that would hence be used to investigate the ability of 2D RANS codes to predict the performances of supercritical airfoils.

RANS calculations obtained via elsA [8], a CFD code of Airbus-ONERA-Safran property, were compared with WT tests and large discrepancies were detected. Those were mainly concentrated on aft-cambered airfoils at cruise aerodynamic conditions. The difference in pressure distribution was mainly expressed in the upper surface shock position, reaching in some cases a difference of about 40 % of the chord between the numerical and experimental shock positions, as well as pressure absolute value all along the lower surface. Interestingly, a Euler equations solver code coupled with a boundary layer model called ISES [9] showed better prediction capabilities than elsA.

It should be reminded that airfoils in transonic conditions are perfectly within RANS validity domain. In light of the initial CFD considerations and its relevance for aerodynamics, some preliminary investigations have already been conducted in ACI unit by Jean-Luc HANTRAIS-GERVOIS, Marco CARINI, Didier BAILLY and Philippe BARDOUX.

## 2.2 Mission

Starting from these preliminary investigations, the purpose of this internship is to consolidate the findings by extensively assimilating the available experimental measurements in order to "map" the RANS turbulence modelling capabilities against the boundary layer physics for transonic airfoil design. This will be accomplished with the following approaches:

- Database Mapping: a significant amount of numerical simulations will be launched and pressure fields calculated and then compared with the database. The difference between numerical simulations and WT tests will be measured through a scalar indicator that will be introduced in the following sections. This will allow us to easily analyze how the latter varies depending on the type of airfoil and aerodynamic conditions (i.e. Mach number, angle of attack and Reynolds number).
- Assimilation of turbulence model parameters: an optimization code, called BIRDIE [10] designed by Didier Bailly at ONERA, will be used to assimilate the coefficients of the Spalart-Allmaras turbulence model [11]. To do this, multiple optimization problems will be proposed featuring various combinations of assimilated coefficients .

Some additional activities have been carried out during the development of this project: the design of an airfoil capable of reproducing the same problems as those in the database, an exercise of mesh convergence, boundary layer physics analysis and a bibliographic study are the main ones. A detailed description of these will be provided in the course of this text.

## 2.3 State of the Art

### 2.3.1 Introduction

Since the problem introduced above has never been dealt in literature, to the author's knowledge, a panoramic view of the subject in particular was quite complicated. Therefore it was chosen to cover topics that are more relevant to the subject of the internship:

- The aerodynamic prediction tools used, i.e. the CFD codes ISES and elsA, with a description of the boundary layer modelling in ISES;
- A presentation of the optimisation method BIRDIE;
- The particularities of the experimental tests carried out by Airbus in pETW;
- An introduction of the adverse pressure gradient effects on the boundary layer properties;
- An introduction of the Spalart-Allmaras model, with a focus on the physical sense of its constants;
- A synthesis of the preliminary investigations carried out at ACI unit about the inconsistency between CFD and experimental results introduced above.

### 2.3.2 elsA

The elsA software [12],[8] (Airbus, Safran and ONERA property) for external and internal flow aerodynamics and multidisciplinary applications has been developing at Onera since 1997. The research, development and validation activities are carried out using a project approach in cooperation with the aircraft industry and external laboratories or universities, led by ONERA. elsA deals with a wide range of aerospace applications: aircraft, helicopters, turbomachinery, open rotors, missiles, launchers, and so forth. An example of aircraft analysis is shown in fig. 2.1.

Today, elsA is used as a reliable design and analysis tool in aeronautic industry and research establishments in Europe, particularly in France. For instance Safran uses elsA for turbomachinery design purposes whilst Airbus for performance prediction and for aircraft design.

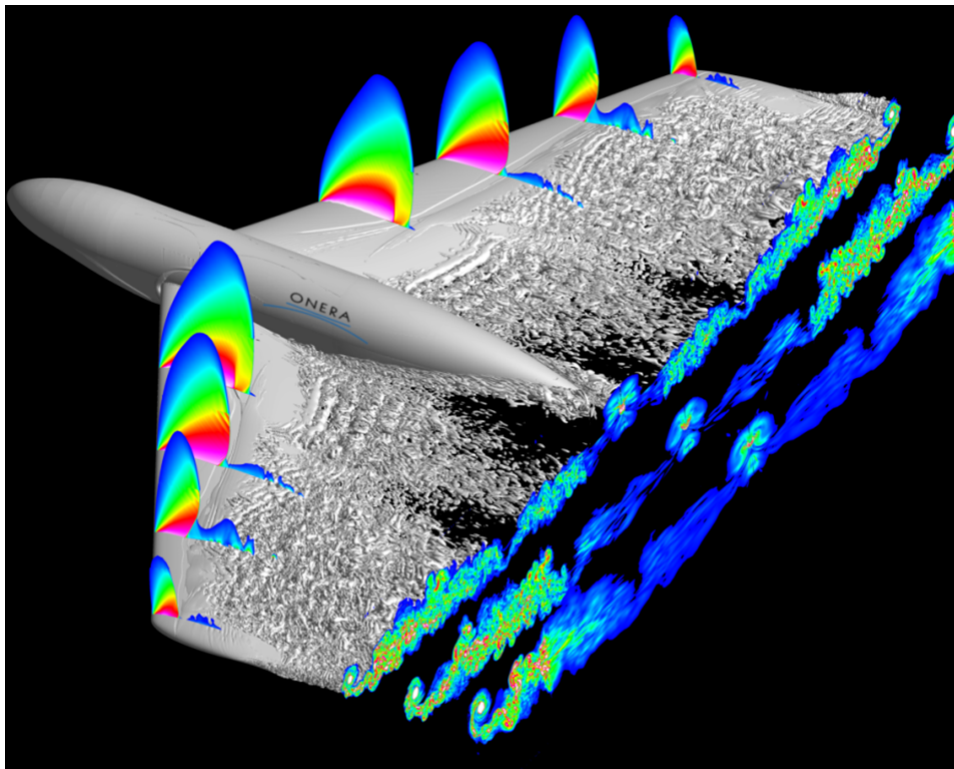


Figure 2.1: Transonic flow around a generic aircraft (Cat3D model) in cruise conditions. This image is taken from <http://elsa.onera.fr>

The elsA CFD software deals with internal and external aerodynamics from the low subsonic to the high supersonic flow regime and relies on the solving of the compressible 3-D Navier-Stokes equations. The thermodynamic properties of the fluid may correspond to the perfect gas or real gas assumption, the latter described by a Mollier diagram.

Large variety of turbulence models from eddy viscosity to full Differential Reynolds Stress models are implemented in elsA for the Reynolds averaged Navier-Stokes (RANS) equations. The range of turbulence models includes classical one-transport and two-transport equation models, more advanced two-equation models, one-layer or two-layer Algebraic Reynolds Stress models. Detached Eddy Simulations (DES) and Large Eddy Simulations (LES) are also available.

The flow equations are solved by a cell centered finite-volume method. Space discretization schemes include a range of second order centered or upwind schemes. The semi-discrete equations are integrated, either by multistage Runge-Kutta schemes with implicit residual smoothing, or by backward Euler integration with implicit schemes solved by robust LU relaxation methods.

A multigrid technique can be selected in order to accelerate convergence as well as a preconditioning technique can be used for low speed flow cases.

Complex geometrical configurations may be handled using high flexibility techniques involving multi-block structured body-fitted meshes. Chimera subprogram, for instance, enables the user to superimpose a thin grid on a coarser one, to improve accuracy locally.

The elsA software is based on an Object-Oriented (OO) design method. OO programming can be used to partition problems into well-separated parts, none of which needs to know more about the others than absolutely necessary. Hence, collaborations between several partners in code development are facilitated and new features are easily expandable.

Three languages have been using for implementing elsA: C++ as main language for implementing the OO design, Fortran for CPU efficiency of calculation loops, Python for the user interface and its user-friendliness. A good CPU and parallel efficiency is reached on a large panel of computer platforms.

### 2.3.3 ISES

ISES is a method of accurately calculating airfoil airflows, including in transonic conditions and at low Reynolds. It solves Euler equation coupled with a boundary layer model. It has been implemented in a code that can be used for analysis or design. It has been formulated and implemented by M. Drela and M. Giles. Its description is in [9].

In view of the extensive use of ISES during this stage, a general presentation must be made. Particular attention will be paid to the boundary conditions formulation and the boundary layer calculation model.

In fact, farfield boundary conditions makes ISES quite insensitive to the size of the computational domain and thus confinement effects are not reproduced. This will be relevant in *Section 2.3.8*, where confinement effects have been investigated.

As will be fully described later in this text, the boundary layer model produces better results than RANS for profiles with higher rear-loading. For this reason, this model will also be introduced here with particular attention on terms where involving adverse pressure gradient.

#### 2.3.3.1 Description

The Euler equations are solved and strongly coupled to a two-equation integral boundary-layer formulation. Concerning Euler equations, they are discretized in conservation form on an intrinsic grid, automatically generated by ISES, in which one family of grid lines corresponds to streamlines. An exemple of ISES computational domain is represented in fig. 2.2 and 2.3

A transition prediction formulation is derived and incorporated into the viscous formulation. The entire discrete equation set, including the viscous and transition formulations, is solved as a fully coupled non-linear system by a global Newton method. This is a rapid and reliable method for dealing with strong viscous-inviscid interactions, which inevitably occur in transonic and low Reynolds number airfoil flows.

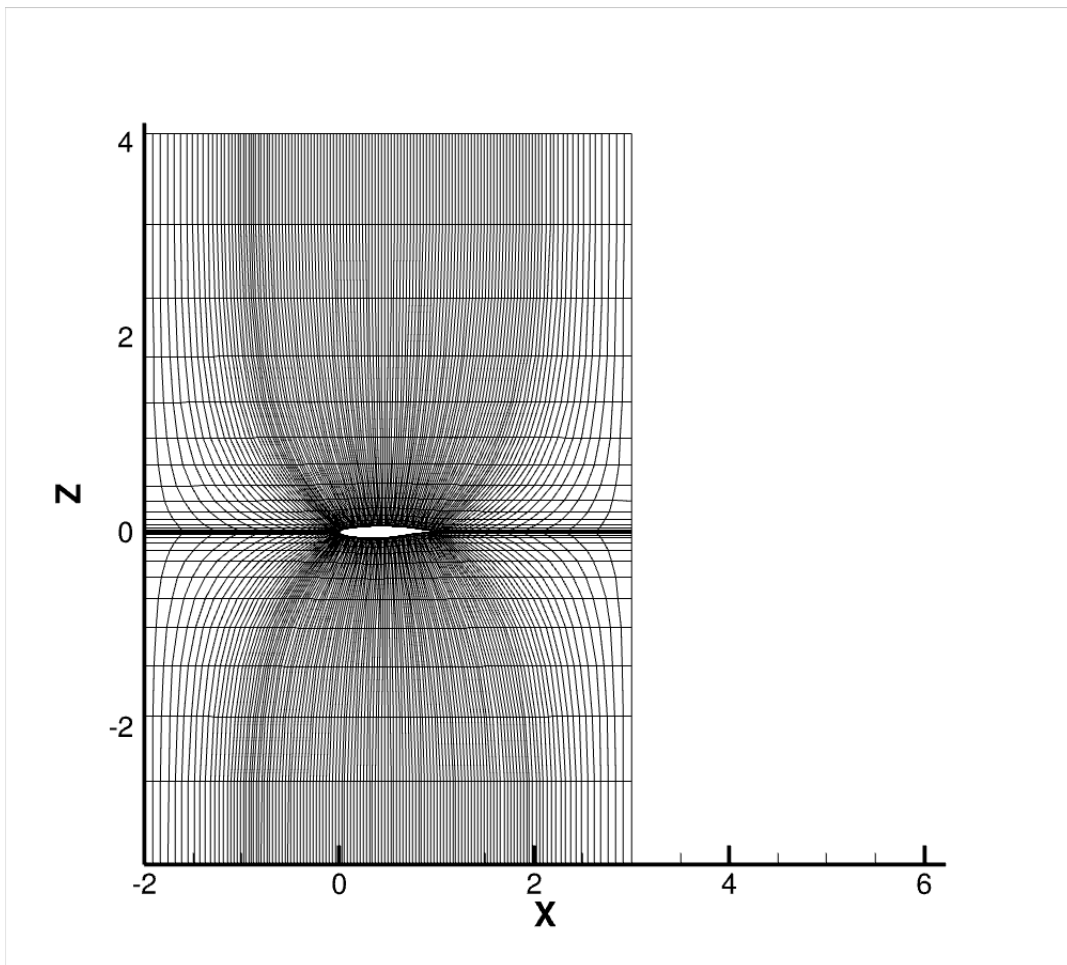


Figure 2.2: Exemple of ISES computational domain used for RAE2822 airfoil - overview

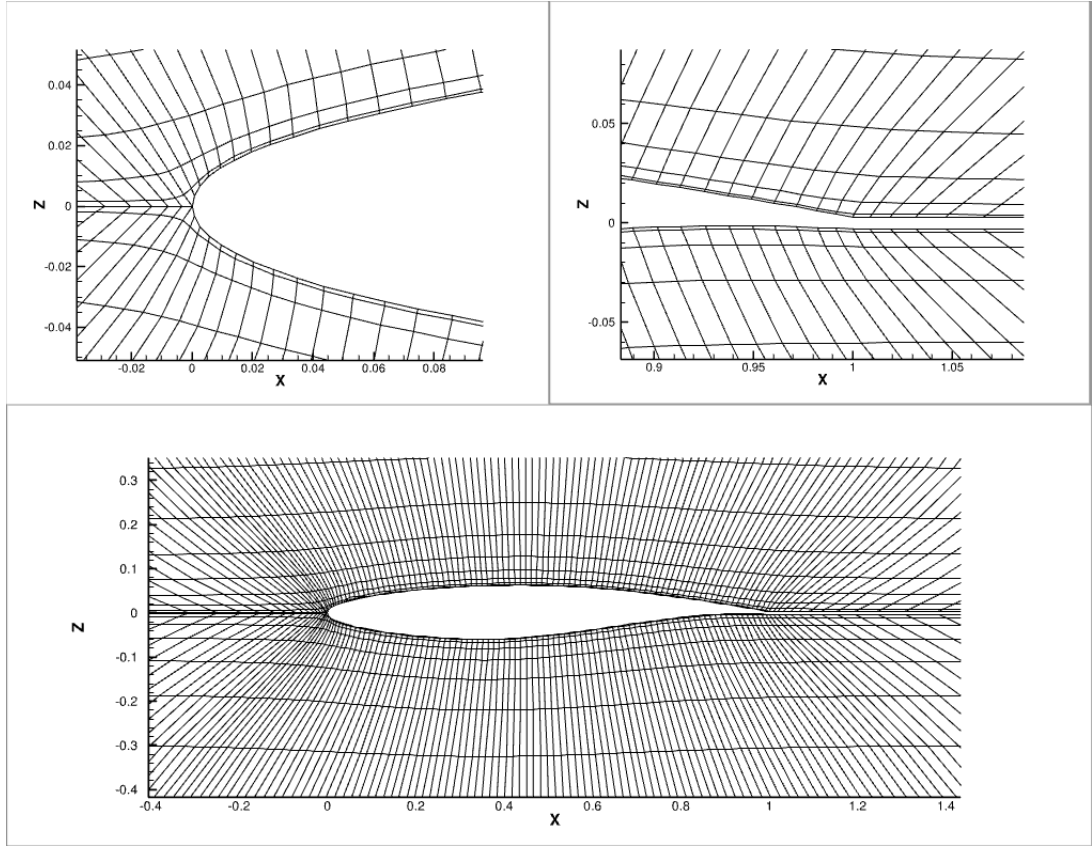


Figure 2.3: example of ISES computational domain used for RAE2822 airfoil. Mesh details at leading edge (top left) and trailing edge (top right) are shown as well as at the entire airfoil (bottom).

### 2.3.3.2 Boundary Condition Treatment

The boundary conditions are imposed on the airfoil solid surface as well as on the outer part of the computational domain.

For a non-viscous case, the slip condition is imposed on the airfoil wall which becomes effectively a streamline. For a viscous case, the same procedure is adopted, except that the streamline is displaced by the local displacement thickness  $\delta^*$ , defined as:

$$\delta^* = \int_0^\delta \left(1 - \frac{\rho U}{\rho_e U_e}\right) d\eta \quad (2.1)$$

where  $\eta$  is the transverse shear layer coordinate,  $\rho$  is the airflow density,  $\rho_e$  is the external airflow density,  $U$  its velocity and  $\delta$  the boundary layer thickness (i.e. the coordinate, normal to the airfoil wall, where the airflow velocity is equal to 99% of the external velocity  $U_e$ ).

For subsonic flow, the boundary condition at outermost domain streamline presents several contributions: the pressure derived from potential velocity of a uniform flow, a doublet, a source and a compressible vortex.

In the supersonic case, on the other hand, characteristic local and spatial relations are imposed to minimise spurious wave reflection within the domain.

### 2.3.3.3 Boundary Layer Formulation

The governing equations are integral boundary layer equations here reported:

$$\frac{d\theta}{d\xi} + (2 + H - M_{a_e}^2) \frac{\theta}{U_e} \frac{dU_e}{d\xi} = \frac{C_f}{2} \quad (2.2)$$

$$\theta \frac{dH^*}{d\xi} + [2H^{**} + H^*(1 - H)] \frac{\theta}{U_e} \frac{dU_e}{d\xi} = 2C_D^* - H^* \frac{C_f}{2} \quad (2.3)$$

where  $\theta$  is the momentum thickness,  $\xi$  the streamwise arc length coordinate,  $M_a$  the Mach number,  $H$  the shape factor,  $C_f$  the drag skin coefficient,  $H^*$  the kinematic energy shape parameter,  $H^{**}$  density shape factor and

$C_D^*$  the dissipation coefficient.

Some of the parameters above are defined as follow:

$$\theta = \int_0^\delta \frac{\rho U}{\rho_e U_e} \left(1 - \frac{U}{U_e}\right) d\eta \quad (2.4)$$

$$H = \frac{\delta^*}{\theta} \quad (2.5)$$

$$C_f = 2 \frac{\tau_{wall}}{\rho_e U_e^2} \quad (2.6)$$

where  $\tau_{wall}$  is the wall shear stress.

$$H^* = \frac{\theta^*}{\theta} \quad (2.7)$$

where  $\theta^*$  is the kinetic energy thickness.

$$\theta^* = \int_0^\delta \frac{\rho U}{\rho_e U_e} \left(1 - \frac{U^2}{U_e^2}\right) d\eta \quad (2.8)$$

$$H^{**} = \frac{\delta^{**}}{\theta} \quad (2.9)$$

where  $\delta^{**}$  is the density thickness.

$$\delta^{**} = \int_0^\delta \frac{U}{U_e} \left(1 - \frac{\rho U}{\rho_e U_e}\right) d\eta \quad (2.10)$$

$$C_D^* = \frac{1}{\rho_e U_e^3} \int_0^\delta \tau \frac{\partial U}{\partial \eta} d\eta \quad (2.11)$$

where  $\tau$  is the shear stress.

To close the problem, the following correlations are presumed:

$$H^* = f_1(H_k, M_{a_e}, Re_\theta) \quad (2.12)$$

$$H^{**} = f_2(H_k, M_{a_e}) \quad (2.13)$$

$$C_f = f_3(H_k, M_{a_e}, Re_\theta) \quad (2.14)$$

$$C_D^* = f_4(H_k, M_{a_e}, Re_\theta) \quad (2.15)$$

where  $H_k$  is the kinematic shape parameter.

$$H_k = \left[ \int_0^\delta \left(1 - \frac{U}{U_e}\right) d\eta \right] / \left[ \int_0^\delta \frac{U}{U_e} \left(1 - \frac{U}{U_e}\right) d\eta \right] \quad (2.16)$$

Depending on whether the flow is laminar, transitional or turbulent, different correlations were defined by Drela and Giles. For purposes of brevity, these correlations will not be disclosed completely but some considerations on terms directly connected to adverse pressure gradient will be done. In fact, in the turbulent layer closure, the only parameter explicitly linked to the adverse pressure gradient is the dissipation coefficient  $C_D^*$ , presented in eq. 2.3.3.3. In its description of these correlations, Drela used  $G - \beta$  locus of equilibrium boundary layer postulated by Clauser in [13]. Hence, the empirical  $G - \beta$  locus used is:

$$G = 6.7 \sqrt{1 + 0.75\beta} \quad (2.17)$$

where

$$G \equiv \frac{H_k - 1}{H_k} \frac{1}{\sqrt{C_f/2}} \quad (2.18)$$

$$\beta \equiv -\frac{2}{C_f} \frac{\delta^*}{U_e} \frac{dU_e}{d\xi} \quad (2.19)$$

where  $\beta$  is the Clauser pressure-gradient parameter and  $G$  the family parameter of equilibrium profiles. Thus, it can be noticed that  $\beta$  is influenced by the adverse pressure gradient.

### 2.3.4 BIRDIE

BIRDIE, a reverse-engineering method, was conceived by Didier Bailly at ONERA with the aim of combining experimental and CFD data in data fusion or data assimilation applications. Its description and validation is available in [1] and [10].

In a general optimisation approach, a functional quantifies the distance between the target field and the field corresponding to the parameters to be optimised.

A more modern approach, on the other hand, considers the points between the two fields as belonging to an affine space. The aim is to create a pseudo parameter space in which a projection of the target field can be defined. For instance, if the target is an experimental pressure distribution featuring 80 measurements, the affine space will be dimension-80 and the target can be located with its measurement coordinates.

Simplistically, to a vector of parameters  $\Theta$  corresponds a vector of vectors  $X$  in the affine space, the relation between them is defined by a  $\Phi$  process, such that  $X = \Phi(\Theta)$ .

From a linear combination of  $\Theta$  parameters,  $\tilde{\Theta}$ , a Euclidean subspace  $\tilde{X}$  can be parametrized, and vice-versa. A representation of these operations is presented in figures 2.4a and 2.4b, respectively.

By performing a projection of  $X$  into  $\tilde{X}$ , a link between  $\Theta$  and  $\tilde{\Theta}$  can be obtained, hence between the vector target  $X$  and the parameters to be optimised  $\tilde{\Theta}$ .

In addition, a loop process corresponding to a linear application between the parameter space  $\tilde{\Theta}$  and itself can be determined. This last step, as the name suggests, enables iterations.

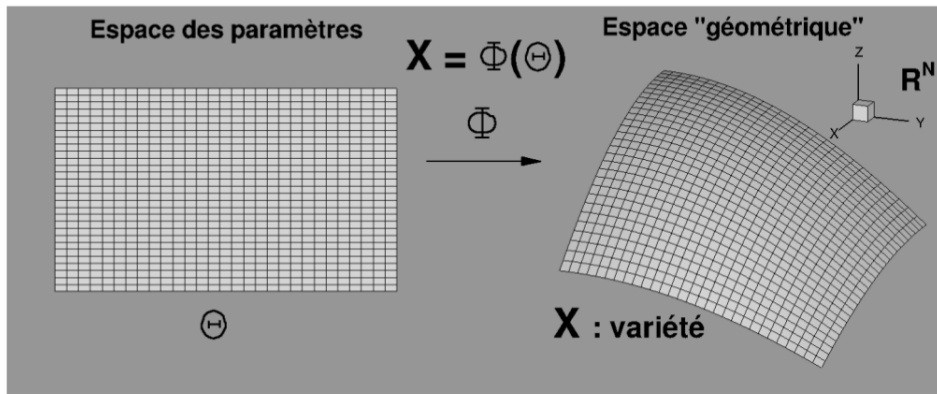
The iteration process is divided into two steps:

- *Predictor* step: a  $\tilde{\Theta}_n$  parameter is predicted by the algorithm on the basis of previous iterations, with  $n = 1, 2, \dots, N$ , where  $N$  is the total number of iterations.
- *Corrector* step: taking into account the distance between the target and the parameters to be optimised, a correction reducing this distance is implemented.

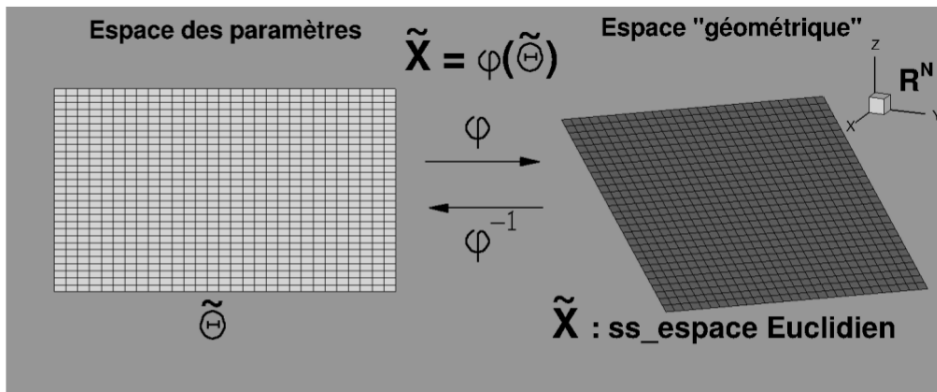
Before starting the iteration process, an initial parameter vector  $\tilde{\Theta}$ , and consequently also  $\tilde{X}$ , need to be initialised. For instance, by incrementing of 25 % each parameter in  $\tilde{\Theta}$ .

This approach has been used in many contexts. Its implementation is light because it requires no code modification nor gradients. The disciplinary code providing the output in the affine space given a set of parameters is embedded as a black box.

If this method is not physics-informed, a certain coherence of results is achieved (the resulting parameters usually make sense).



(a) Geometric space definition from a parameter vector



(b)  $\tilde{\Theta}$  space definition from a geometric subspace

Figure 2.4: Representation of BIRDIE mathematical operations (extracted from [1])

### 2.3.5 Wind Tunnel Tests

The pETW (pilot European Transonic Wind Tunnel) was built during the main wind tunnel facility development at a scale of approximately 1/9 and it is capable of achieving similar test and operation conditions as the main ETW cryogenic facility.

The main characteristics of the pETW facility are reported in Table 2.1. Airbus performed a test campaign in pETW on different profiles. Six different airfoil geometries have been tested during the campaign but only four of them have been studied during this internship and the preliminary investigations in section 2.3.8. These four airfoils are "RAE2822", "EFT", "C1" (Challenge 1) and "C2" (Challenge 2), from the least aft-cambered to the most one.

For confidentiality reasons, geometries of EFT, C1 and C2 will not be shown (Airbus design).

The most part of the tests has been conducted with slotted bottom and top wind tunnel walls: only for the RAE2822 airfoil measurements with solid walls have also been performed. In the adopted wind tunnel setup, the airfoil model is fixed to the side walls as shown in the pictures of figure 2.5. Its aspect ratio is 3, which is assumed to produce limited 3D effects. The maximum model thickness is of the order of  $\approx 10$  [mm], resulting in a blockage of 4.37%, under the conventional limit of 5%. Each model is equipped with a total of 100 pressure taps distributed in 3 sections: at 50% of the span and at 17% and 30% from the two side walls, respectively. Additional pressure measurements are also available on the top and bottom wind tunnel walls. In the present report, only measurements collected at the model centerline will be considered for comparison with CFD results. Hence, 74 pressure taps are available, 46 of which being located on the upper side and the remaining 28 on the lower side of the airfoil model. It is worthwhile to note that in this campaign, the airfoil models have not been equipped with a balance and direct global force measurements are not available.

Tests have been performed for several Reynolds numbers  $Re$ , varying from  $Re \approx 6.5 \cdot 10^6$  to  $Re \approx 15.7 \cdot 10^6$  and in a wide range of Mach numbers,  $M_a \in [0.2, 0.78]$ , but with most of the data being collected in the transonic regime. The tests conditions have been collected in table 3.4. For all the airfoils, wind tunnel tests have been conducted without fixing the laminar-to-turbulent transition, except for the RAE2822 airfoil, for which, for some tests, the transition was fixed at  $x/c = 0.03$  on the upper surface and at  $x/c = 0.05$  on the lower surface.

Test section size	0.229 [m] $\times$ 0.271 [m]
Mach number range	0.15 – 1.3
Pressure range	1.25 – 4.5 [bar]
Temperature	313 [K] (Condensation onset)
Reynolds number	up to $230 \cdot 10^6$ per meter

Table 2.1: Main characteristics of wind tunnel pETW (from [2])

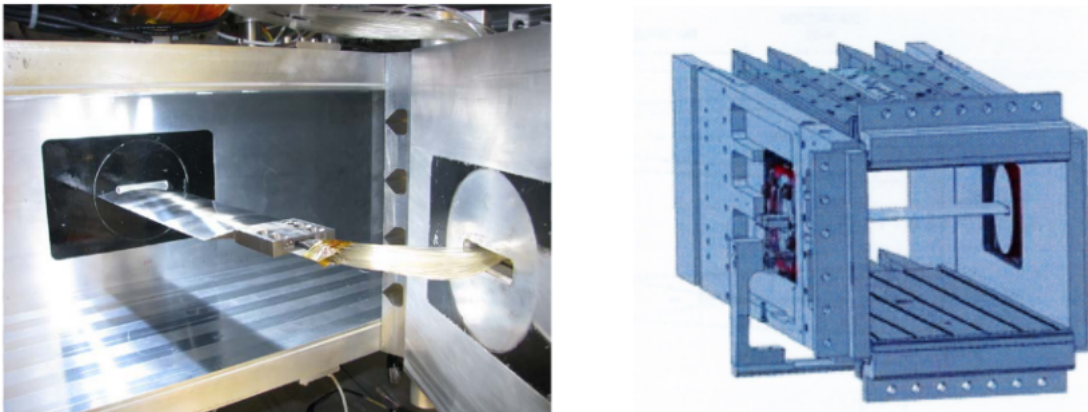


Figure 2.5: Pictures of wind tunnel pETW (from [2])

### 2.3.6 Adverse Pressure Gradient Effects

The fact that the adverse pressure gradient (APG) has a strong influence on the boundary layer is well known in aerodynamics, but how this is expressed is not completely well comprehended yet. Certainly the most known effect is that it causes boundary layer separation. Some other effects will be introduced below.

Before going further, we recall that, according to Richardson's energy cascade theory, the largest eddies of turbulence contain most of the kinetic energy, whereas the smallest eddies are responsible for the viscous dissipation of turbulence kinetic energy. Between these two, an intermediate range of scales is present, called inertial subrange, in which the energy is diffused from the large scales to the smaller ones.

However, in [14], a comparison between the turbulent structures in a zero pressure gradient (ZPG) boundary layer and a boundary layer subjected to a strong APG has been carried out. Surprisingly, an important reflection of the turbulent motion from the wall (where the smallest eddies are gathered), back into the outer layer (where the smallest eddies are accumulated) has been detected. Hence, a behaviour against the energy cascade theory.

In addition, APG effects on the outer layer of the boundary layer have been encountered in a variety of cases. For instance, in [15], direct numerical simulations were performed to investigate the effects of an adverse pressure gradient on a turbulent boundary layer over a flat plate.

Numerical results showed that the mean flows are greatly affected by an adverse pressure gradient, and the coherent structures in the outer layer, under strong APG, were more activated than those in the ZPG flows.

Similar results have been found in [16], where turbulent boundary layer properties have been analysed over a NACA0012 and NACA4412 wing sections. In this investigation, it has been found that a strong APG causes a reduction of the skin friction coefficient and a rise of the shape factor compared to ZPG cases. In addition, a large discrepancy between velocity profiles within the boundary layer was observed. In the case of a strong APG, a significant shift downward of the inner-scaled mean velocity within the buffer layer, compared to ZPG velocity profile, was detected as well a larger slope in the outer layer.

### 2.3.7 Spalart-Allmaras turbulence model

In this section a brief introduction to the turbulence model presented by P. Spalart and S. Allmaras in [11] will be made. Particular attention will be paid to the contributions of each term, as they will be protagonists of the data assimilation presented below.

This is a one-equation model, where the main variable is eddy viscosity  $\nu_t$ . Hence, it is based on Bussinesq hypothesis. It was designed with an empirical approach and was inspired from more classical turbulence models, such as  $k - \epsilon$  model in [17], and of course using variables with Galilean invariance.

The left-hand side of the equation is the material derivative of  $\nu_t$ ,  $D\nu_t/Dt$ , whilst on its right-hand side terms corresponding to the production, diffusion and destruction of the turbulence can be found. The construction of the equation was done by adding each contribution one at a time, and then appropriately calibrated. Each coefficient will be presented in its physical sense and/or its scope, its value in the standard equation and, if mentioned in the article, its physical range of validity.

- $c_{b1}$  represents the *production* term. Author's proposed value is 0.135 while his plausible range is between 0.128 and 0.138.
- $c_{b2}$  corresponds to the *diffusion* term. Its standard value is 0.622 and should be  $|c_{b2}| \leq 1$ . We must notice that if  $c_{b2}$  were lower than -1, turbulence behaviour would result physically incorrect on account of the fact that the turbulent front would propagate towards the turbulent region.
- $\sigma_P$ : Prandtl's number equivalent. The authors suggest a span of (0.6,1.0) and a standard value of 2/3.
- $\kappa$ : Von Karman constant, 0.41.
- $c_{w1}$ : the *destruction* term. Its definition is based on equilibrium among production, diffusion and destruction itself, hence:

$$c_{w1} = \frac{c_{b1}}{\kappa^2} + \frac{1 + c_{b2}}{\sigma_P} \quad (2.20)$$

- $c_{w2}$  and  $c_{w3}$ : without any modifications,  $c_{w1}$  produces a too little skin friction coefficient  $C_f$  in a flat plate boundary layer. Therefore, a non-dimensional function  $f(c_{w2}, c_{w3}, r)$  has been multiplied to  $c_{w1}$ , in order to artificially increase the rapidity of the destruction term to decay in boundary layer outer region.

The function  $f(c_{w2}, c_{w3}, r)$  is dependent to the coefficients  $c_{w2}$  and  $c_{w3}$  and an additional variable  $r$ . The latter is defines as follow:

$$r \equiv \frac{\nu_t}{S\kappa^2 d^2} \quad (2.21)$$

Where  $S$  is a measure of the deformation tensor,  $d$  is the distance to the wall and the other variables have already been declared. Standard values constants are respectively 0.3 and 2.0.

- $c_{v1}$ : this term affects the buffer layer and viscous sublayer. In addition, this term is in  $\tilde{\nu}$  definition, the final actual variable in the turbulence model equation, so that  $c_{v1}$  would to some extent influence all the other terms. Its recommended value is 7.1.
- $c_{t_i}$  for  $i = 1, \dots, 4$ : they concerns laminar boundary layer model response. Since we handle high Reynolds flows and it has been proven in [2] and [18] that laminar transition has very little effect on the airfoil pressure coefficient distribution, they have not been considered relevant to assimilate in this study.

## 2.3.8 Previous Investigations

### 2.3.8.1 Introduction

The main purposes of this section are to introduce the main work already done on this subject and to justify the various reasons that led this internship to focus on turbulence models to perform the data assimilation. In particular, how the adverse pressure gradient is influenced by turbulent models for aft-cambered airfoils. The reason between WT tests and CFD predictions mismatch is claimed to be due to incapability of standard turbulence model to deal with strong rear-loading. Hence, it is necessary to sum up the most important findings in [2] and [18] in order to exclude, as much as possible, other plausible motives which may cause this mismatch. One should know that this summary is not intended to replace the full analysis made in the reports listed above, but simply to give an indication of the investigations made and the results obtained from them. Unfortunately, these reports are confidential, so one might not consult them, if interested in learning more, without authorization.

Before reading the following, one should read *Section 2.3.5* where they can find a pETW test campaign introduction.

### 2.3.8.2 Technical Report 1

The principal aim of the technical report in [2] was to validate elsA prediction capabilities of 2D airfoils at transonic conditions. To accomplish this, RANS simulations at plausible cruise conditions were compared with pETW pressure distributions. Since a vast discrepancy was found, different strategies to find the cause were taken into account.

A preliminary validation of the experimental data was done through:

- a pressure distribution comparison of RAE2822 between pETW tests and another experimental campaign. No mismatch was encountered;
- a pressure distribution comparison of pETW results for different spanwise locations (50%, 33% and 17%). No wall nor 3D flow effects were detected. In fact, pressure distributions at 50% and 33% were almost equal.

Moreover, a set of Mach number and angle of attack ( $M_a, \alpha$ ) was optimised in order to find a pressure coefficient distribution matching the experimental one. For instance, a  $\Delta M_a \approx 0.009$  and  $\Delta \alpha \approx 0.4^\circ$  from the original ones were found for "C2" airfoil. These variations may indicate blockage effects but they were considered too high to be plausible values.

Furthermore, it was proven that wake mesh orientation at the trailing edge, turbulence models and laminar-turbulent transition criteria had negligible effects on pressure distribution and hence on the discrepancy. Concerning turbulence models, " $k-\omega$ ", "Spalart-Allmaras" (SA) and Reynolds stress equation model (RSM) turbulence models were compared and the only difference encountered was on the convergence results. In fact, only SA turbulence model had converged.

Conclusively, viscous-inviscid coupling solver ISES was found to predict the flow better than elsA and a preliminary investigation on boundary layer characteristics was performed.

### 2.3.8.3 Technical Report 2

The main scope of the technical report in [18] was to thoroughly analyse the discrepancy presented above. Based on the above analysis, arguing that the difference between the pETW and RANS data is due to the low reliability of the experimental results seems quite questionable. Nevertheless, one should always keep in mind the intrinsic limitations of experimental results, in view of the high blocking factor of the wind tunnel (4.37%). Therefore, grid domain sensitivity was examined in order to highlight these confinement effects. Afterwards, an in-depth analysis on turbulence models and their effects on boundary layer was achieved.

The mesh domain sensitivity study was carried out in three phases:

- Grid sensitivity of ISES results. As introduced in 2.3.3, this software generates the computational domain automatically. Nonetheless, its grid size and his domain grid can be modified by the user. Hence, six different grids were tested, varying the outer box, and ISES proved insensitive to these variations, thus confirming the solidity of its boundary conditions.
- RANS Domain extension sensitivity analyses. The impact of confinement effects in RANS simulations was investigated within the framework of unbounded flow modelling by gradually reducing the domain size while keeping standard farfield conditions on the outer boundary. As expected for the boundary conditions imposed, pressure coefficient distribution on the suction side has been found to be quite sensitive to outer

box size. However, such modifications have shown to not satisfactorily capture experimental pressure distribution features.

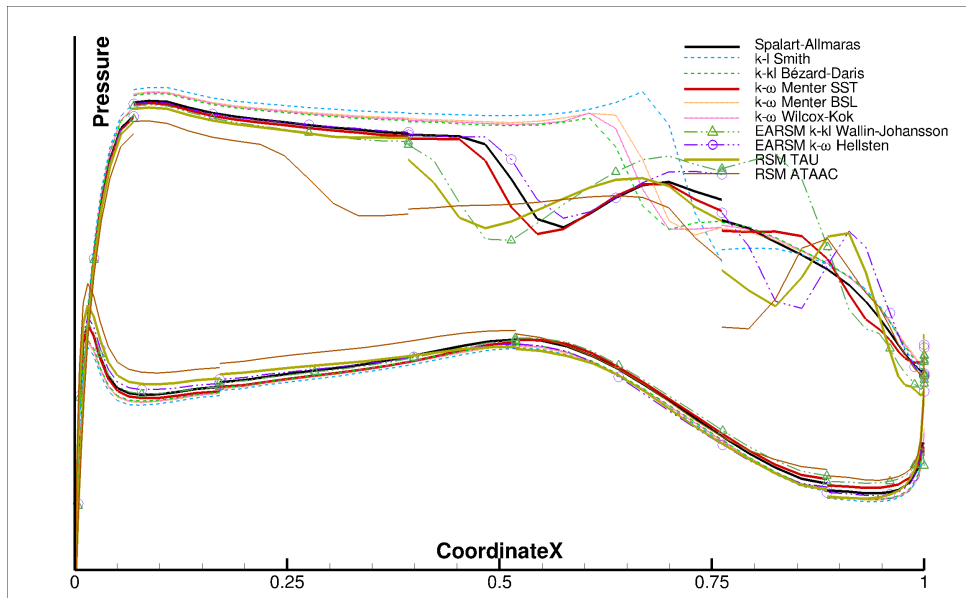
- 2D RANS modelling of wind tunnel confinements effects. RANS simulations were performed in a channel having the same features of pETW. For instance, blockage factor and slotted walls were respected from the original wind tunnel. Three types of boundary conditions were applied at the top and bottom walls: slip, no-slip and porous wall conditions. The pressure fields obtained from this computational wind tunnel model were found to be not in accordance with the experimental ones.

As a result of this study and the adequate accordance between not aft-cambered airfoils wind tunnel tests and numerical simulations, pETW database was considered reliable.

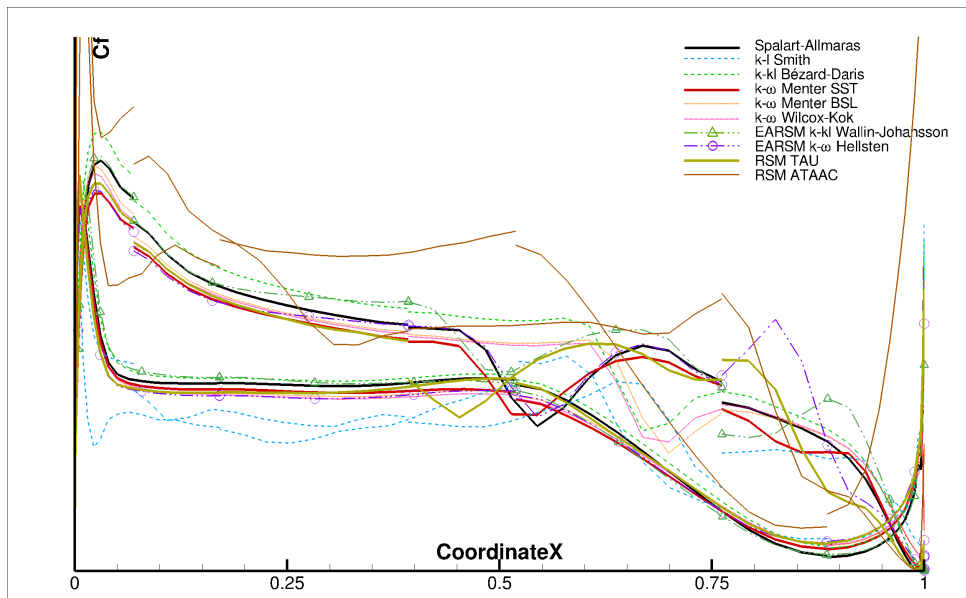
As in technical report 1, turbulence model influences on RANS prediction were investigated. However, a set of 10 different turbulence models available on elsA was chosen to perform this exercise and not only 3 models as previously. The results extracted from the technical report are shown in figure 2.6. Globally, the results of the 10 turbulence models span a shock excursion that widens with the profile curvature. The excursion is also large for the rear loading. Despite a lack of convergence, RSM SSG-LRR-omega model results were closest to pETW tests. Spalart-Allmaras model provided the best converged results.

Some of the turbulence equations constants described in 2.3.7 were assimilated, providing interesting results. In order to do this, BIRDIE [10] algorithm was used, and a set of constants chosen. In fact, BIRDIE compares the target (WT tests) with elsA output and furnishes new constants. Having used the new constants to launch a new simulation, elsA output will be compared with the target by BIRDIE, a new set of constants will be proposed and iterating until a potential convergence.

Matching pressure distribution between pETW and elsA results was obtained with excellent results. Nevertheless, the skin friction coefficient distribution over the airflow was found to be too high and further analysis about boundary layer properties were conducted. As a result of these preliminary analysis, the adverse pressure gradient has been considered as the cause of the discrepancy between experimental and CFD results.



(a) Pressure coefficient distribution



(b) Skin friction coefficient distribution

Figure 2.6: Turbulence model effects on  $C_p$  and  $C_f$  distributions

# Chapter 3

## Methodology

### 3.1 Numerical Setup

All the basic numerical features chosen to perform numerical simulations are here exposed. While elsA features has here exposed, ISES ones have been sufficiently disclosed in 2.3.3

#### 3.1.1 elsA

The numerical configuration and mesh features adopted for all the simulations performed with elsA have been chosen following the "good advices" presented in the technical report [19] and are common for all the simulations performed during this internship. Only the grid size and, in the final part of the stage, the constants of the turbulence models were changed.

**Numerical Configuration** Only steady 2D RANS equations simulations have been performed. Implicit Euler backward scheme has been used as time discretization. The Jameson scheme is employed for the spatial flux discretisation. The Courant-Friedrichs-Lewy (CFL) number varies linearly from 1 to 100 up to the thousandth time step, after which it remains constant. Depending on the calculation grid, the multi-grid method was used at 1 or 2 sub-levels. The Spalart-Allmaras turbulence model has been adopted and fully turbulent computations are performed without modelling the natural transition. Far-field boundary conditions are applied at computational domain borders whilst no slip condition at airfoil solid wall. All the simulations have been performed with a Total Temperature  $T_t = 220K$ .

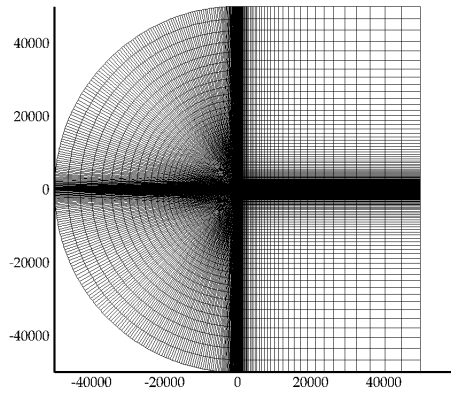
**Meshing Method** The computational domain is extended to 50000 chords lengths from the airfoil surface in order to have a negligible effect of the no-reflection far field boundary conditions on the pressure distribution and the aerodynamic forces, thus providing an accurate approximation of free-air conditions.

The computations have been performed on structured 2-block meshes featuring a C-H topology. The meshes have been created by using a modified version of the Rizzi's mesh method [3]: as an example, the grid used for RAE2822 airfoil computations is illustrated in fig. 3.5.

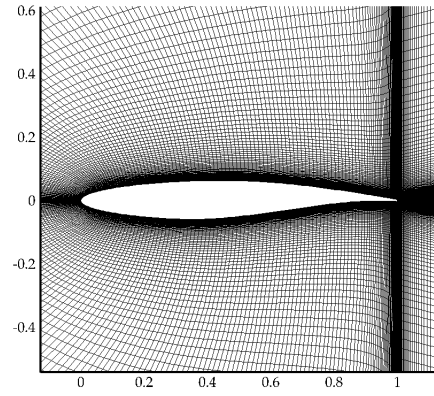
In particular, the grid in the near-wake region has a typical "fan-like" deformation due to the gradual relaxation of the near-wall refinement in the boundary layer region as moving downstream of the trailing- edge. As described in [19], this local modification greatly improves the residual convergence. Lastly for all grids generated, the following parameters are common:

- DSLE = 0.0006. The length of the first mesh cell on the airfoil surface at the leading edge;
- DSTE = 0.0005. The length of the first mesh cell on the airfoil surface at the trailing edge;
- DETLE =  $\sqrt{2/0.026} \cdot y^+ \cdot c \cdot Re_\infty^{(-13/14)}$ , where  $y^+$  is the non-dimensional wall distance,  $Re_\infty$  the upstream Reynolds number and  $c$  the chord length.
- DETTE =  $3 \times$  DETLE. The thickness of the mesh cell at the trailing edge.

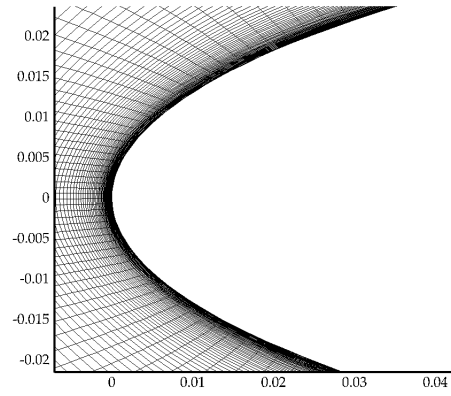
All this value are scaled by the chord length. This notation corresponds to the original one presented in [3].



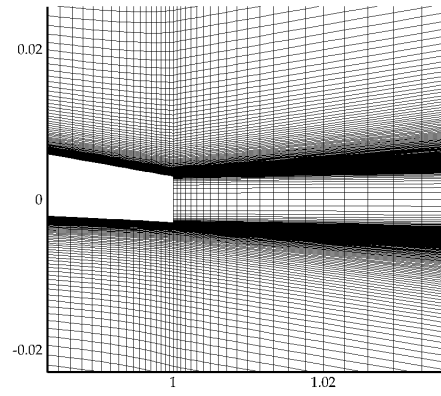
(a) Overview



(b) Grid around the airfoil



(c) Leading edge details



(d) Trailing edge details

Figure 3.1: Example of mesh generated by Rizzi method [3] for an elsA RAE2822 airfoil simulation

## 3.2 Profil\_12 Design

### 3.2.1 Introduction

The main purpose of this section is describing the procedure followed for designing Profil\_12 airfoil. The reasons for the design of an additional airfoil to those already in the pETW database, and which consequently has no experimental results, are multiples.

- **Acquiring elsA working flow procedures.** Thanks to this exercise, it was possible to familiarise with all the necessary and fundamental phases that are required to run a numerical simulation: pre-processing, post-processing and convergence check, for example. It is also worth remembering that elsA does not have a graphical user interface, but a textual one based on Python language. Hence, being comfortable with the various keys and very specific commands, as well as comprehending how to access to ONERA supercomputers, is a time-consuming process and an essential step.
- **Familiarising with BIRDIE.** This reverse engineering method has been used during the design of Profil\_12, as will be described later. In addition, it will be used to perform the data assimilation lately in the text.
- **Verifying a prior hypothesis.** From what has been analysed and expounded in technical reports [2] and [18], and presented in *Section 2.3.8*, the mismatch between ISES and elsA numerical results and WT tests is caused by the strong aft-camber of some airfoils. If a wing profile with this characteristic, i.e. a large rear loading, is designed, then one could expect a similar mismatching between ISES and elsA softwares.

By using BIRDIE method, an intermediate airfoil geometry was obtained from "RAE2822" airfoil. The intermediate airfoil has been called Profil\_1. Afterwards, geometric modification has been made to this airfoil and their effect on numerical simulations studied.

### 3.2.2 Procedure

#### 3.2.2.1 Intermediate Airfoil Profil\_1 Design

As already mentioned in the introduction, the aim of this exercise is to obtain a profile with inconsistent results between ISES and elsA, as it was for C2 profile. Therefore, it has been decided to utilise BIRDIE for solving a reverse-engineering problem. "RAE2822" profile has been selected as the starting point and C2 airfoil has been imposed as the target of the problem.

Thus, "RAE2822" profile has been associated to 8 parameters, contained in the parameter vector  $\tilde{\Theta} = \{\tilde{\theta}_1, \tilde{\theta}_2, \dots, \tilde{\theta}_8\}$ , in order to control its geometry. To do this, "RAE2822" profile coordinates have been associated to a "Bézier" curve, and then to Bernstein polynomials. Each "Bézier" curve is contained in the vector  $\tilde{X} = \{\tilde{X}_1\}$ , following the *Section 2.3.4* notation. The vector  $\tilde{X}$  is therefore a function of the parameters in  $\tilde{\Theta}$  and there is a unique correspondence between  $\tilde{\theta}_i$  and  $\tilde{X}$ , for  $i = 1, \dots, 8$ .

The first four parameters enables to control the airfoil thickness whilst the remaining its camber line, locally along the chord. In fact, the chord has been uniformly divided into 4 nodes including its extremities, thus obtaining a spacing between one node and another of  $\Delta x = 1/(4 - 1)$ , so that the generic parameter  $\tilde{\theta}_i$  and  $\tilde{\theta}_{i+4}$ , for  $i = 1, \dots, 4$ , can control the airfoil camber and thickness at the node  $x_i$ , respectively.

Naturally, any local change has repercussions around the profile. For instance, by increasing the value of  $\tilde{\theta}_1$  and  $\tilde{\theta}_5$ , a camber and thickness rise can be observed at  $x_1 = 0.0$ , as well as visible effects on the rest of the profile. Further informations about "Bézier" curves method are available in [20].

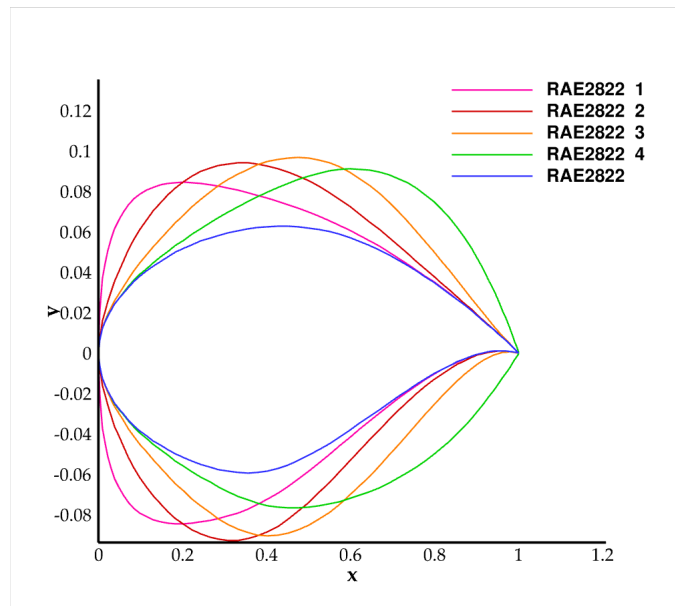
The scope of the problem is therefore to optimise the parameters contained in  $\tilde{\Theta}$  so as to obtain, after  $n$  iterations, a vector  $\tilde{X}_n$  as close as possible to a target. The selected target, named  $X$ , is C2 airfoil.

The reverse engineering process has been pursued in the following steps:

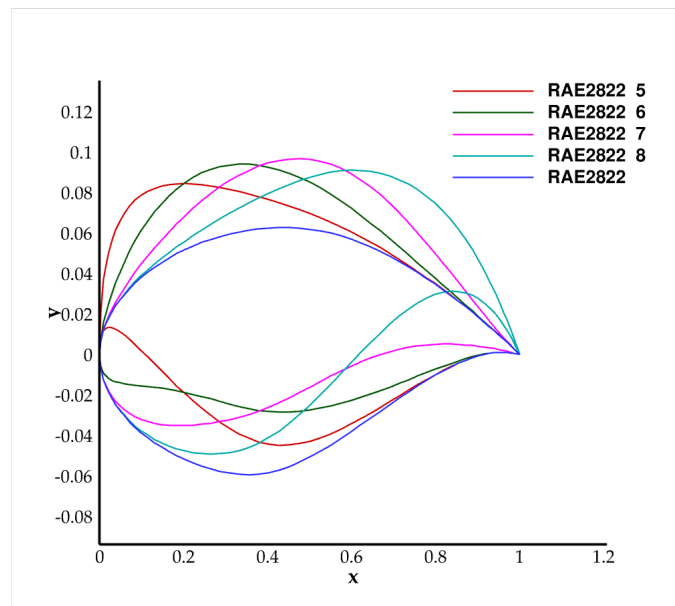
- **Initialisation.** Each "Bézier" parameter in  $\tilde{\Theta}$  has been incremented of 0.1 and the respective  $\tilde{X}$  vector calculated. Their grafical representation is presented in figure 3.2.
- **Iteration.** As a result of the previous step, BIRDIE proposed a new set of parameters, called  $\tilde{\Theta}_1$ . Using these parameters, a new airfoil shape has been calculated,  $\tilde{X}_1$ , and then given as an input to BIRDIE, which proposed  $\tilde{\Theta}_2$  and and so forth until convergence.

The reverse engineering process has been successful and the final profile shape,  $\tilde{X}_n$ , where n is the last iteration, was quite similar to the C2 profile. For this reason, the final result will not be shown. It must be noted, however,

that this has been only the starting point and ultimately Profil\_12 geometric characteristics are **different** from  $\tilde{X}_n$ .



(a) Variations on the airfoil thickness.



(b) Variations on the airfoil camber-line.

Figure 3.2: Initialization of BIRDIE parameters. The number next to airfoil name corresponds to subscripts of  $\tilde{\theta}_i$  parameter, which have been used to generate the airfoils.

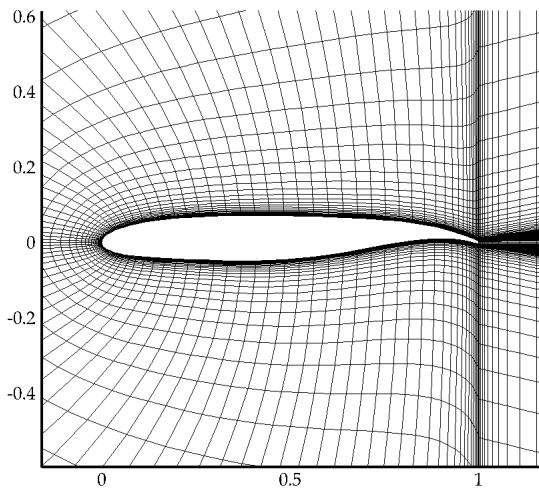
Successively, many geometrical adjustments, performed by manually modifying  $\tilde{\Theta}$  parameters, were applied to  $\tilde{X}_n$ . The main idea was to obtain an airfoil significantly different from C2 but also preserving an important rear-camber. After several iterations, the profile called Profil\_1 has been obtained.

Profil\_1 was tested with elsA and ISES software at various aerodynamic conditions, mainly transonic. In addition, results from 3 different grids, generated by the "RizziMesher" method, were compared for elsA numerical simulations.

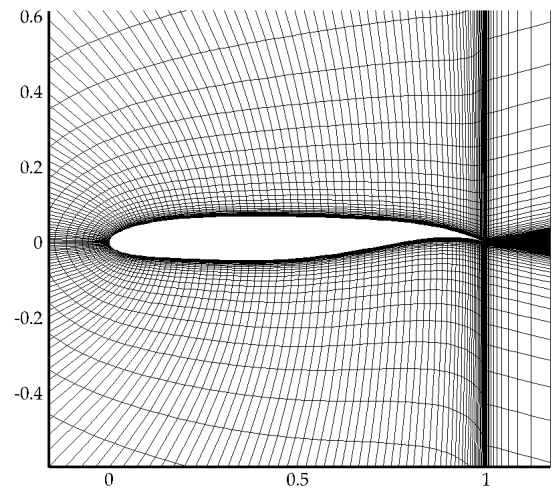
**Meshes** Tree meshes have been tested for the conditions presented in table 3.2. Their principal characteristics are displayed in table. 3.1 and their graphical representation is shown in figure 3.3.

<b>Name</b>	<b>C (I × J)</b>		<b>H (I × J)</b>		<b>Mesh points</b>
Mesh 1	96	96	48	202	19023
Mesh 2	193	96	48	202	28287
Mesh 3	385	385	193	809	304362

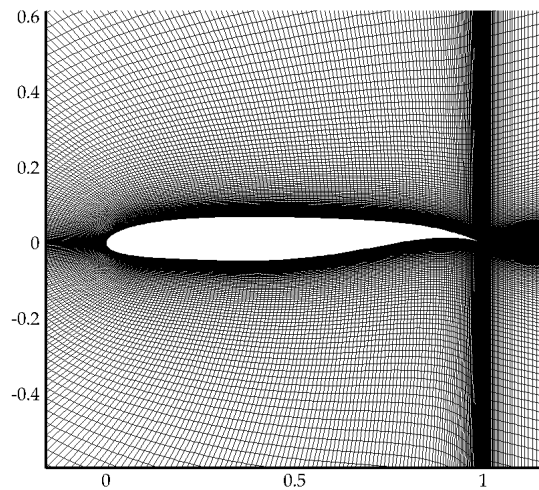
Table 3.1: Principal mesh characteristics for Profil\_1 airfoil. The leftmost column shows the mesh names, the middle ones the numbers of points in the streamwise (I) and radialwise (J) directions for C and H topologies and the last one the total number of mesh points.



(a) Mesh 1



(b) Mesh 2



(c) Mesh 3

Figure 3.3: Meshes used for Profil\_1 RANS calculations. Their main characteristics are provided in table 3.1

**Aerodynamic Conditions** The aerodynamics conditions simulated for Profil\_1 are summarized in table 3.2.

$Re$	$Ma$	$\alpha[^\circ]$				
		-1	-0.5	0	0.5	0.75
$15 \cdot 10^6$	0.71	-1	-0.5	0	0.5	0.75
$15 \cdot 10^6$	0.75	-1	0	1	2	2.5

Table 3.2: Aerodynamic conditions simulated for Profil\_1 airfoil.

The ISES software was used to select these sets of Mach and Reynolds number and angles of attack. This software is capable of calculating profile polars in a matter of seconds. Having fixed the Reynolds number to the most available in the pETW database,  $Re = 15 \cdot 10^6$ , the profile was then tested for various Mach numbers and angles of attack. By observing the trend of the main aerodynamic coefficients, the lift coefficient ( $C_L$ ), the drag coefficient ( $C_D$ ) and the momentum coefficient ( $C_M$ ), one can easily identify the most interesting incidences to be analysed. Particularly interesting has been the moment coefficient as a function of the angle of attack ( $AoA$ ) analysis. Indeed  $C_M$  derivative changes sign in presence of a shock. Therefore, angles of attack were chosen in the vicinity of the derivative sign change, after a graphical analysis. An example of a  $C_L$ ,  $C_D$ , and  $C_M$  curves is provided in fig. 3.4.

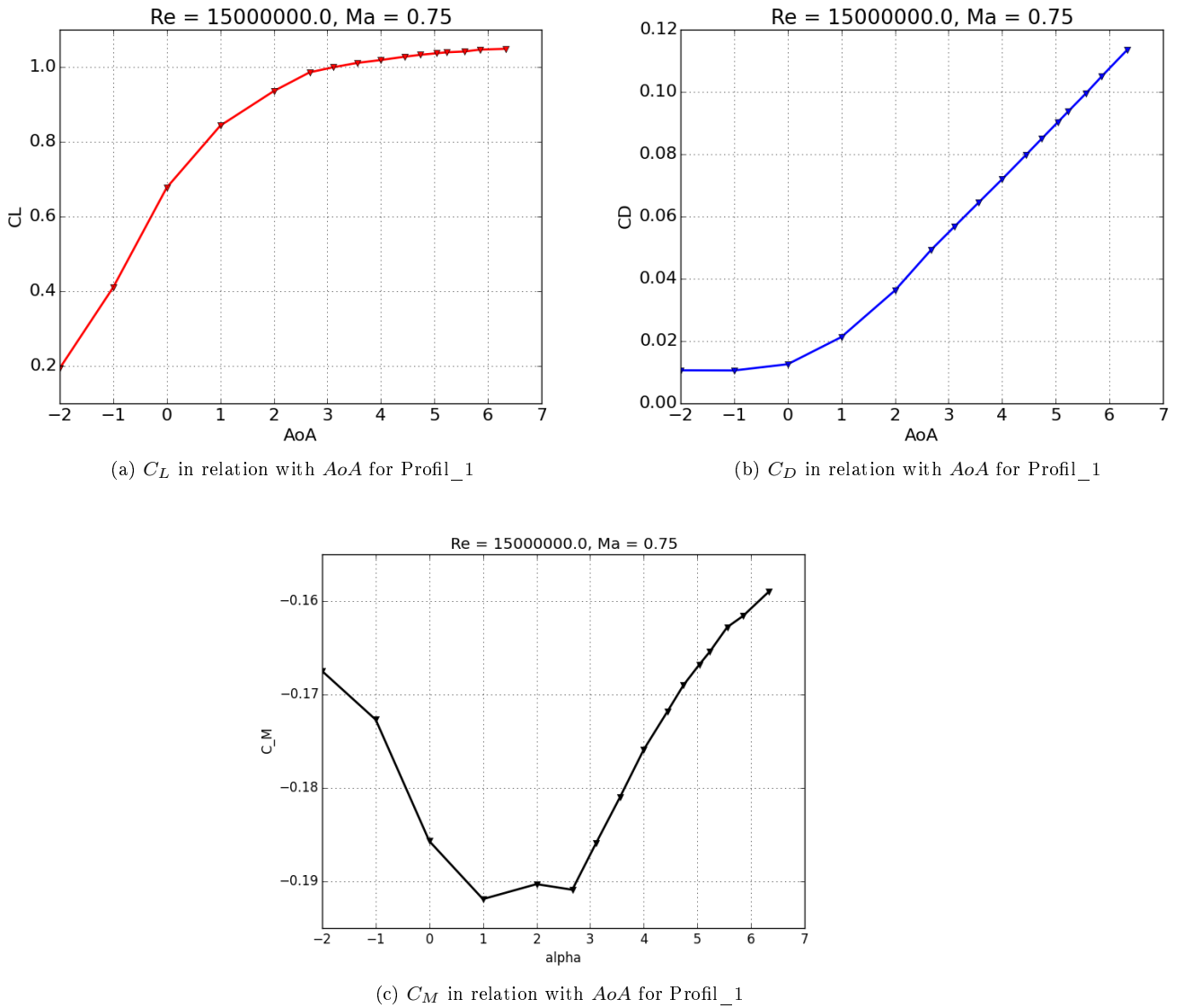


Figure 3.4: Example of polar curves of Profil\_1

**Numerical Configuration** The numerical configuration is described in Section 3.1.

### 3.2.2.2 Final Airfoil Profil\_12 Design

Many slight geometrical variations on the airfoil Profil\_1 were made to qualitatively evaluate the effects on the mismatch between the two pressure distributions and other boundary layer properties, from ISES and elsA softwares. All these simulations were performed with "Mesh 2" grid, referring to 3.1. In addition, constant Mach and Reynolds numbers have been chosen,  $M_a = 0.75$  and  $Re = 15 \cdot 10^6$ , whilst  $AoA$  could vary in a specific range,  $AoA \in (-3, 3)$ . After several iterations, a fairly satisfactory profile has been achieved.

## 3.3 Grid Convergence

### 3.3.1 Introduction

In this section, the Grid Convergence exercise will be presented. Before proceeding with the "database mapping" and data assimilations, it has been judged imperative to ensure the goodness of the results.

Indeed, as already envisaged from the previous section, the discrepancy between the two solvers can be quite significant and making sure that this is not due to the computational grid is a necessary step. The grid convergence exercise has been conducted on "Profil\_12" airfoil, as it has been reputed the less robust compared to the other airfoils. The aerodynamic state, chosen to fulfil this exercise, is determined by the the following parameters:  $Re = 15.6 \cdot 10^6$ ,  $M_a = 0.7338$  and  $\alpha = 0.0^\circ$ . Indeed they are representative values of standard cruise condition.

At first, the convergence criteria decided a priori and the main characteristics of the meshes will be presented. Hence, the global and specific characteristics of the flow field will be compared. In fact, the aerodynamic coefficients  $C_L$ ,  $C_D$  and  $C_M$ , as well as the pressure and wall friction coefficients ( $C_p$  and  $C_f$ ) and the velocity profile on different locations around the profile will be analysed. The Grid Convergence Index (GCI) will be calculated and a Far-Field Drag (FFD) analysis accomplished.

### 3.3.2 Procedure

#### 3.3.2.1 Numerical Convergence Criteria

Given the scope of this exercise, the convergence criteria chosen are quite strict.

Before presenting these criteria, it is useful to define the relative error  $\epsilon_x$  of a general quantity  $x$ .

$$\epsilon_x = \frac{x_{i+1} - x_i}{x_n} \quad \text{with} \quad i = 0, 1, \dots, n - 1, n \quad (3.1)$$

Hence, the chosen criteria are as follows:

- relative error of the aerodynamic coefficients  $C_L$ ,  $C_D$  and  $C_M$ ,  $\epsilon < 10^{-8}$ ;
- RANS equations residuals decay by at least 6 orders of magnitude;
- non-dimensional wall distance  $y^+ \leq 1$ . Through the formulation of the first cell size in *Section 3.1*, a value of  $y^+$  around 0.2 was obtained.

#### 3.3.2.2 Grids

All the grids have been generated through the modified Rizzi method introduced in *Section 3.1*. Table 3.3 shows the grid main characteristics. Some instances of these are presented in figure 3.5.

### 3.3.3 Grid Convergence Index

The Grid Convergence Index (GCI) [21] is a measure of grid quality. It is calculated with respect to the variation of a parameter while refining the grid. The parameter choice is completely free, but often aerodynamic coefficients are chosen. The smaller the value, expressed as a percentage, the closer the value of the chosen parameter to the asymptotic value.

In addition, the spatial convergence order  $p$  and the asymptotic value of the aerodynamic coefficients have been also calculated. The spatial order of convergence represents how quickly the numerical solution converges to the final and unique numerical solution as the grid is refined. With the numerical scheme used, this should equal 2. The asymptotic value of the coefficients, on the other hand, is an estimation of their hypothetical value if an infinitely fine mesh had been used. In other words, the actual solution without numerical errors.

A code written in FORTRAN and provided by NASA in [21] was used to compute these parameters.

### 3.3.4 Far-Field Drag Analysis

Using an innovative thermodynamic approach, a Far-Field Drag (FFD) analysis is capable of splitting the total drag into physical and numerical contributions. These are divided into:

- $C_{D_p} = C_{D_{vp}} + C_{D_w}$ ;
- $C_{D_{vp}}$ , viscous pressure drag;
- $C_{D_w}$ , (shock)-wave drag;

- $C_{D_i}$ , induced drag (since only 2D RANS have been performed, this term is not present);
- $C_{D_f}$ , skin friction drag;
- $C_{D_{sp}}$ , spurious drag.

The latter term  $C_{D_{sp}}$  is divided into reversible and non-reversible spurious drag. While the former can be recovered by changing the numerical methods and/or the computational domain, the latter is estimated as irrecoverable. For example, a good grid has few units of drag coefficient, while a bad one has about 10. Hence, this parameter will be convenient to evaluate the grid quality.

A theoretical introduction about FFD analysis is provided hereafter.

Traditionally, surface integrals (generally speaking of a 3D case) are used to evaluate wall stresses, and hence drag and lift computation. Doing so, part of the drag corresponds to some numerical errors and then is over-estimated. For instance, the wall stress integration nearby the leading edge, where gradients could reach quite high values. This approach is here called Near-Field Drag Analysis (NFD). By integrating the shear stress and the pressure on a wing (or on an airfoil in the 2D case), it is possible to calculate the drag (or equivalently the drag coefficient) and decompose it as follow:

$$C_{D_{nf}} = C_{D_p} + C_{D_f} + C_{D_{sp}} \quad (3.2)$$

where  $C_{D_p}$  is the drag coefficient due to the pressure distribution on the profile and  $C_{D_f}$  due to friction stresses. The contribution of  $C_{D_{sp}}$  is unknown.

However, in the FFD analysis, volume integrals rather than surface ones are used.

Starting from the RANS momentum integral-equation, its variables are manipulated in order to obtain thermodynamic ones, such as enthalpy and entropy. An equivalent equation is hence obtained but in thermodynamic terms. By transforming the equation domain from two-dimensional into three-dimensional, i. e. applying the Stokes theorem, an integral equation over the entire computational domain is defined. Considering the integral additivity property, the domain to be integrated can be divided into several parts: a part that corresponds to the boundary layer, a part surrounding a (possible) shock and and the remaining computational domain. In order to divide the domain, numerical sensors are used. By calculating the integral equation on each sub-domain, it is possible to estimate the various contributions to the aerodynamic drag as follow:

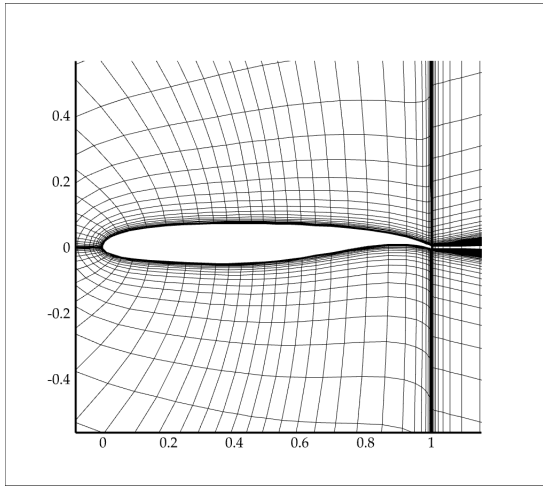
$$C_{D_{ff}} = C_{D_p} + C_{D_f} = C_{D_{vp}} + C_{D_w} + C_{D_f} \quad (3.3)$$

By subtracting the drag estimated by near-field the far-field approaches, the spurious drag is obtained.

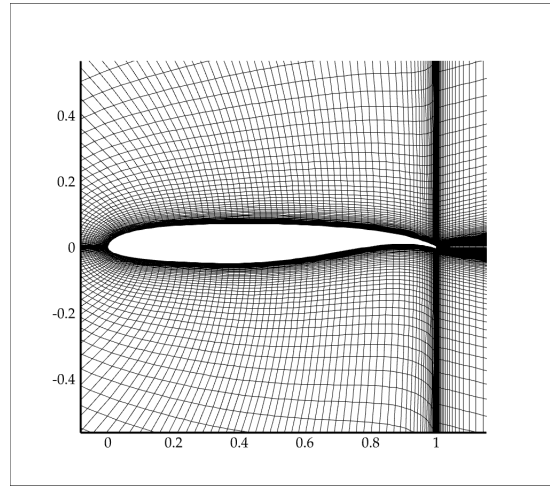
$$C_{D_{nf}} - C_{D_{ff}} = C_{D_{sp}} \quad (3.4)$$

<b>Name</b>	<b>C(I × J)</b>		<b>H(I × J)</b>		<b>Mesh points</b>
Grid1	77	77	39	160	12749
Grid2	115	115	57	240	28700
Grid3	155	155	77	324	51392
Grid4	193	193	97	405	82456
Grid5	231	231	115	509	118994
Grid6	269	269	135	593	160692
Grid7	309	309	155	681	210540
Grid8	347	347	173	765	263414
Grid9	385	385	193	849	323920
Grid10	423	423	213	933	390674
Grid11	463	463	231	1021	464442
Grid12	577	577	193	1233	587536

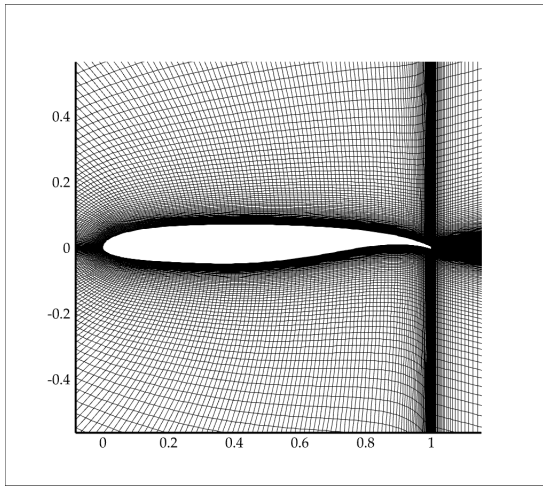
Table 3.3: Principal mesh characteristics for the Grid Convergence exercise. The leftmost column shows the mesh names, the middle ones the numbers of points in the streamwise (I) and radialwise (J) directions for C and H topologies and the last one the total number of mesh points.



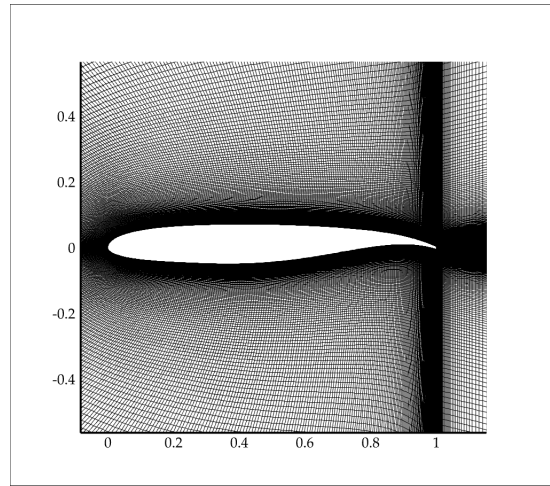
(a) Grid 1



(b) Grid 4



(c) Grid 7



(d) Grid 12

Figure 3.5: Instances of grids used for the Grid Convergence exercise

## 3.4 Reliability mapping of the "pETW" database

### 3.4.1 Introduction

In this section, the reliability of CFD simulations, calculated with elsA and ISES codes, for 2D airfoils has been investigated with respect to the database pETW. The selected airfoils are RAE2822, EFT and C2. The C1 airfoil has not been chosen in view of his geometric similarity to EFT.

In addition, the airfoil presented in *Section 3.2* and called Profil\_12 has been compared only between ISES and elsA data.

In order to achieve this, firstly some aerodynamic conditions provided in the database were suitably selected and then simulated on the CFD codes. Subsequently, pressure coefficients distributions deriving from numerical simulations and from the database have been compared for different aerodynamic conditions, through a scalar metric that will be introduced afterwards. Lastly, the results will be shown in the form of tables and plots and briefly disclosed.

The main objective of this exercise is to prove that, for airfoils with certain characteristics, numerical simulations are unsatisfactory over a wide range of  $Re$  and  $M_a$  numbers and  $AoAs$ , and therefore they are not suitable for predicting the airflow.

### 3.4.2 Procedure

The initial choices of the "mapping" procedure are:

1. **Choice of the aerodynamic conditions (Mach and Reynolds numbers);**
2. **Choice of  $AoA$ ;**
3. **Choice of the comparative scalar variable, called  $\sigma$ .**

The numerical setup is described in *Section 3.1*, the grid is "Grid7" defined in *Section 3.3* and the convergence criteria are those used to perform the Grid Convergence study.

#### 3.4.2.1 Aerodynamic conditions

All the tests within the database have been collected in a table having Mach number as rows and Reynolds number as columns. The table is shown in 3.4.

In this table, the aerodynamic conditions under which the WT tests were carried out have been provided, with distinction amongst the various profiles, the Mach and Reynolds. When all the airfoils have been tested with the same aerodynamic conditions, "ALL" is written in the cell.

For instance, one can notice that the "RAE" and EFT airfoils were also tested at low Mach and Reynolds, while the remaining C1 and C2 profiles were tested mainly for high Mach and Reynolds. In addition, we note that all the airfoils have been tested principally for high Reynolds and Mach numbers.

In order to be able to compare the results more easily and to limit numerical resources usage, only some points of this table have been selected. The selection criteria have been:

- A wide distribution of Mach and Reynolds number to test;
- A sufficient number of points in transonic conditions.

Those points are red coloured in the table.

The blue cells have been added with the aim of investigating Mach and Reynolds effects on CFD codes prevision capability. In fact, it can be noticed that blue cells are at the same line than red cells at lowest and highest Mach number. Evidently, no experimental data are accessible to compare with.

#### 3.4.2.2 Choice of $AoA$

For each airfoil, excepting Profil\_12, and for each pair of  $M_a$  and  $Re$ , a set of roughly five  $AoA$  has been picked from the database pETW. Concerning Profil\_12, it has been chosen either the same  $Re$ ,  $M_a$ , and  $AoA$  as C2, either a range of  $AoA$  judged appropriate for that  $Re$  and  $M_a$ . The procedure selection steps have been the following:

Ma/Re	2.87 m	3.57 m	4.25 m	5 m	6.2 m	6.4 m	7.5 m	8.9 m	9.7 m	11 m	13.5 m	15.7 m
0.2	RAE EFT			RAE EFT								
0.25		RAE EFT			RAE EFT							
0.3			RAE EFT				RAE EFT					
0.4									RAE EFT			
0.5										ALL		
0.6						RAE		RAE			ALL	
0.7												RAE EFT
0.705												ALL
0.71												RAE EFT
0.715												ALL
0.72												RAE EFT
0.725								RAE				ALL
0.73						RAE		RAE EFT				RAE EFT
0.735						RAE		RAE C1 C2		RAE EFT	RAE EFT	ALL
0.74								RAE EFT		RAE	RAE EFT	RAE EFT
0.745								ALL				ALL
0.75								ALL				ALL
0.755								ALL		C1 C2	C1 C2	ALL
0.76								RAE				ALL
0.765								C1 C2				ALL
0.77												RAE
0.775								RAE C1 C2				ALL
0.78												RAE
0.785								RAE				ALL
0.79												RAE
0.795												RAE
0.8												RAE

Table 3.4: Aerodynamic conditions tested in pETW. The red cells are the points chosen to simulate with experimental data availability. The blue ones are additional points where no experimental data are available.

1. graphical analysis of the drag and moment coefficients curves in pETW and choice of 5 different  $AoA$ . In fact, when the moment coefficient derivative changes sign at high Mach number, shocks usually are the reason.
2. calculation through CFD codes.
3. if the simulation is converged, the angle of attack is preserved; otherwise, reiteration until convergence.

Since this method has not been used for Profil\_12 points selection, some of its numerical simulations have diverged, particularly for transonic conditions.

### 3.4.2.3 Discrepancy metric $\sigma$

Considering the large amount of data, 4 airfoils  $\times$  9 couples of  $(Re, M_a) \times 5 AoA$ , a scalar variable capable of measuring the discrepancy between experimental and numerical data has been defined as follow:

$$\sigma = \sqrt{\frac{1}{N} \cdot \sum_i^N (y_{1_i} - y_{2_i})^2} \quad (3.5)$$

where  $y$  is the quantity to compare, in this case  $C_p(x_i)$ , picked at  $N$  places over the profiles. 1 and 2 indices represent the data to compare, they could be either experimental from the pETW database, either numerical calculated by elsA and by ISES.

To avoid interpolation issues, the chord distribution  $x_i$  corresponds to the experimental locations of pressure sensors, as reported in *Section 2.3.5*. Hence, the numerical pressure coefficient distribution have been interpolated on the same spatial discretization. One should know that numerical data have much finer discretization than experimental ones, therefore accuracy has been preserved during this operation.

## 3.5 Data Assimilation

### 3.5.1 Introduction

This final section will present the data assimilations carried out during this stage. As it can be noticed from the previous results, the discrepancy between experimental and numerical data can be quite important. In order to attempt to decrease this discrepancy, the constants of the Spalart-Allmaras turbulence model will be assimilated using the BIRDIE code. An introduction to the Spalart-Allmaras (SA) model is furnished in *Section 2.3.7*. Departing from the work accomplished previously and summarized in *Section 2.3.8*, which had brought highly promising results, 4 optimisation problems were formulated. These will be called "**Optimization Problem 1**", "**Optimization Problem 2**", "**Optimization Problem 3**" and "**Optimization Problem 4**". To achieve this, an automation code, written in Python by the author of this text, enabled to link multiple elsA simulations (i.e. its pre-processing, RANS calculation and post-processing phases) with the BIRDIE code and the pETW database.

The objective of these assimilations is finding a suitable combination of SA constants that models in a better manner the physics involved, i.e. large pressure gradient of aft-cambered profiles under transonic conditions. However, with the aim of preserving as much as possible the physics of the model with the assimilated constants, other flow properties will be analysed: an example are the wall friction coefficient and the velocity profile within the boundary layer. In case inconsistencies arise, subsequent data assimilation will take them into account, i.e. by imposing them as target of the optimisation problem.

### 3.5.2 Optimisation Problem 1

**Description** Before going further, the notation used to describe the parameters and vectors of BIRDIE needs to be reminded. We refer to  $X = \{X_1, X_2, \dots, X_{N-1}, X_N\}$ , where  $N$  is the  $X$  length, as the vector of vectors representing the target,  $\tilde{X} = \{\tilde{X}_1, \tilde{X}_2, \dots, \tilde{X}_{N-1}, \tilde{X}_N\}$  as the vector of vectors to be optimised, and  $\Theta = \{\tilde{\theta}_1, \tilde{\theta}_2, \dots, \tilde{\theta}_{N-1}, \tilde{\theta}_N\}$  as the parameters uniquely bounded to the vector of vectors  $\tilde{X}$ .

The target  $X$  of this problem is composed of 2 vectors  $X_1$  and  $X_2$ : the distribution of the experimental pressure coefficient (i.e. extracted from the pETW database) and the numerical skin friction coefficient extracted from ISES, both for the C2 profile in transonic conditions. The vector to be optimised  $\tilde{X}$  is the  $C_p$  and  $C_f$  evolution calculated by elsA. The  $\Theta$  parameters to be optimised are the constants of the Spalart-Allmaras model. Several combinations of constants have been tested.

Due to findings in the work previously performed, also the skin friction coefficient, extracted from ISES, has been imposed as a target of the optimisation and not only the experimental pressure distribution. In fact, it has been discovered that if only the pressure distribution around the profile is set as a target, the new set of coefficients yielded to shear stresses about *two* times larger than using the standard coefficients. Thus, it is expected, and also formerly been obtained in the previous investigations, that BIRDIE will find a set of coefficients that produces more coherent shear stresses with this formulation.

**Numerical and Physical Setup** The main characteristics of the numerical setup is described at the head of the chapter.

The grid used is the one obtained from the Grid Convergence exercise described in *Section 3.3*. The only difference is (clearly) in the turbulence model: different combinations of constants will be varied to perform the optimisation problem.

In order to speed up convergence, an initial solution has been used for the numerous simulations performed with elsA. This initial solution refers to the flow-field calculated with the standard constants of the SA model. It is therefore complicated to rely on the residuals of the RANS equations to evaluate convergence. Hence, since Rizzi Method has been guaranteeing a reliable  $y^+$  distribution, the convergence criterion becomes the monitoring of the aerodynamic coefficients. If the aerodynamic coefficients vary less than 0.1 % in the final numeric temporal iterations, the simulation is considered converged. For instance, for RAE2822 profile, 2000 iterations are needed, while for C2 about 6000, which corresponds to about 2 and 6 minutes of computational time. The latter is a very important factor when it comes to data assimilation, where numerous simulations are necessary to undertake the optimisation process.

The aerodynamic aerodynamic state chosen corresponds to the largest discrepancy between elsA and the pETW database, found in the database mapping *Section (4.3)*:  $Re = 15.7 \cdot 10^6$ ,  $M_a = 0.724$  and  $\alpha = 0.68^\circ$ .  $C_p$ ,  $C_f$  and  $H_k$  for this state are presented in figures 4.13b, 4.15b and 4.17b.

**Set of SA Constants assimilated** We recall the *standard* value of the SA turbulence model constants used for performing the data assimilation in table 3.5.  $\kappa$  is not present in the table since it can not be modified in

the elsA version used to accomplish this exercise.

Constant	Value
$c_{b1}$	0.1355
$c_{b2}$	0.622
$\sigma_P$	2/3
$c_{w1}$	3.24
$c_{w2}$	0.3
$c_{w3}$	2.0
$c_{v1}$	7.1

Table 3.5: Spalart-Allmaras turbulence model constants

Various combinations of constants were tested in order to analyse their effects on the flowfield around the profile and its convergence. They are reported in table 3.6.

Name	$\tilde{\Theta}$
Set1	$c_{v1}, c_{w2}, c_{w3}$
Set2	$c_{b1}, c_{b2}, \sigma_P$
Set3	$c_{b1}, c_{b2}, c_{v1}$
Set4	$c_{b1}, c_{b2}, c_{v1}, c_{w2}$
Set5	$c_{b1}$
Set6	$c_{b2}$
Set7	$c_{v1}$
Set8	$c_{b1}, c_{b2}$
Set9	$c_{b1}, c_{b2}, c_{w3}$

Table 3.6: Set of SA turbulence model constants chosen to perform the data assimilations

The relation between the destruction term  $c_{w1}$ , the production term  $c_{b1}$ , the diffusion term  $c_{b2}$  and  $\sigma_P$ :  $c_{w1} = c_{b1}/\kappa^2 + (1 + c_{b2})/\sigma_P$  has been considered as a constraint, i.e.  $c_{w1}$  has not been assimilated. This decision has been made on the assumption that not respecting the equilibrium between production, dissipation and diffusion was an approach excessively numerical and not sufficiently physical. Hence, since the destruction term is a function  $c_{w1} = f(c_{b1}, c_{b2}, \sigma_P)$ , its value updates with each iteration of all set of coefficients with exception to "Set1".

**Discrepancy Metric  $\sigma$**  The discrepancy metric defined in 4.3 has been utilised to evaluate the iterations of the optimisation process. We recall its expression here.

$$\sigma = \sqrt{\frac{1}{N} \cdot \sum_i^N (y_{1i} - y_{2i})^2} \quad (3.6)$$

where  $y_1$  and  $y_2$  are the vectors to compare and  $N$  the vector length. This variable has been used to trace the convergence trend in the different iterations of BIRDIE. It has been chosen to use  $\sigma$  in lieu of the distance provided by BIRDIE in order to measure the influence of the pressure side (PS) and the suction side (SS) on the total discrepancy, as done during the database mapping described in previous sections. This time, however,  $\sigma$  has been calculated not only for  $C_p$  distribution but  $C_f$  as well. Summarizing, the results of  $\sigma$  have been calculated with respect to the evolution of  $C_p$  on PS, SS and along the whole profile and with respect to  $C_f$  on PS, SS and along the whole profile.

**BIRDIE** In order to provide  $X$  and  $\tilde{X}$  vectors to BIRDIE, the same interpolation performed in the pETW database mapping, described in *Section 3.4.2.3*, was carried out. Indeed, whilst the experimental  $C_p$  is the original from pETW database, all other vectors ( $C_f$  from ISES,  $C_p$  from elsA and  $C_f$  from elsA) were interpolated along locations of the C2 pressure tappings. In addition, two further manipulations were applied to the wall friction coefficients.

1. Since BIRDIE weighs the absolute value of the vector components,  $C_f$  was divided by a factor of 4000, in order to have the same order of magnitude as the pressure coefficient distribution  $C_p$ , and thus to have the same weight in finding the optimal point.
2. As the shock alters the distribution of  $C_f$  on the SS quite significantly, it has been considered to pick  $C_f$  for  $x/c < 0.4$  and  $x/c > 0.8$ , in order to avoid this distortion. Not having done thus, BIRDIE would have calculated a large distance between the target  $C_f$  of ISES and the  $C_f$  of elsA due to the shock only. Our intention, however, is to find a distribution that globally makes physical sense.

These adjustments are represented in figures 3.6 and 3.7.

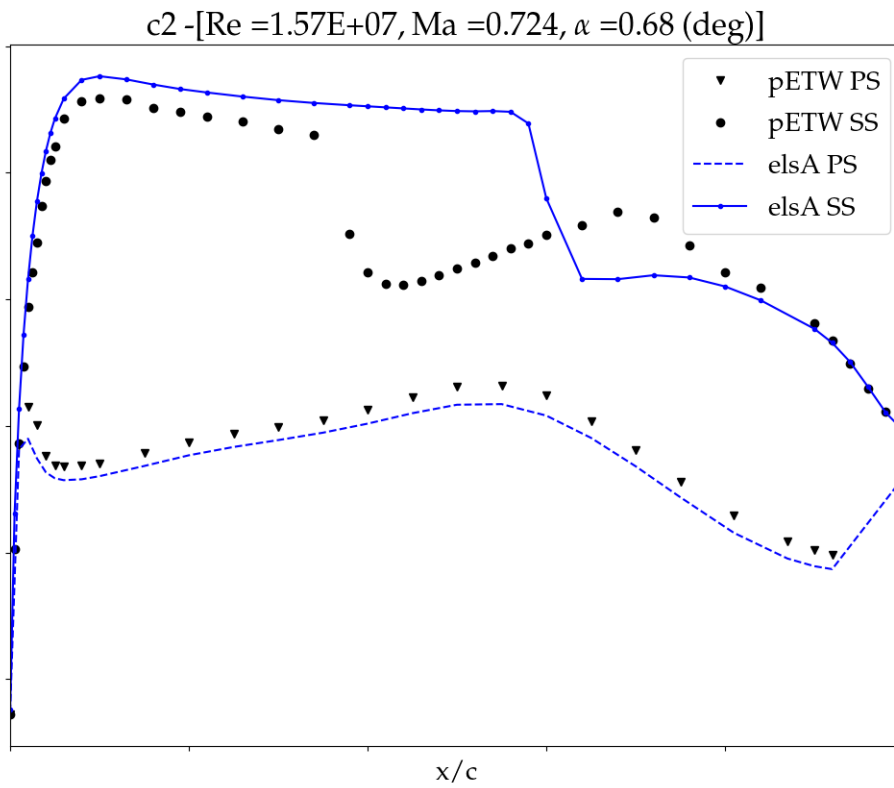


Figure 3.6: Example of  $C_p$  treatment for BIRDIE optimisation

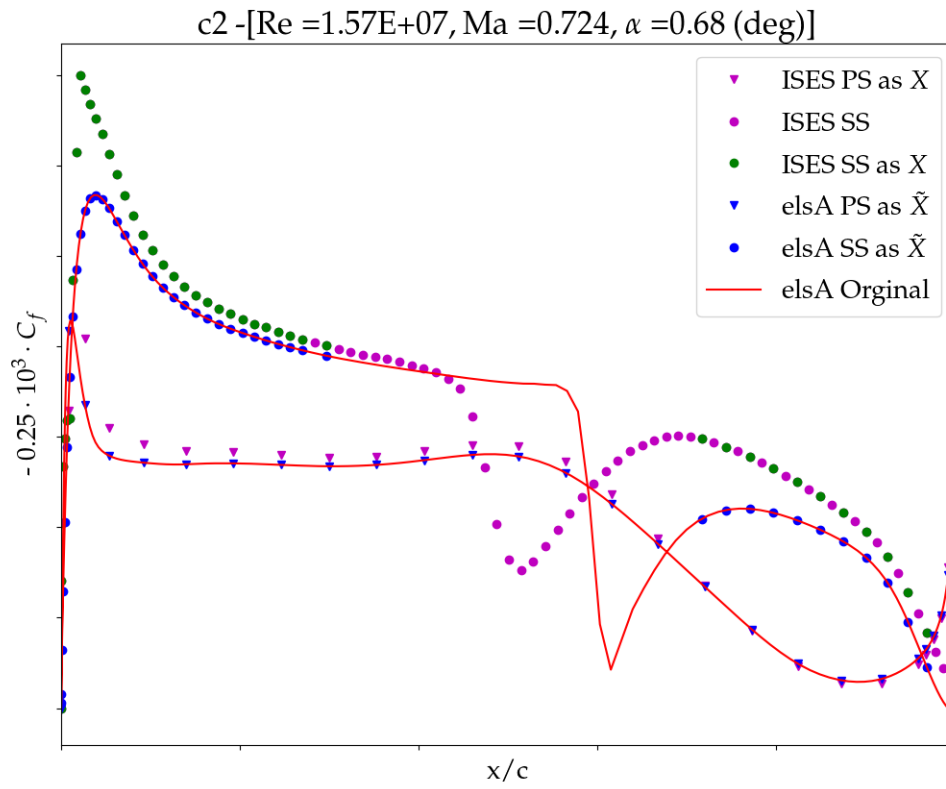


Figure 3.7: Example of  $C_f$  treatment for BIRDIE optimisation

### 3.5.3 Optimisation Problem 2

**Description** This optimisation problem is defined exactly as the former one. Considering the excellent results obtained with the SA model constants in "Set3" ( $c_{b1}, c_{b2}, c_{v1}$ ), different aerodynamic conditions have been tested for C2 and EFT airfoil with this combinations of SA constants. These conditions have been picked up from the pETW database and are presented in table 3.7.

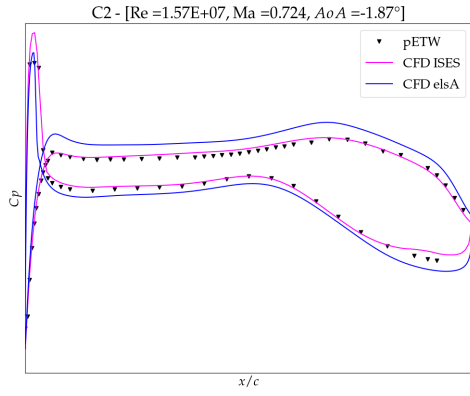
Name	Airfoil	$Re \cdot 10^6$	$M_a$	$\alpha[^\circ]$
Assimilation1	C2	15.7	0.724	-1.866
Assimilation2	C2	11.83	0.505	2.149
Assimilation3	C2	9.01	0.745	0.7941
Assimilation4	C2	15.7	0.749	-0.6572
Assimilation5	EFT	15.55	0.727	1.0906
Assimilation6	EFT	15.55	0.747	0.9772
Assimilation7	EFT	8.94	0.747	0.9838

Table 3.7: Aerodynamic conditions of Optimisation Problem 2

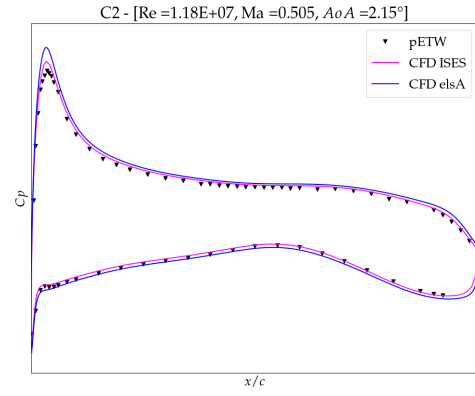
The principal aim is to analyse how the results of the data assimilation vary with geometry and aerodynamic conditions.

- Assimilation 1: negative alpha effects;
- Assimilation 2: subsonic flow;
- Assimilation 3: smaller Reynolds number;
- Assimilation 4: particular  $C_p$  distribution;
- Assimilation 5: different geometry compared to C2;
- Assimilation 6 and 7: effects of Reynolds number at the constant  $M_a$  and  $\alpha$ .

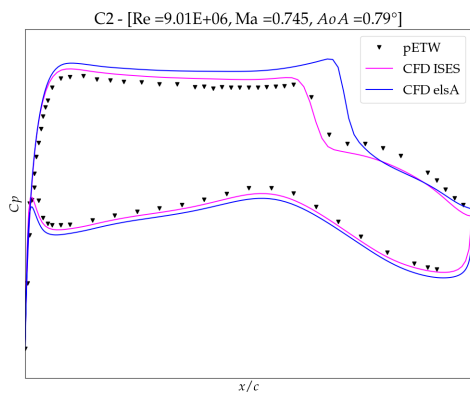
The pressure fields related to these aerodynamic conditions are represented in figure 3.8. All of them are present except for Assimilation4 one, as it will be represented directly in the section results.



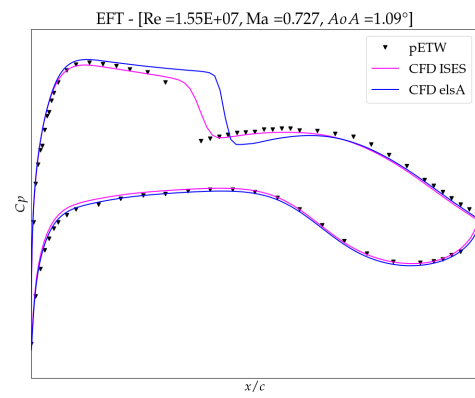
(a) Assimilation1



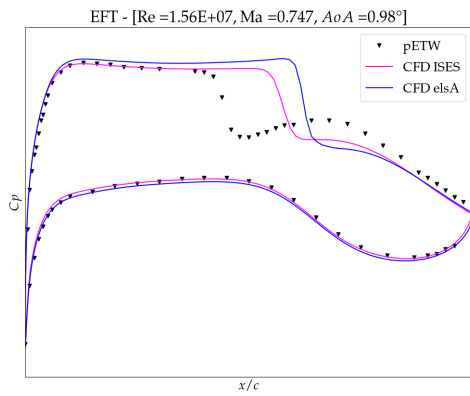
(b) Assimilation2



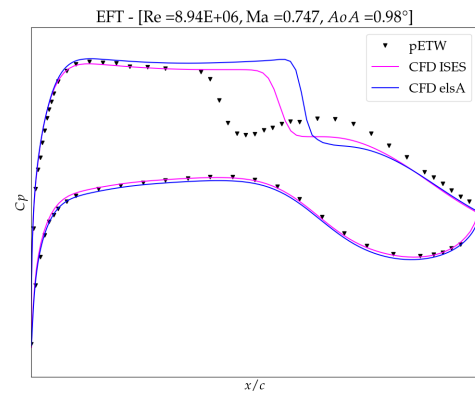
(c) Assimilation3



(d) Assimilation5



(e) Assimilation6



(f) Assimilation7

Figure 3.8:  $C_p$  distributions related to different aerodynamic conditions and airfoils

### 3.5.4 Optimisation Problem 3

**Description** The target  $X$  is formed by 3 vectors ( $X_1, X_2$  and  $X_3$ ): the former vectors in "Optimisation Problem 1" and the skin friction evolution calculated with elsA for the RAE2822 profile in subsonic conditions with the standard set of coefficients of the Spalart-Allmaras turbulence model.

To the former  $\tilde{X}$  has been added the skin friction coefficient distribution calculated for RAE2822 profile with a non-standard set of the SA turbulence model constants.

In fact, with a set of coefficients obtained from "Optimisation Problem 1" ("Set3"), a simulation of a RAE2822 profile in subsonic conditions was performed. A quite important discrepancy was found between the results obtained with the standard coefficients and those with the new ones, hence it has been decided to impose as a target the  $C_f$  obtained with the reference SA turbulence model.

**Numerical and Physical Setup** Concerning C2 airfoil simulations, none of the characteristics described in "Optimisation Problem 1" has changed.

As regards the simulations carried out on the RAE2822 profile, the same numerical setup and mesh, used for the C2 profile, were adopted.

The selected aerodynamic conditions for RAE2822 were extracted from the pETW database and are:  $Re = 3.57 \cdot 10^6$ ,  $M_a = 0.246$  and  $\alpha = 2.65^\circ$ .

**SA Constants** Evidently "Set3", i.e. Spalart-Allmaras model constants  $c_{b1}, c_{b2}$  and  $c_{v1}$ , has been chosen to perform this assimilation.

**Discrepancy metric  $\sigma$**  As in Optimisation problem 1, the  $\sigma$  contribution of  $C_f$  on PS, SS and over the entire RAE2822 profile has been calculated.

**BIRDIE** The skin-friction coefficient distribution on RAE2822 airfoil has been interpolated on the pressure tapping location along the chord of C2 airfoil, as it has been done for  $C_p$  interpolation.

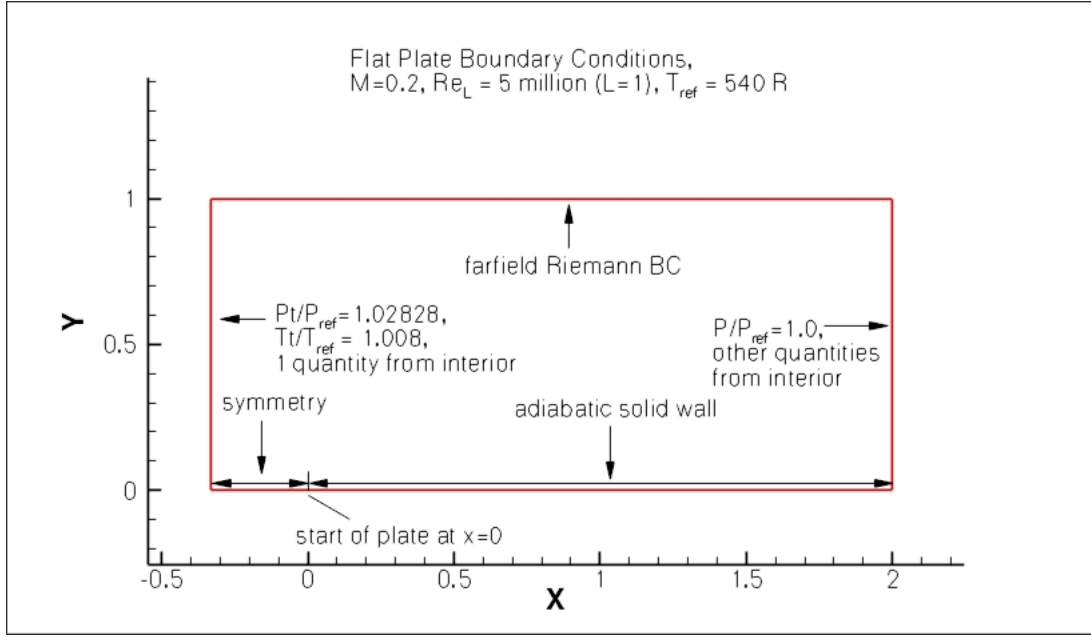


Figure 3.9: Flat Plate main characteristics (extracted from [4])

### 3.5.5 Optimisation Problem 4

**Description** The target  $X$  is formed by 4 vectors ( $X_1, X_2, X_3$  and  $X_4$ ): the former 3 vectors of "Optimisation Problem 3" and velocity profile for a flat plate in subsonic condition calculated with **standard SA model constants**. The vector of vectors  $\tilde{X}$  to be optimised corresponds to the former optimisation formulation with the addition of the velocity profile of a flat plate in subsonic conditions with a non-standard set of the SA turbulence model constants.

In a similar vein as the previous case, with the set of coefficients obtained from Optimisation Problem 1 and 3, simulations of a flat plate in subsonic condition were carried out in order to analyse its BL properties with the assimilated SA constants. The test case full description is given in [4]. A significant discrepancy was found between the results obtained with the standard coefficients and those with the new ones, hence the reference velocity profile has been imposed as a target.

**Numerical and Physical Setup** Concerning RAE2822 and C2 profiles, the aerodynamic regime and numerical properties have remained unchanged. About the flat plate, a test case provided by NASA has been utilised. Its boundary conditions, domain dimensions and aerodynamic conditions are represented in the figure 3.9. The angle of attack used is  $\alpha = 0^\circ$ . However, the domain dimensions used in this exercise have been scaled by a factor 1000 with respect to NASA test case.

The mesh used,  $258 \times 33 \times 2$  ( $I \times J \times K$ ), along the  $x$ -axis presents a local refinement at the leading edge, and then has a uniform distribution downstream. Following the  $y$ -axis, close to the wall has an exponential refinement which allows to have enough points in the boundary layer as well as guaranteeing  $y^+$  of the order of unity. A representation of the calculation grid is shown in figure 3.11. On the top half of the illustration one can see the mesh discretization at the trailing edge, while on the bottom one a global view of the mesh.

**SA Constants &  $\sigma$**  The "Set3", consisting of  $c_{b1}, c_{b2}, c_{v1}$  constants, has been chosen to perform this exercise. The convergence of the optimisation process was tracked through the discrepancy metric  $\sigma$  calculated for the flat plate as well.

**BIRDIE** The velocity profile vector, used as a target  $X$  and as an input  $\tilde{X}$ , has been extracted from the position  $x = 0.97$ . As in the case of the skin friction coefficient, some manipulations have been necessary so that  $X$  and  $\tilde{X}$  could be properly used in BIRDIE.

1.  $U^+$  extraction. Since the distribution in the boundary layer, in the direction normal to the wall  $y$ , is different (denser) than pressure trappings one of profile C2, an extraction of some  $U^+$  points proved necessary. An exponential distribution was attempted, in order to extract points from all characteristic parts of the boundary layer: viscous sub-layer, buffer layer, log-zone and outer layer. This spatial distribution can be observed in figure 3.10.

- Variable rescaling. Both  $U^+$  and  $y^+$  have been rescaled to have values around unity. This is due to the fact that, as mentioned before, BIRDIE weighs the absolute value of the  $X$  and  $\tilde{X}$  components researching the optimum point. However, it was deliberately chosen to have a higher value than the other vectors, essentially giving more weight to the flat plate target than to the others. The factor for  $U^+$  is  $1/2.5$  while for  $y^+$  is  $1/10^5$ .

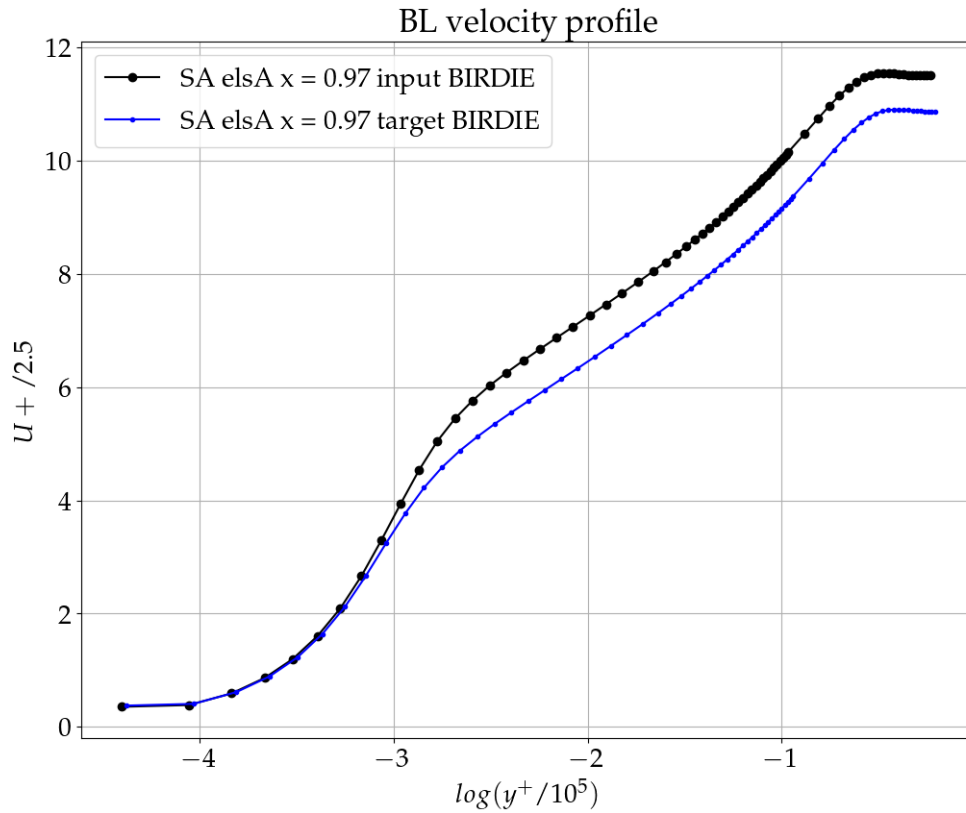


Figure 3.10: Example of  $X_4$  (target BIRDIE) and  $\tilde{X}_4$  (input BIRDIE) of Optimisation Problem 4

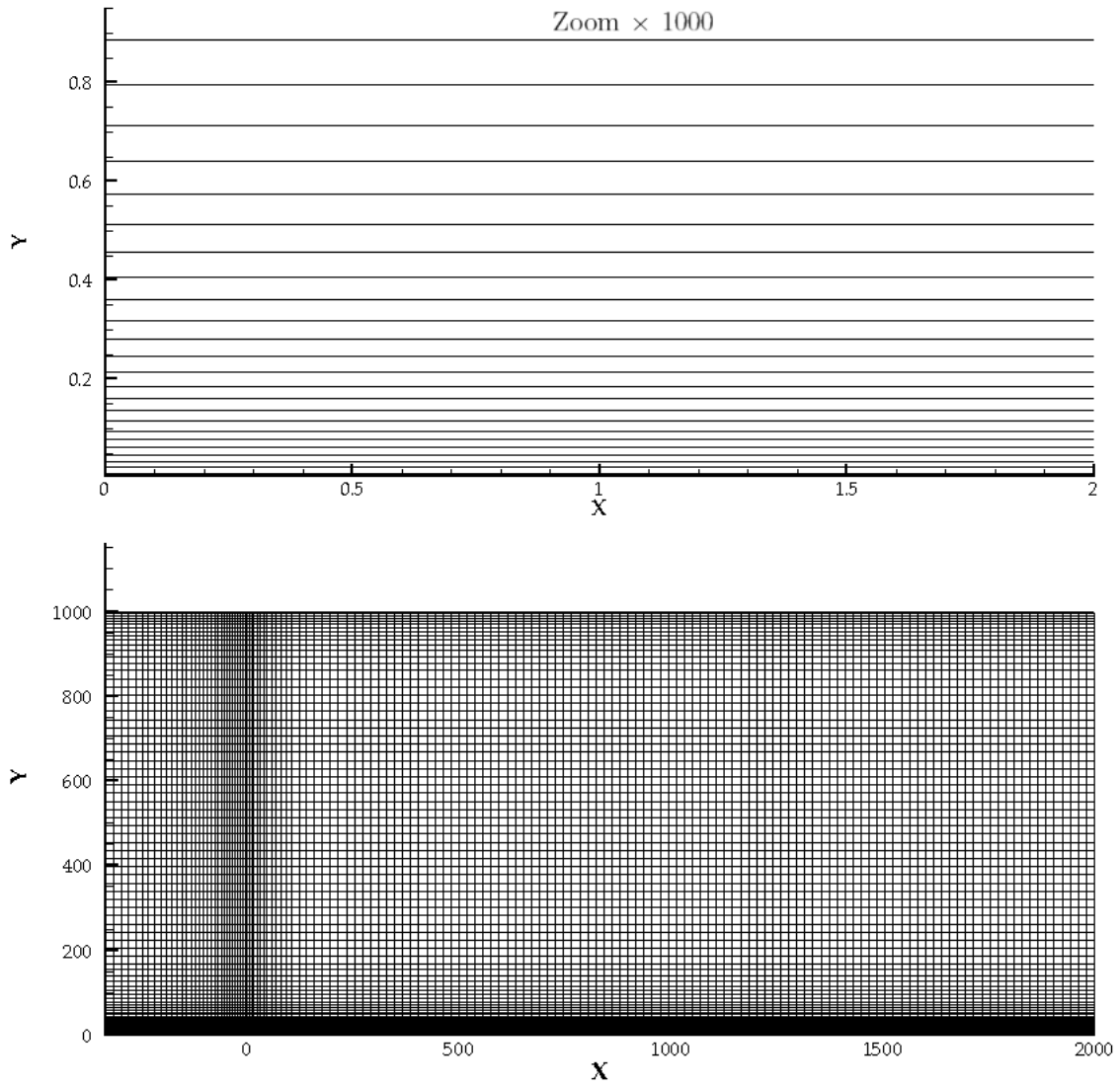


Figure 3.11: Flat Plate Grid

# Chapter 4

## Results

### 4.1 Profil\_12 Design

In this section, the results of the procedure described in *Section 3.2* are reported.

At first, the results about Profil\_1 geometry will be shown, compared it with that of profile RAE2822. Afterwards, a short analysis on the simulation results obtained by elsA and ISES will be made, with particular attention on the distribution of the pressure and skin friction coefficient and some integral quantities of the boundary layer. Thus, a similar analysis will be pursued on the iterations that led to the definition of the final geometry of Profil\_12.

#### 4.1.1 Intermediate Airfoil Profil\_1 Design

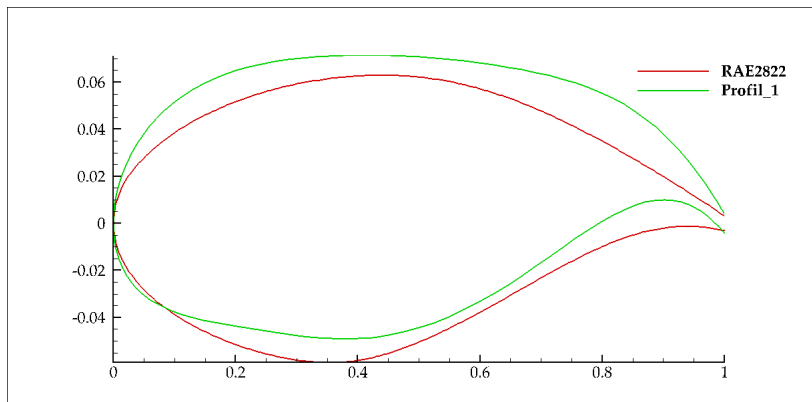


Figure 4.1: Profil\_1 Geometry

#### Profil\_1 Geometry

**Numerical Convergence** Throughout the various simulations, RANS equations residuals were appropriately monitored, as well as the non-dimensional wall distance  $y^+$ . In fact, it was verified that the residuals were reduced by no less than 4 orders of magnitude. Through the formulation defined in *Section 3.1* to define the thickness of the first cell at the leading and trailing edge, a value of  $y^+$  around 0.2 was obtained. This was considered adequate for the turbulence model used. Two examples of residuals and non-dimensional wall distance are shown in figure 4.2. While in fig. 4.2a  $y^+$  evolution over the airfoil chord has been presented, in fig. 4.2b mass conservation and Spalart-Allmaras turbulent equation residuals have been shown.

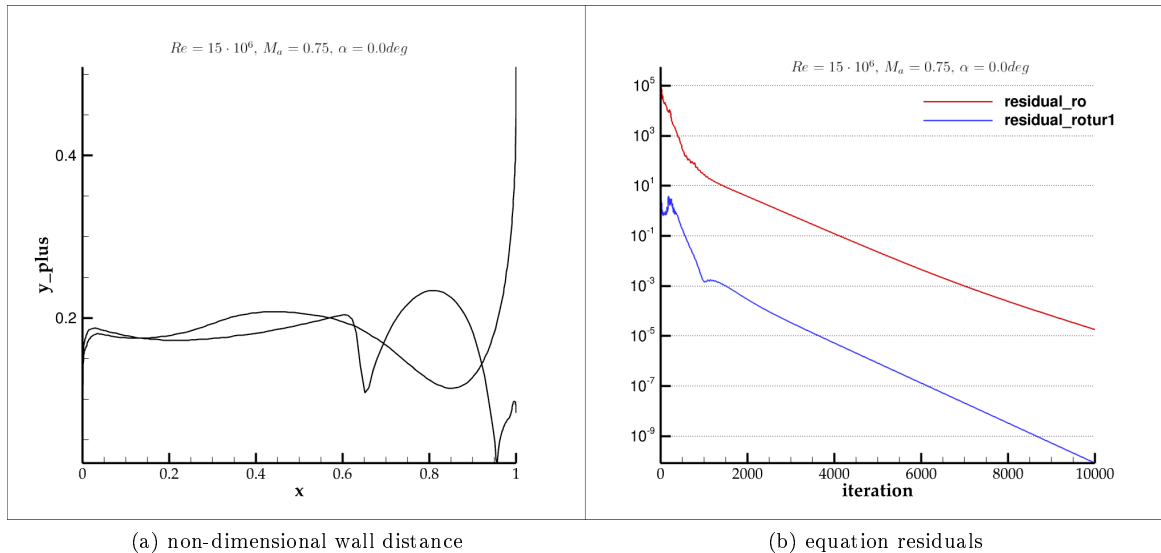


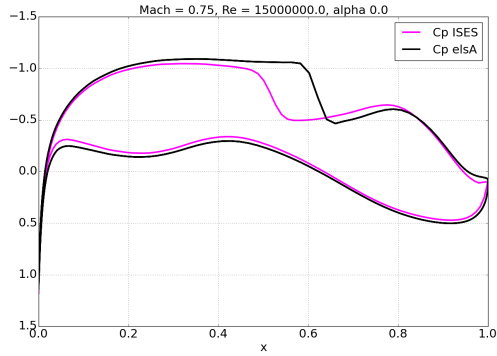
Figure 4.2: Non-dimensional wall distance and equation residuals examples for Profil\_1 simulations

**Grid Results Comparison** Results of Mesh 2 and Mesh 3 elsA simulations have been compared for the aerodynamic conditions  $Re = 15 \cdot 10^5$ ,  $Ma = 0.75$  and  $\alpha = 0.0^\circ$ . Mesh 3 is approximately 10 times finer than Mesh 2, thus this comparison can be considered as a verification of the results consistency. If no particular differences occur between the presented results, then Mesh 2 can be considered reliable enough for calculating the other aerodynamic conditions and airfoil geometry. In fact, very few simulations were run with Mesh 3, due to the significant computational cost involved. The comparison between the results obtained with these 2 meshes are shown in figure 4.3. The curves showing the characteristics of the boundary layer and the flow field were chosen according to a simple criterion: where the results between ISES and elsA differ the most, as this is the purpose of this profile design. In fact, in fig. 4.3 the distributions of the pressure coefficient  $C_p$ , the skin friction coefficient  $C_f$  on the suction side (SS) and kinematic shape factor  $H_k$  on the pressure side (PS) of Mesh 2 (respectively figures 4.3a, 4.3c and 4.3e) and "Mesh 3" (respectively figures 4.3b, 4.3d and 4.3f) are shown.

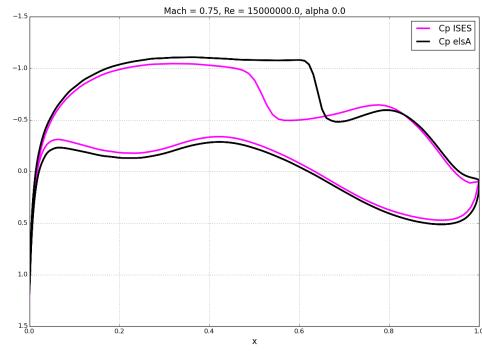
No substantial difference can be seen from the figures just presented. This allowed us to select Mesh 2 for the remaining simulations.

Hence, one can note that Profil\_1 already represents a success with respect to the goal set: generating a profile that produces large discrepancies between the predictions of elsA and ISES softwares. In figure 4.3a, a large difference in the shock position can be noticed. Moreover, elsA overestimates the pressure on the airfoil PS with respect to ISES prediction. From figure 4.3c, one can notice a larger  $C_f$  downstream of the shock in ISES than elsA. Lastly, figure 4.3e shows how the kinematic shape factor on the profile PS differs between the simulations results. In fact, it is precisely where the peculiarity of this profile is concentrated, i.e. the large rear-loading, that the greatest discrepancies are noted, with elsA underestimating the latter with respect to ISES.

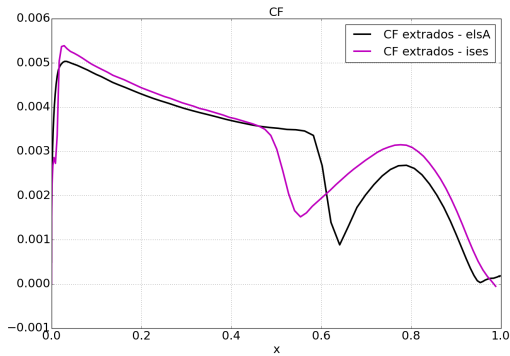
Contrasts of this nature were also noted in previous investigations done here at ACI, and described in the technical reports [2] and [18], when they compared ISES and elsA results on C2 profile. Thus, this suggests that Profil\_1 may be as problematic as the pETW airfoils for elsA, which is the quality we look for.



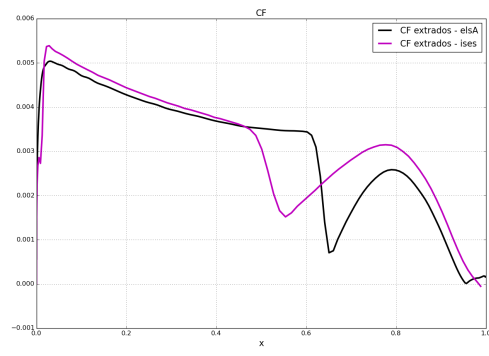
(a) "Mesh 2"  $C_p$  over the airfoil Profil\_1 chord



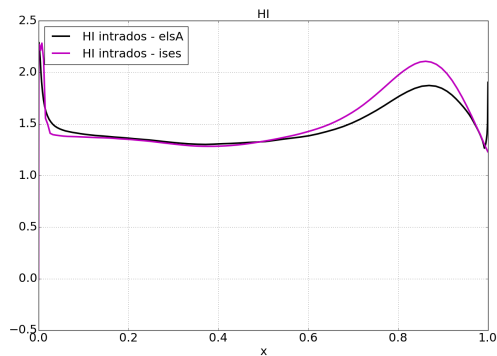
(b) "Mesh 3"  $C_p$  over the airfoil Profil\_1 chord



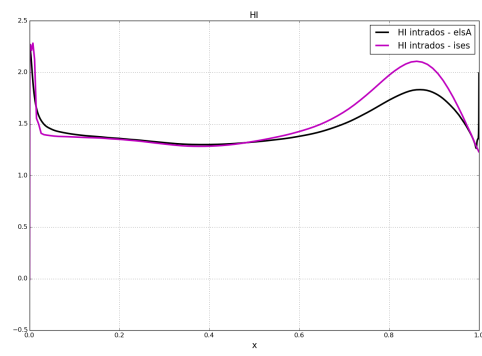
(c) "Mesh 2"  $C_f$  (SS) over the airfoil Profil\_1 chord



(d) "Mesh 3"  $C_f$  (SS) over the airfoil Profil\_1 chord



(e) "Mesh 2"  $H_k$  (PS) over the airfoil Profil\_1 chord



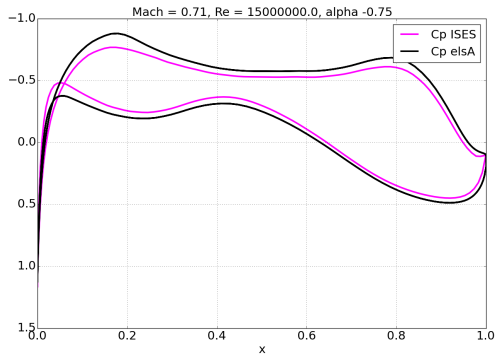
(f) "Mesh 3"  $H_k$  (PS) over the airfoil Profil\_1 chord

Figure 4.3: Flow field and boundary layer characteristic of Profil\_1 simulations for different grids

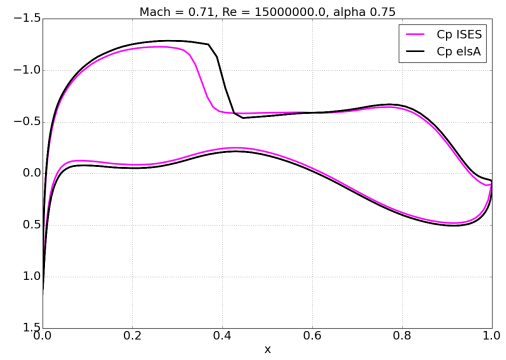
**$M_a$  and  $\alpha$  effects on Profil\_1** In fig. 4.4, the pressure field trend, on Profil\_1 airfoil, with the Mach number and the angle of attack is displayed.

In fig 4.4a,  $M_a = 0.71$  and  $\alpha = -0.75^\circ$ , a slight discrepancy between the predictions of ISES and elsA is present despite no shock has been reached. In fact, elsA tends to overestimate the pressure field both on the SS (in absolute value) and on the PS.

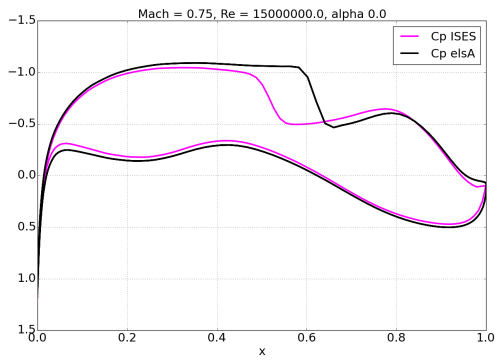
In fig 4.4b, having constant Mach number but with a larger angle of attack, the shock has appeared and a slight difference in its position between the numerical solutions can be noted. This gap rises at  $M_a = 0.75$  and  $\alpha = 0.0^\circ$ , fig. 4.4c, but it decays when the boundary layer detaches from the airfoil due to a stronger shock in fig. 4.4d.



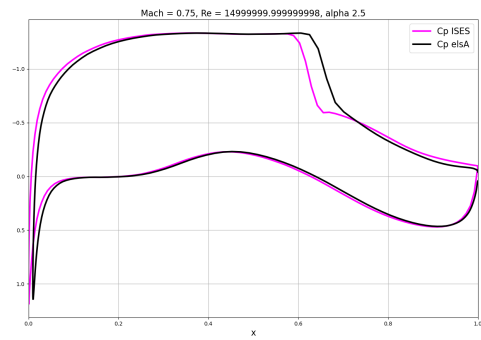
(a)  $C_p$  evolution at  $(M_a = 0.71, \alpha = -0.75^\circ)$



(b)  $C_p$  evolution at  $(M_a = 0.71, \alpha = 0.75^\circ)$



(c)  $C_p$  evolution at  $(M_a = 0.75, \alpha = 0.0^\circ)$



(d)  $C_p$  evolution at  $(M_a = 0.75, \alpha = 2.5^\circ)$

Figure 4.4:  $C_p$  distribution of Profil\_1 at different aerodynamic states

### 4.1.2 Final Airfoil Profil\_12 Design

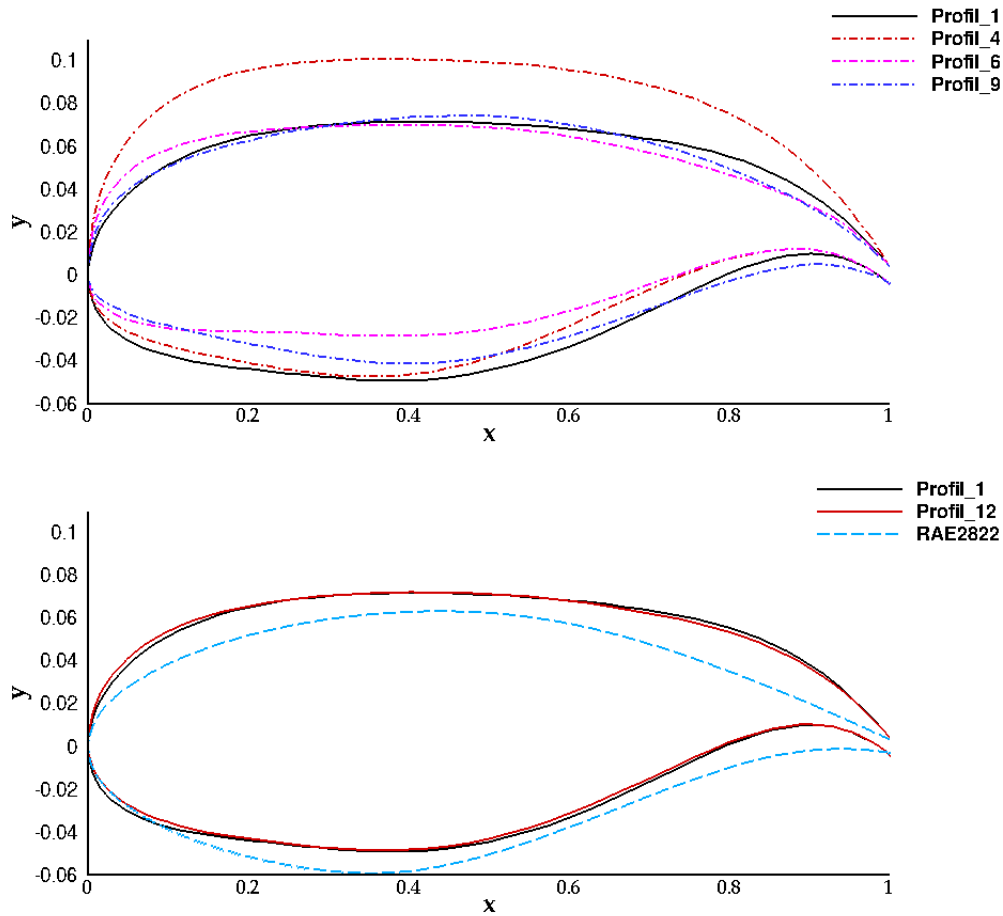


Figure 4.5: Airfoils tested during this design process. At the top there 4 intermediate profiles are shown. At the bottom Profil\_1, Profil\_12 and RAE2822 airfoils are presented.

As already mentioned, several geometric variations were carried out with the intention of studying their effects on the shock position and attempting to increase the difference between ISES and elsA predictions. This yielded to 12 iterations. Boundary layer separation and/or residuals divergence occurred during this process. Some intermediate geometries obtained (Profil\_4, Profil\_6, Profil\_9) are shown in the upper part of fig. 4.5, while the final one (Profil\_12) is presented in the lower part.

Some particularities of these geometries are:

- Profil\_4: thickness distribution more important than Profil\_1.
- Profil\_6: thinner and more cambered at the leading edge than Profil\_1.
- Profil\_9: slightly thinner and less aft-cambered than Profil\_1. In addition, significantly different PS between them.
- Profil\_12: tiny differences at the leading and trailing edges compared to Profil\_1.

The performance of these profiles have been studied at constant Mach and Reynolds numbers,  $M_a = 0.75$  and  $Re = 15.0 \cdot 10^6$ , but in a variety of angles of attack. However, for the sake of brevity, in figure 4.6 pressure coefficient distributions of four airfoils introduced above have been compared only at  $\alpha = 0.0$ . Profil\_4 (fig. 4.6a) and Profil\_6 (fig. 4.6b) have been predicted by ISES and elsA codes with better consistency with respect to the other airfoils. Having analysed  $C_f$  evolution on the SS (not shown here), both ISES and elsA did not predict BL separation. Moreover, they computed a slight contrast in shock position and are in good agreement in the calculation of the  $C_p$  on the PS. Thus, they are of low interest.

The two softwares have had more difficulties in coherently computing the pressure field around Profil\_9, fig 4.6c. Despite the shock location is quite similar, a general overestimation of the  $C_p$  distribution of elsA calculation with respect to ISES one is present. In view of the geometric resemblance of Profil\_12 to Profil\_1, the results

of numerical simulations between these two profiles are very similar. However, in figure 4.6d, it can be noted that both elsA and ISES compute for Profil\_12 the shock position more downstream than for Profil\_1.

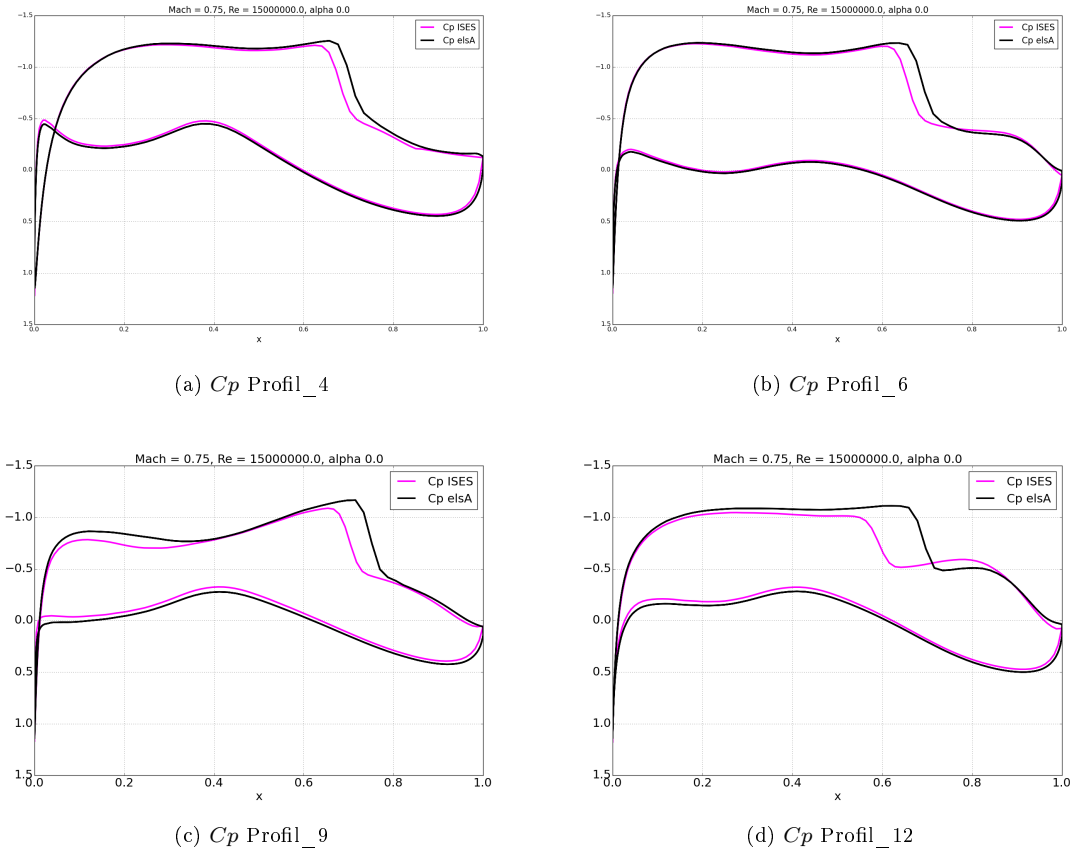


Figure 4.6:  $C_p$  distribution of intermediate and final airfoils

### 4.1.3 Conclusion

Generally speaking, the objectives set at the beginning of this section have been fulfilled. Several numerical simulations have been executed on elsA, familiarising the author with this tool. To be fair, engineer Quentin Bennehard simplified the author's task by providing Python functions which allowed to run simulations on a distant supercomputer quite quickly.

BIRDIE has proved to be an interesting and useful tool, capable of solving the optimisation problem in a few iterations and with remarkable results. An airfoil producing large discrepancies on flow-field characteristics between the elsA and ISES CFD codes has been found. Further analysis on this profile will be done in the section dedicated to the mapping of the pETW database.

Conclusively, it is worth noting that despite these discrepancies have been found to vary widely in different iterations, they have remained consistently present. Since the only common feature of the tested profiles is a strong rear-loading, we can affirm that the previous hypothesis has been verified.

## 4.2 Grid Convergence

This section details the results from the grid convergence exercise. The approach adopted to achieve them is described in *Section 3.3*. Initially, illustrations of the convergence criteria imposed on all the simulations performed will be shown. The trend of pressure and viscous wall stresses will be compared between the different grids, as well as the velocity profile within the boundary layer in 6 precise locations around the airfoil. Afterwards, the results of the Grid Convergence Index (GCI) and Far-Field Drag (FFD) analysis will be shown and commented. Finally, the choice of the grid that will be used to map the reliability of the CFD codes, with the purpose of well reproducing the experimental data contained in the pETW database, will be carried out and justified.

### 4.2.1 Convergence Results

In fig 4.7, some illustrations of the convergence criteria fulfilment are shown. In fig. 4.7a, the residuals decayed by at least 6 orders of magnitude. In fig. 4.7b,  $y^+$  is in the range of unity (therefore in the validity range of the turbulence models) and in fig. 4.7c the relative error of the aerodynamic coefficients is reduced by at least 8 orders of magnitude, reaching even the machine error (and therefore not depicted in the image).

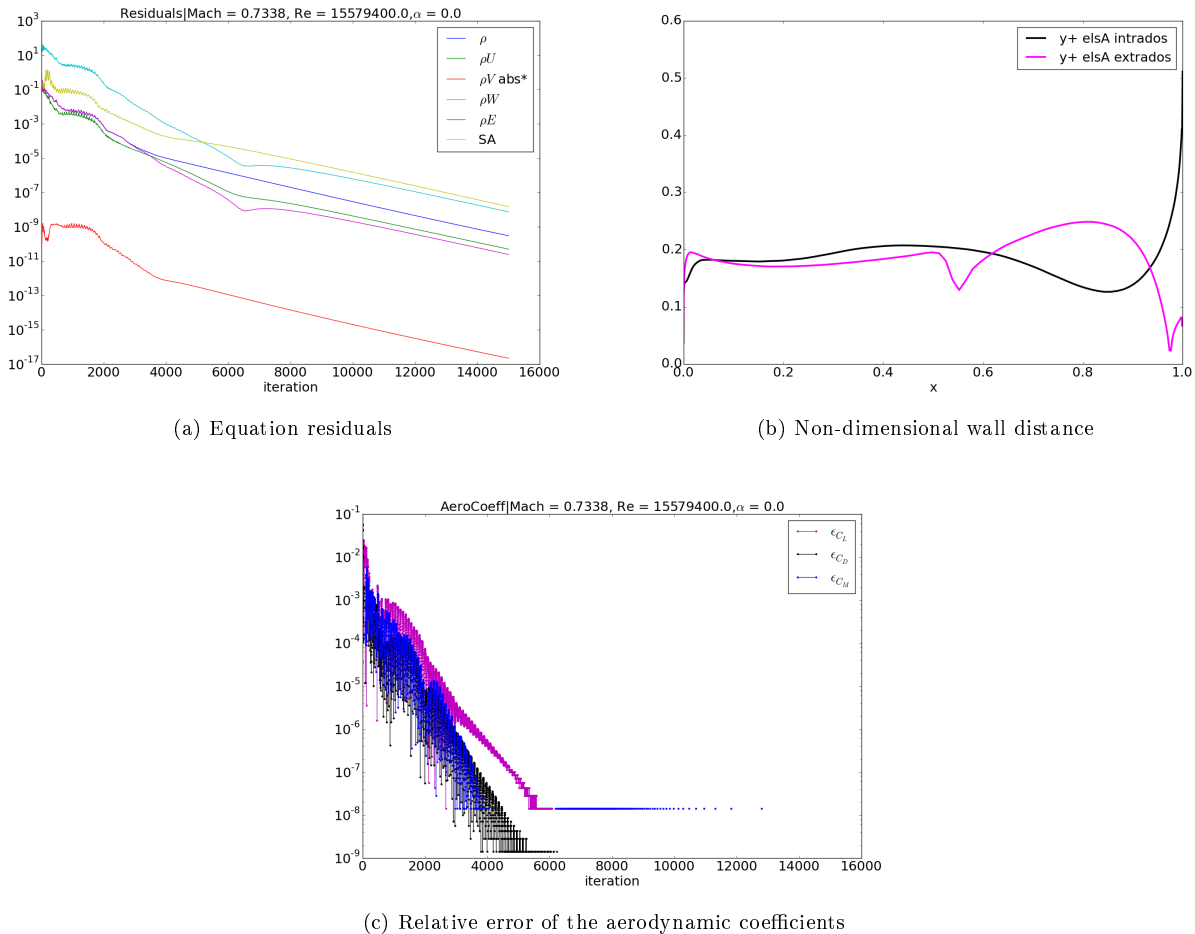


Figure 4.7: Non-dimensional wall distance, aerodynamic coefficient relative errors and equation residuals instances

### 4.2.2 Flow-Field Comparison

A comparison of the evolution of the pressure and wall friction coefficients is given in fig. 4.8. The selected grids correspond to iteration number 1,4,7 and 12. For both coefficients, the same observations can be made: simulations calculated on Grid1 produce results unacceptable compared to the finest grid. These deviations are reduced for Grid4, and then become almost imperceptible for Grid7 and finer grids.

The non-dimensional velocity  $U^+$  has been extracted at appropriate positions around the airfoil for the various simulations. Its definition is here recalled:

$$U^+ = \frac{U}{u_*} \quad (4.1)$$

where  $u_*$  is the friction velocity,  $u_* = \sqrt{\tau_w/\rho}$ .

These positions are listed in the table 4.1 and shown in fig. 4.9. Three positions have been chosen on the PS and three on the SS. On the PS, two out of three points are voluntarily close to the rear-loading. The aim is that the velocity profile does not vary as a function of the grid size, in particular at this position which is assumed to cause problems for numerical solvers. The third position on the PS is  $x/c = 0.4$ , where the flow should not be overly complex to compute. On the SS, the non-dimensional velocity profile has been extracted shortly after the leading edge, upstream and downstream of the shock. The results of these extractions are shown in figure 4.10.

BL position extraction	
$x_{PS}/x$	$x_{SS}/c$
0.4	0.1
0.8	0.4
0.9	0.85

Table 4.1:  $x$  coordinate of the velocity profile extraction. Leftmost column corresponds to the  $x$  coordinate on the airfoil pressure side (PS) while rightmost on the suction side (SS)

Only results for Grid1, Grid4 and Grid7 are shown. Since Grid7 and Grid12 results are always superposed, it's impossible to distinguish the curves, hence Grid12 is not shown.

A Cassiopee ([22]) function called "ExtractMesh" was used to extract these velocity profiles, which interpolate adequately the center cell values of the cell close to the airfoil wall.

The characteristic sub-layers within the boundary layer can be distinguished, i.e viscous sub-layer, buffer layer, log zone and outer layer.

However, one can notice that Grid1 shows the first point outside the log-zone, despite its first cell is a  $y^+ \approx 0.2$ . This is due to the excessive thickness of the closest cells to the airfoil wall, which does not allow to ExtractMesh to interpolate properly. Grid4, on the other hand, has enough points in the log-zone but few units in the buffer layer and viscous sublayer. Finally, Grid7 present satisfactory velocity trends, proving to have a grid points distribution dense enough even at such low  $y^+$  values. Furthermore, one can remark the excellent robustness of the SA model which, even for grids with relatively few points near the wall, manages to give quite consistent results in the outer layer.

### 4.2.3 Aerodynamic Coefficients

In table 4.3, the main aerodynamic coefficients calculated by elsA for each grid are shown. Figure 4.11 displays the latter but normalised with respect to the value obtained for the finest grid (Grid12). In addition, its y-axis has as lower and upper limits the values of 99% and 101%.

One can notice that aerodynamic coefficient values are strongly variable in the first grid iterations. While the drag coefficient stabilises from the fifth iteration onwards, the lift and momentum coefficients present a more pronounced variation. This variation is much reduced from the seventh iteration onwards, as all 3 coefficients retract in the range of 0.5% from the final value.

### 4.2.4 Grid Convergence Index

Table 4.4 shows the results produced by the GCI calculation.

For each refinement of the grid, for instance from Grid1 to Grid2 (second row of the table), the refinement ratio (RR) is shown. The latter is the ratio between the grid of the actual iteration with the grid of the previous one, for instance Grid1 and Grid2. Rightmost table shows the GCI calculated with respect to each aerodynamic coefficient ( $C_L, C_D$  and  $C_M$  in order). One should recall that the smaller this value, the more unnecessary to keep refining the grid. As commented earlier, high values of GCI (and therefore great variations of all coefficients) for the first iterations, and lower values for the final ones can be observed. One can also note

that the GCI relative to the  $C_D$  is the lowest and reaches its minimum going from Grid6 to Grid7. The second best GCI is relative to  $C_L$  while the worst is relative to  $C_M$ . Interestingly, from Grid8 to Grid9 all GCIs rise.

Table 4.2 shows the results of the calculation of aerodynamic coefficients asymptotic values as well as the convergence order of the spatial discretization, based on aerodynamic coefficient trends. We recall that the numerical discretization method used in elsA has a theoretical order of 2.

This value is well approximated by the result relative to  $C_D$ .  $C_L$  order of convergence, however, has a much lower value. Concerning  $C_M$ , a negative order has been obtained, which makes no numerical sense. In fact it means that the solution gets worse as the grid is refined.

The estimated asymptotic value for  $C_D$  is very close to the values found from grid 4 onwards. The value of  $C_L$  is 0.5% higher than that for grid 12 while the value for  $C_M$  is 8% lower. This value of  $C_M$  is also meaningless.

	$C_L$	$C_D$	$C_M$
Asymptotic Value	0.840	125.1	-0.1894
Order of Convergence	0.57	2.15	-0.25

Table 4.2: Asymptotic value and order of convergence of each aerodynamic coefficient

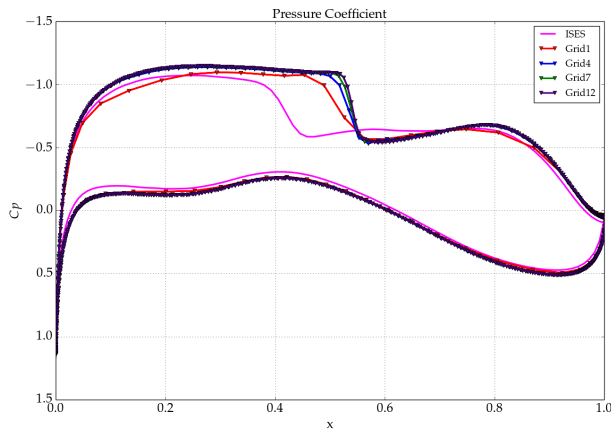
### 4.2.5 Field Drag Analysis

Table 4.5 shows the results from the FFD analysis. The leftmost column presents the near-field drag coefficient  $C_{D_{nf}}$  and its components, the middle column shows the  $C_{D_{ffd}}$  derived from the FFD method and its components, while the rightmost column presents the difference between those two, i.e. the spurious  $C_{D_{sp}}$ .

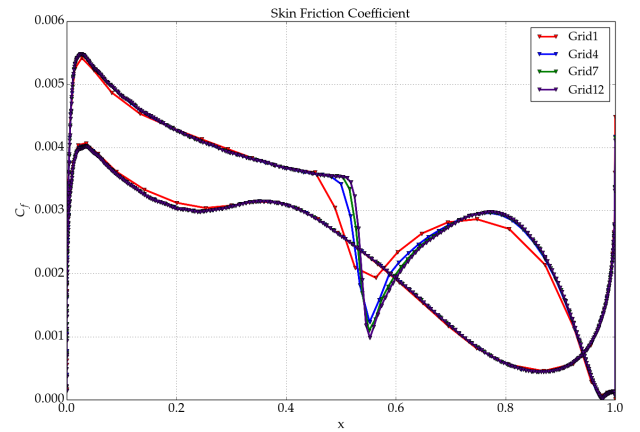
It is worth noting how the contribution of each component of  $C_{D_{ffd}}$  varies with the grid size.  $C_{D_{vp}}$  is strongly variable in the first 3 iterations but then stabilises in the remaining ones. This term strongly depends on the pressure field, thus if  $C_p$  does not change this term does not vary as well.  $C_{D_w}$  has an ascendant trend, i.e. the shock became stronger, except for Grid8 to Grid9 where it presents the same value. Finally it is quite interesting to note that the contribution of the friction is constant even from the first iteration. This is another proof of the robustness of the SA model with respect to grid refinement. About  $C_{D_{sp}}$  evolution with the grid size, one can make similar remarks to those made previously on the trend of the total  $C_D$ . There is a large variation in the first iterations, with these variations gradually decreasing, and then reaching a value below unity already at iteration 5. Finally, it can be seen that the values for grids 9, 11 and 12 do not make any sense, since the  $C_{D_{sp}}$  should not be negative according to what has been introduced about FFD analysis. However, these values obtained are within the uncertainty range of this approach.

### 4.2.6 Conclusion

Grid7 has been chosen to perform the simulations for the database mapping and the data assimilation, described in the following sections. In fact,  $C_p$  and  $C_f$  distribution calculated on it are almost indistinguishable to those of Grid12. The node distribution in the J direction, i.e. perpendicular to the airfoil wall, is dense enough to sufficiently cover the velocity profile at low  $y^+$ . All aerodynamic coefficients present a difference from the value obtained with the finest grid below 0.5%. The GCI relative to the aero coefficients going from Grid 6 to 7 is the lowest for  $GCI_{C_D}$  and among the lowest for the others. And finally, the  $C_{D_{sp}}$  relative to this grid is less than unity.



(a)  $C_p$  distribution



(b)  $C_f$  distribution

Figure 4.8: Pressure coefficient and skin friction distribution along "Porfil\_12" for various grids

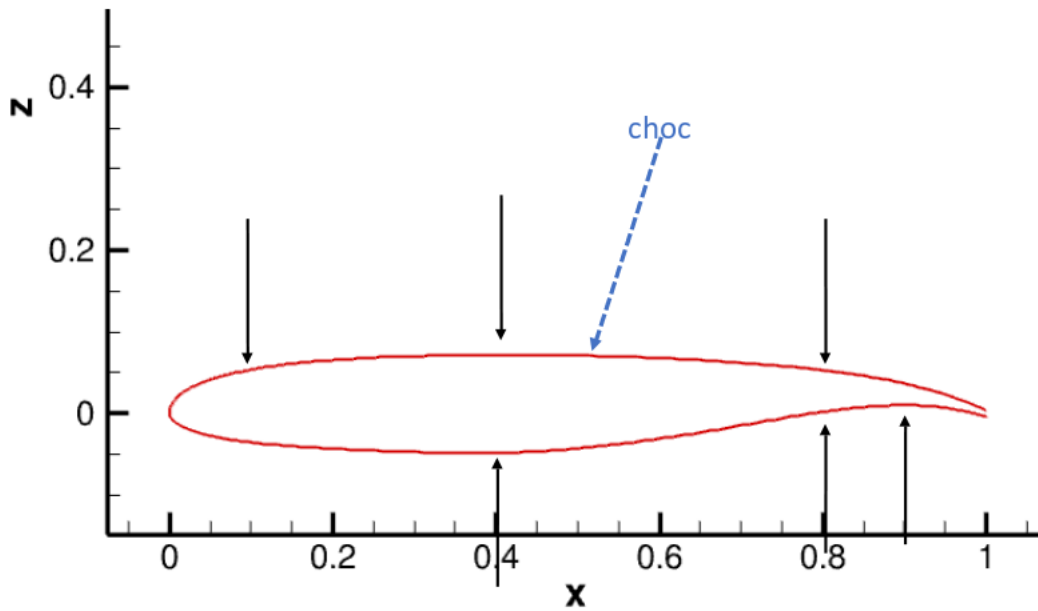
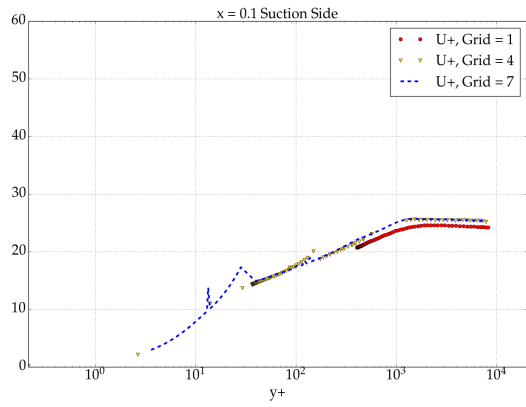
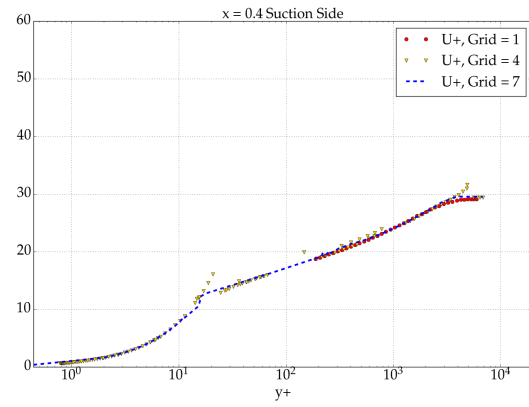


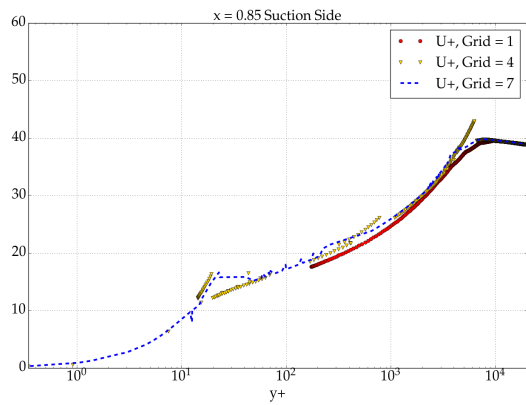
Figure 4.9: Illustration of the positions where velocity profile has been extracted on "Porfil\_12"



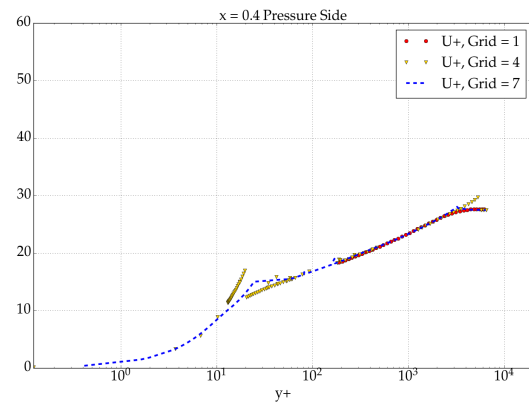
(a)  $x = 0.1$  on the SS



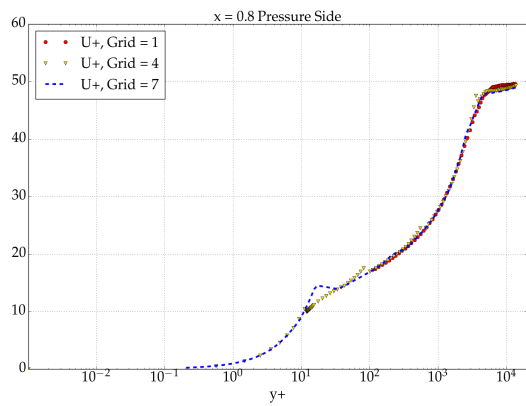
(b)  $x = 0.4$  on the SS



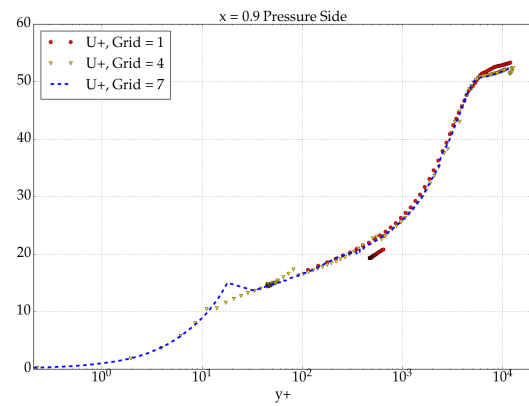
(c)  $x = 0.85$  on the SS



(d)  $x = 0.4$  on the PS



(e)  $x = 0.8$  on the PS



(f)  $x = 0.9$  on the PS

Figure 4.10: Non dimensional velocity  $U^+(y^+)$  extracted from elsA simulations in various grids

Name	Mesh Points	$C_L$	$C_D \cdot 10^{-4}$	$C_M$
Grid1	12749	0.775	154.5	-0.1971
Grid2	28700	0.799	130.3	-0.1989
Grid3	51392	0.814	126.0	-0.2010
Grid4	82456	0.822	125.1	-0.2024
Grid5	118994	0.826	124.9	-0.2031
Grid6	160692	0.829	124.9	-0.2037
Grid7	210540	0.831	124.9	-0.2040
Grid8	263414	0.832	124.8	-0.2041
Grid9	323920	0.833	124.9	-0.2043
Grid10	390674	0.833	124.9	-0.2045
Grid11	464442	0.834	124.9	-0.2046
Grid12	587536	0.835	125.0	-0.2048

Table 4.3: Aerodynamic coefficients per grid type

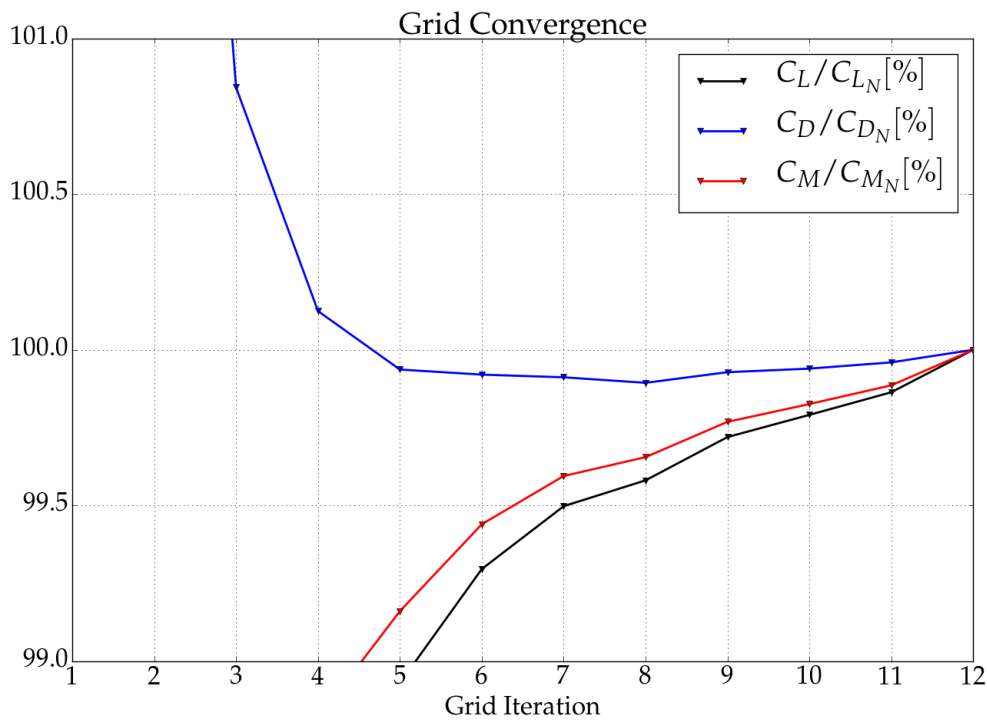


Figure 4.11: Normalised aerodynamic coefficients per each grid

<b>From</b>	<b>To</b>	<b>RR</b>	$GCI_{C_L}(\%)$	$GCI_{C_D}(\%)$	$GCI_{C_M}(\%)$
1	2	0.44	10.44	23.75	4.90
2	3	0.56	8.36	5.68	8.55
3	4	0.62	5.41	1.39	6.72
4	5	0.69	3.31	0.43	4.50
5	6	0.74	2.93	0.04	4.47
6	7	0.76	1.79	0.02	2.76
7	8	0.80	0.87	0.06	1.31
8	9	0.81	1.58	0.12	2.65
9	10	0.83	0.87	0.04	1.48
10	11	0.84	0.98	0.08	1.69

Table 4.4: Grid Convergence Index calculated per each aerodynamic coefficient

Name	$C_{D_{n.f}} =$	$C_{D_p} +$	$C_{D_f}$	$C_{D_{ff}} =$	$C_{D_{vp}} +$	$C_{D_w} +$	$C_{D_f}$	$C_{D_{sp(rev)}}$	$C_{D_{sp(irr)}}$
Grid1	154.5	100.9	53.6	127.7	60.0	14.1	53.6	25.724	1.014
Grid2	130.2	76.7	53.6	120.9	53.2	14.1	53.6	8.543	0.832
Grid3	126.0	72.4	53.6	121.9	52.7	15.6	53.6	3.412	0.737
Grid4	125.1	71.5	53.6	122.7	52.5	16.6	53.6	1.663	0.712
Grid5	124.9	71.2	53.6	123.5	52.5	17.4	53.6	0.661	0.692
Grid6	124.9	71.2	53.7	123.8	52.3	17.8	53.7	0.431	0.684
Grid7	124.9	71.2	53.7	124.0	52.2	18.1	53.7	0.180	0.676
Grid8	124.8	71.2	53.7	124.0	52.2	18.1	53.7	0.125	0.674
Grid9	124.9	71.2	53.7	124.2	52.1	18.4	53.7	-0.042	0.672
Grid10	124.9	71.2	53.7	124.2	52.1	18.5	53.7	0.005	0.670
Grid11	124.9	71.2	53.7	124.3	52.0	18.6	53.7	-0.024	0.669
Grid12	125.0	71.3	53.7	124.5	51.9	18.9	53.7	-0.181	0.678

Table 4.5: Far-Field Drag analysis per each grid

## 4.3 Reliability mapping of "pETW" database

This section presents the results obtained of the reliability mapping of numerical simulation with respect to experimental data, through the procedure described in *Section 4.3*. Firstly the aerodynamic conditions utilised to perform the simulations will be shown. Secondly, the results will be presented through the discrepancy metric  $\sigma$ , a variable capable of measure the discrepancy between numerical and experimental results, and thorough visualisation of some flow field properties (the pressure and skin friction distribution and the kinematic shape factor). All the elsA numerical simulations have been performed with the Grid7 from the Grid Convergence exercise.

### 4.3.1 Choice of $AoA$

Thanks to the procedure described in 3.4.2.2, table 4.6 has been obtained. In the latter, airfoil names with a star (\*) indicates lacking experimental data, hence only numerical simulations are accessible, violet cells signifies that ISES has diverged for that combination of  $(Re, M_a, AoA)$  and red cells that elsA has diverged.

It can be noticed that ISES has shown to be more robust, especially for Profil\_12. All things considered, it is somehow logical that this airfoil designed in a such rudimentary manner has a smooth performance range more limited than others which have been optimized and designed more thoroughly for transonic conditions. In fact, with the numerical set-up utilised, divergence has appeared mainly for BL separation and therefore unsteady aerodynamic phenomena did not fit a steady numeric scheme; evidently, Profil\_12 has a smaller drag curve working range compared to the other airfoils.

### 4.3.2 Comparison between experimental and numerical data

Tables 4.7, 4.8 and 4.9 show the main results of this exercise. The cell values represent  $\sigma$ , which has to some extent a similar definition as a statistical root mean square (RMS) or an euclidean norm, hence the smaller the value, the smaller the "distance" between the two pressure coefficient distributions (i. e. the little the difference between them). For each set (profile,  $M_a$ ,  $Re$ ) corresponds several  $\sigma$  values (one for each  $AoA$ , up to 5). Their location on the table correspond to the precise location of  $AoA$  in tab 4.6.

There are 3 pressure coefficient distribution comparisons presented in the tables: between ISES and elsA calculations, ISES and experimental data and ultimately between elsA and experimental data. Clearly, the contrast between numerical and experimental data has been only possible when the latter were available, thus for non-starred airfoils in the table 4.6.

Moreover,  $\sigma$  has been calculated for 3 different cases: utilising coefficient pressure distribution only from the airfoil lower surface, only from the airfoil upper surface and from both surfaces. Thus, it appears easier to comprehend where the contrast between data is located as well as his weight.

Conclusively, heating maps have been superimposed on table cells: green cells represent low values of  $\sigma$ , red cells high ones and white cells intermediate ones.

In table 4.7,  $\sigma$  has been computed *separately* on lower and upper surfaces between numerical simulations and experimental pressure coefficient distribution for airfoils RAE2822, EFT and "C2". In table 4.8, the complete  $C_p$  distribution (i. e. pressure side and suction side) has taken into account for  $\sigma$  calculation. For both of these tables,  $\sigma$  derived from ISES and experimental pressure coefficient distributions are on their left side, from elsA and experimental ones on their right side.

In table 4.9,  $\sigma$  calculated between elsA and ISES  $C_p$  vectors for airfoils RAE2822, EFT, C2 and Profil\_12 have been reported. In this case,  $\sigma$  has been shown both *separately* and *jointly* on pressure side (**PS**) and suction side (**SS**).

Concerning table 4.7, it can be noticed that  $C_p$  distributions of numerical simulations are much accurate on airfoil PS than on SS, for both elsA and ISES. In fact, we can notice that  $\sigma$  on the **lower surface** does not vary with  $AoA$ ,  $M_a$  and  $Re$  for RAE2822 as much as the others profiles. For EFT, ISES predictions on the PS are slightly worse than elsA ones. Lastly, elsA provides much higher  $\sigma$  values than ISES for C2 and they vary with  $M_a$  and  $AoA$ . In fact, elsA computations on C2 airfoil in transonic conditions have been surprisingly inaccurate on lower surface, up to 5 times bigger than on the other profiles. This exceptional behaviour may be related to the particular geometrical features of C2 airfoil as well as to more negative angles of attack chosen to perform C2 simulations. As a consequence of that, they have a more loaded PS than the other airfoils. In fact, it can be observed that, for negative  $AoA$ , the smaller the angles, the more important the  $\sigma$  value. Concluding about analyses on the PS, no  $Re$  coherent influences on  $\sigma$  can be noted on all three profiles.

The  $C_p$  predictive capabilities of both ISES and elsA on the **upper surface** tend to worsen with  $AoA$ , moving from left to right in the table, with Mach number, moving from the upper part of a sub-table to the lower (i.e.

keeping the airfoil constant), and with airfoil aft-camber, comparing the sub-tables each-other (top to bottom). In fact, whilst these capabilities between ISES and elsA are comparable for airflow simulations on RAE2822, the gap between them slightly increases for EFT and then much more for C2. In fact, we can notice that C2 prediction are **always** red coloured for Mach numbers bigger than 0.7. Reynolds number does not seem to change  $C_p$  prediction capabilities coherently, neither for elsA nor for ISES. Likewise, in table 4.8 we can observe the combined effects of lower and upper surface just briefly highlighted. Indeed, ISES has shown to be more accurate than elsA in most of the cases.

A similar trend may be noted in table 4.9: since ISES predictions are closer to experimental pressure field than elsA ones, a similar heatmap to the previous ones can be observed. Better correlation between ISES and elsA for less cambered airfoils, smaller angles of attack, and/or subsonic external flow conditions, worse correlation viceversa. However,  $Re$  number effects are easier to notice since the added (starred) points in table 3.4 furnish a wider distribution of aerodynamic conditions. These effects are more evident for C2 and Profil\_12, hence for the most aft-cambered airfoils. Firstly, the smaller the  $Re$ , the more difficult to converge for elsA. For instance, Profil\_12 has converged for 3 different  $AoAs$  at  $Re = 15.7m$  and  $M_a = 0.75$ , while only once at  $Re = 3.57m$  and the same  $M_a$ . Secondly, the bigger the  $Re$ , the smaller the discrepancy between elsA and ISES, although the difference is slight.

In figures 4.12 and 4.13 are reported the pressure distributions, picked from the "pETW" database (black triangles) and obtained from ISES (magenta line) and elsA (blue line) simulations, corresponding to the smallest and the biggest  $\sigma$  for all the airfoils. For the first six figures,  $\sigma$  computed between experimental and elsA  $C_p$  has been considered, whilst for Profil\_12  $\sigma$  between ISES and elsA. All aerodynamic conditions has been added in plot titles whilst  $\sigma$  values in figure descriptions. In addition,  $\sigma$  computed between ISES and experimental results and between elsA and experimental results have been added in the description of the first six figure (RAE2822, EFT and C2), in order to facilitate the comparison between them. Similarly, in figures 4.14 and 4.15 the skin friction coefficient distributions  $C_f$ , related to the biggest and smallest value of  $\sigma$ , of all profiles are shown as well as the kinematic shape factor  $H_k$  in figures 4.16 and 4.17.

The RAE and EFT profiles, in high-subsonic conditions ( $M_a = 0.5$ ), are well predicted by elsA and ISES with respect to the experimental data, obtaining  $\sigma$  values between 0.02 and 0.04 for both airfoils. We notice that the sigma value, both for ISES and elsA, is slightly higher for EFT (fig. 4.12c) than for RAE (fig. 4.12a). In transonic conditions the differences between the 3 curves (experimental, ISES and elsA results) is much tangible. The RAE profile (fig. 4.12b) is slightly better predicted by ISES, since the  $C_p$  is closer to the experimental data on  $PS$  and with a slightly more upstream shock. In agreement with this, the  $\sigma$  value of ISES (with respect to the experimental data) is slightly lower than that of elsA, 0.14 and 0.17 respectively. In EFT (fig. 4.12d) these two discrepancies (position of the shock and distribution of  $C_p$  on the  $PS$ ) in the transonic conditions shown are even more pronounced. The shock is more downstream in both elsA and ISES results, with the latter predicting it slightly better, as it was for RAE2822 airfoil. The  $\sigma$  of ISES is lower than that of elsA, 0.16 and 0.21, consistently with what is expected. Furthermore,  $\sigma$  values have risen between RAE2822 and EFT, both in transonic and high subsonic conditions, again being consistent with the trend of the curves. We note, also, that under subsonic conditions, elsA overestimates for both profiles the absolute value of the  $C_{p_{min}}$  (pressure coefficient minimum) compared to the experimental and ISES data. Under transonic conditions, the plateau upstream of the shock is also overestimated by elsA with respect to ISES and experimental data.

The best case of C2 airfoil (for  $\sigma$  calculated between elsA and experimental results) is in high subsonic conditions with negative  $\alpha$ , shown in fig. 4.13a. Despite being the best case,  $\sigma$  is quite high,  $\sigma = 0.08$ , compared to those mentioned for the RAE and EFT profiles. This is due to the fact that elsA overestimates the whole pressure field and since  $\sigma$  takes into account all points in the distribution of  $C_p$  in the estimation of the discrepancy, the latter is well indicated by this value.

It is recalled that a similar behaviour of elsA with respect to ISES, i.e. overestimating the pressure field in absolute value, was already found in the Profil\_12 design. ISES therefore has very satisfactory results with respect to the experimental data, as  $\sigma = 0.03$  suggests.

The worst case of C2 is quite illustrative, fig. 4.13b. The distance between the shock from the experimental data and the calculated shock from elsA is significantly important, while ISES has a better prediction (although not acceptable) of the shock position. Furthermore, upstream of the shock,  $C_p$  plateau is, in absolute value, higher than the experimental data and ISES.

The  $\sigma$  values are 0.26 and 0.16 for elsA and ISES, respectively. It can be observed qualitatively on the figure, that the discrepancy on  $PS$  is increased compared to EFT. The same thing can be observed from the trend of sigma calculated on the  $PS$  and showed in table 4.7, as commented above.

Lastly, the best case of Profil\_12 is in fully subsonic conditions, fig. 4.13c. It is interesting to note that the

disagreement between elsA and ISES in predicting  $C_p$  distribution on the PS is represented also at such low Mach number, although is quite small. In fact, the  $\sigma$  between elsA and ISES results is 0.03. Similar considerations made for profile C2 can be made for the worst case of Profil12, fig. 4.13d. High difference in shock position and PS  $C_p$  distribution. The difference in PS is even more tangible than in the previous cases. The  $\sigma$  in this case is equal to 0.21.

One can note from these figures a certain pattern: increasing the profile aft-camber, in general increases the discrepancy related to the position of the shock, the pressure distribution on the PS and the absolute value of the  $C_{p_{min}}$ .

Concerning RAE2822 airfoil, ISES overestimates, with respect to elsA, the  $C_f$  distribution under high subsonic conditions close to the leading edge, mainly on the SS and less on the PS, and then in an almost imperceptible manner in the rest of the profile. This is shown in fig. 4.14a.

In transonic conditions (fig. 4.14b), on the other hand, the overestimation of ISES on the SS rises compared to that in subsonic conditions, both upstream and downstream of the shock, while on PS no tangible contrast is observable.

The differences between ISES and elsA discussed for RAE under subsonic conditions are repeated almost equally for all profiles. In transonic conditions instead, one can notice a relevant discrepancy between the two CFD codes in the  $C_f$  distribution downstream of the shock. In fact, the mismatch between the prediction of ISES and elsA in this zone increases from RAE to EFT and then again between the latter and C2. However, this contrast is manifested differently for Profil\_12.

The author claims that the behaviour of ISES in overestimating  $C_f$  near the leading edge is due to the turbulent transition model, which is activated in the first grid cells at the leading edge. Nonetheless, this supposition has not been verified.

The contrast in the airfoil SS, downstream of the shock, on the other hand, is proportional to the rear-loading and it is therefore plausible that they are related.

The kinematic shape factor  $H_k$  distribution relative to high subsonic conditions, calculated for RAE2822 (fig. 4.16a), presents a remarkable concordance between two simulation results. This concordance is also present under transonic conditions (fig. 4.16b).

The first discrepancies between ISES and elsA results occur for the EFT profile in high subsonic conditions (fig. 4.16c), where ISES overestimates  $H_k$  with respect to elsA on the PS close to the trailing edge. This contrast then increases slightly in transonic conditions (fig. 4.16d), while a good agreement is maintained elsewhere.

The same occurs for C2 in subsonic and transonic conditions (fig. 4.17a and 4.17b) and for Profil\_12 in transonic conditions (4.17d). For Profil\_12 in **low** subsonic conditions this difference is quite small.

The discrepancy between elsA and ISES of this integral characteristics of the boundary layer also rises proportionally with the airfoil aft-camber and Mach number.

### 4.3.3 Conclusion

The main objective of this exercise was to analyse in the most complete and rigorous manner the capabilities of elsA and ISES in predicting the flow field around supercritical profiles. For accomplishing this, an important resource as the pETW database has been partially reproduced. To carry out this analysis, the reproduced aerodynamic conditions were chosen to have a wide range of Mach and Reynolds numbers and angles of attack. As a result of this exercise we can make the following considerations.

The CFD codes used, ISES and elsA, are sufficiently reliable in predicting the performance of supercritical profiles with moderate aft-camber. The main characteristics of the flow field, i.e. the pressure field and the viscous stress distribution, and one of the boundary layer ( $H_k$ ) presented consistent results. This is no longer the case when it comes to profiles with a very large rear loading. The elsA code struggled, more than ISES, in predicting the flow field correctly for most of the transonic aerodynamic conditions studied. Firstly these difficulties increases proportionally with the rear loading, secondly, with shock strength, thus with increasing Mach number and angle of attack.

The Reynolds number, on the other hand, had little effects on the discrepancy between the CFD solvers. Mainly, it affected the convergence of the numerical solution of some airfoils.

A certain pattern was noticed by comparing flow field and boundary layer quantities. The contrast between the pETW, ISES and elsA data grows in proportion to the rear-loading in the following manners: shock position and  $C_p$  distribution on the PS,  $C_f$  evolution downstream of the shock,  $H_k$  trend at the PS trailing edge. Hence, a correlation between these phenomena and the rear-loading has shown to be more than plausible.

Profil\_12 has shown to be able to reproduce the same mismatch of the most aft-cambered airfoils, such as EFT and C2. Hence, it can be used for further investigations without the constraint of confidentiality.

Whereas these discrepancies had been observed and analysed previously, such a complete mapping of this issue

has been performed for the first time.

A wide range of aerodynamic conditions has been covered and analysed with a method created ad hoc (discrepancy metric  $\sigma$ ), which is quite intuitive and achieved consistent results.

The results here presented will be used also during the data assimilation, since some aerodynamic conditions will be chosen in relation with their discrepancy metric value.

Conclusively, it should be noted that ISES has been more accurate than elsA. A solver of the Euler equations coupled with a correlation-based boundary layer resolution model, which solves airfoil flow field in a matter of seconds, has proven to be more robust than a RANS solving method associated with the SA model.

Airfoil	$Re$ m	$Ma$	$\alpha$ [°]				
RAE	3.57	0.246	2.65	4.32	6.02	7.73	9.54
RAE*	9.00	0.250	1.00	2.00	3.01	4.00	5.01
RAE	11.84	0.498	-1.74	0.74	2.19	3.05	4.03
RAE	15.45	0.704	-1.51	-0.05	0.92	1.88	2.85
RAE	15.79	0.726	-1.98	-1.04	-0.05	0.91	1.86
RAE	15.74	0.748	-2.00	-1.04	-0.06	0.90	1.86
RAE	9.06	0.750	-2.00	-1.04	-0.06	0.90	1.86
RAE*	3.57	0.750	1.56	3.22	4.92	6.58	8.27
EFT	3.67	0.250	1.56	3.22	4.92	6.58	8.27
EFT*	9.01	0.250	1.14	2.38	3.62	4.45	5.27
EFT	11.72	0.500	1.14	2.38	3.62	4.45	5.27
EFT	15.47	0.705	1.10	1.99	2.49	3.05	3.75
EFT	15.50	0.727	-1.65	-0.71	0.16	1.09	2.07
EFT	15.55	0.747	-1.93	-1.02	0.03	0.98	1.81
EFT	8.94	0.747	-1.93	-1.02	0.02	0.98	1.81
EFT*	3.57	0.750	-1.93	-1.02	0.02	0.98	1.81
C2*	3.57	0.250	0.00	1.00	2.00	3.00	4.00
C2*	9.00	0.250	-1.89	0.08	1.31	2.15	4.24
C2	11.83	0.505	-3.08	-2.00	-0.98	2.14842	4.24148
C2	15.79	0.705	0.09	1.02	1.59	2.22	
C2	15.79	0.705	-3.24	-1.87	-0.55	0.68	1.65
C2	15.71	0.724	-1.99	-1.10	-0.65	0.24	0.71
C2	15.67	0.749	-2.06	-1.05	-0.62	0.18	0.79
C2	9.01	0.745	-2.06	-1.05	-0.62	0.18	0.79
C2*	3.57	0.750	-2.06	-1.05	-0.62	0.18	0.79
Profil_12*	3.57	0.250	0.00	1.00	2.00	3.00	4.00
Profil_12*	9.00	0.250	-2.06	-1.05	-0.62	0.18	0.79
Profil_12*	11.83	0.505	-0.98	0.09	1.02	1.59	2.22
Profil_12*	15.79	0.705	-3.24	-1.87	-0.55	0.68	1.65
Profil_12*	15.71	0.724	-1.99	-1.10	-0.65	0.24	0.71
Profil_12*	15.67	0.749	-2.06	-1.05	-0.62	0.18	0.79
Profil_12*	9.01	0.750	-2.05619	-1.05315	-0.623574	0.182223	0.786771
Profil_12*	3.57	0.750	-2.05619	-1.05315	-0.623574	0.182223	0.786771

Table 4.6: Aerodynamics conditions simulated per airfoil; starred (\*) airfoils indicates lack of experimental data; violet cells indicate ISES divergence; red cells indicate elsA divergence.

Re	Ma	lower surface		upper surface		lower surface		upper surface											
		$\sigma$ : ISES		- EXP		$\sigma$ : EXP		- ELSA											
<b>RAE2822</b>																			
3.57	0.25	0.04	0.03	0.03	0.02	0.04	0.04	0.05	0.02	0.02	0.02	0.02	0.03	0.04	0.05	0.07	0.08	0.02	
11.8	0.50	0.02	0.02	0.01	0.01	0.01	0.02	0.02	0.03	0.03	0.11	0.02	0.02	0.02	0.02	0.03	0.04	0.14	
15.5	0.70	0.04	0.05	0.04	0.02	0.02	0.03	0.03	0.04	0.13	0.18	0.03	0.03	0.02	0.02	0.04	0.04	0.06	
15.8	0.73	0.04	0.02	0.02	0.01	0.02	0.02	0.03	0.04	0.07	0.19	0.03	0.02	0.01	0.02	0.04	0.05	0.06	
15.7	0.75	0.06	0.03	0.02	0.02	0.01	0.01	0.03	0.04	0.05	0.10	0.04	0.03	0.02	0.02	0.03	0.05	0.07	
9.06	0.75	0.07	0.03	0.02	0.02	0.01	0.01	0.03	0.04	0.05	0.09	0.05	0.02	0.02	0.01	0.01	0.02	0.05	
<b>EFT</b>																			
$\sigma$ : ISES										$\sigma$ : EXP									
$\sigma$ : ISES										$\sigma$ : EXP									
3.67	0.25	0.04	0.04	0.04	0.06	0.06	0.09	0.19	0.02	0.02	0.02	0.02	0.02	0.02	0.02	0.05	0.09	0.12	
11.7	0.50	0.04	0.04	0.04	0.04	0.03	0.03	0.03	0.05	0.02	0.02	0.02	0.02	0.02	0.02	0.05	0.05	0.05	
15.5	0.71	0.05	0.03	0.02	0.02	0.03	0.06	0.06	0.16	0.20	0.12	0.03	0.02	0.02	0.03	0.04	0.06	0.14	
15.5	0.73	0.05	0.05	0.06	0.04	0.02	0.03	0.04	0.04	0.05	0.21	0.03	0.03	0.03	0.03	0.06	0.07	0.07	
15.6	0.75	0.06	0.05	0.05	0.03	0.02	0.03	0.04	0.05	0.20	0.08	0.04	0.03	0.03	0.03	0.06	0.07	0.09	
8.94	0.75	0.06	0.05	0.05	0.03	0.02	0.02	0.03	0.04	0.19	0.10	0.04	0.03	0.03	0.03	0.05	0.06	0.08	
<b>C2</b>										$\sigma$ : ISES									
$\sigma$ : ISES										$\sigma$ : EXP									
$\sigma$ : ISES										$\sigma$ : EXP									
11.8	0.51	0.03	0.02	0.02	0.03	0.03	0.03	0.04	0.05	0.05	0.08	0.07	0.05	0.03	0.03	0.02	0.08	0.10	
15.8	0.71	0.23	0.07	0.05	0.02	0.02	0.04	0.02	0.02	0.04	0.05	0.17	0.15	0.05	0.07	0.12	0.12	0.08	
15.8	0.71	0.04	0.03	0.04	0.05	0.05	0.10	0.16	0.22	0.05	0.05	0.05	0.05	0.07	0.07	0.15	0.25	0.30	
15.7	0.72	0.06	0.05	0.03	0.05	0.03	0.03	0.05	0.19	0.16	0.20	0.20	0.17	0.06	0.07	0.06	0.13	0.14	
15.7	0.75	0.11	0.07	0.05	0.05	0.04	0.03	0.05	0.07	0.18	0.10	0.18	0.08	0.07	0.09	0.14	0.15	0.15	
9.01	0.75	0.10	0.08	0.07	0.04	0.05	0.03	0.04	0.05	0.16	0.09	0.15	0.10	0.08	0.07	0.09	0.12	0.15	

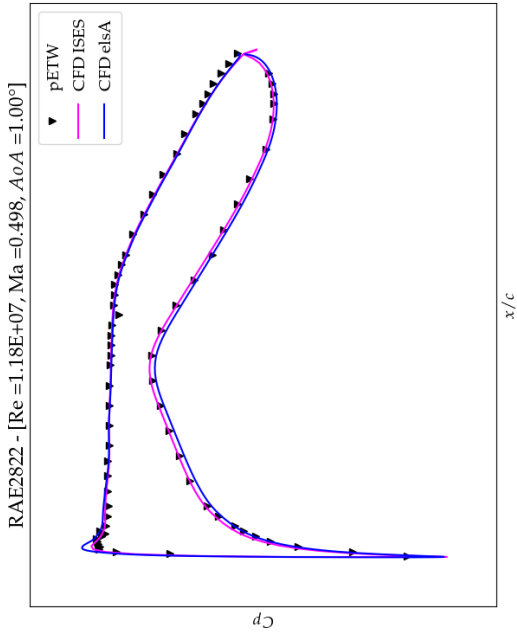
Table 4.7:  $\sigma$  values between numerical simulations and experimental data for airfoils RAE2822, EFT and C2, calculated *separately* in lower and upper surfaces.

<b>Re Ma</b>		<b>lower and upper surface</b>									
<b>RAE2822</b>		<b><math>\sigma</math> : ISES - EXP</b>					<b><math>\sigma</math> : EXP - ELSA</b>				
3.57	0.25	0.04	0.04	0.05	0.02		0.04	0.04	0.06	0.06	0.03
11.8	0.50	0.02	0.02	0.02	0.03	0.08	0.02	0.02	0.03	0.03	0.11
15.5	0.70	0.04	0.04	0.04	0.1	0.14	0.04	0.04	0.05	0.15	0.17
15.8	0.73	0.03	0.03	0.03	0.05	0.14	0.03	0.04	0.05	0.08	0.14
15.7	0.75	0.04	0.03	0.03	0.04	0.08	0.03	0.04	0.06	0.07	0.09
9.06	0.75	0.05	0.03	0.03	0.04	0.07	0.04	0.04	0.06	0.09	0.08
<b>EFT</b>		<b><math>\sigma</math> : ISES - EXP</b>					<b><math>\sigma</math> : EXP - ELSA</b>				
3.67	0.25	0.05	0.08	0.15			0.04	0.07	0.09	0.13	0.17
11.7	0.50	0.03	0.03	0.03	0.05		0.04	0.04	0.04	0.05	0.06
15.5	0.71	0.06	0.05	0.13	0.16	0.1	0.05	0.11	0.18	0.2	0.1
15.5	0.73	0.04	0.05	0.05	0.05	0.16	0.05	0.06	0.06	0.12	0.21
15.6	0.75	0.05	0.05	0.05	0.16	0.07	0.05	0.06	0.07	0.2	0.11
8.94	0.75	0.04	0.04	0.05	0.15	0.08	0.05	0.05	0.07	0.2	0.12
<b>C2</b>		<b><math>\sigma</math> : ISES - EXP</b>					<b><math>\sigma</math> : EXP - ELSA</b>				
11.8	0.51	0.03	0.04	0.04	0.05	0.07	0.08	0.09	0.09	0.1	0.07
15.8	0.71	0.14	0.05	0.05			0.12	0.13	0.1		
15.8	0.71	0.05	0.08	0.13	0.18		0.12	0.2	0.24	0.26	
15.7	0.72		0.04	0.05	0.16	0.13	0.13	0.15	0.12	0.26	0.19
15.7	0.75	0.07	0.06	0.06	0.15	0.08	0.15	0.13	0.13	0.2	
9.01	0.75	0.06	0.06	0.06	0.13	0.08	0.13	0.13	0.13	0.22	0.14

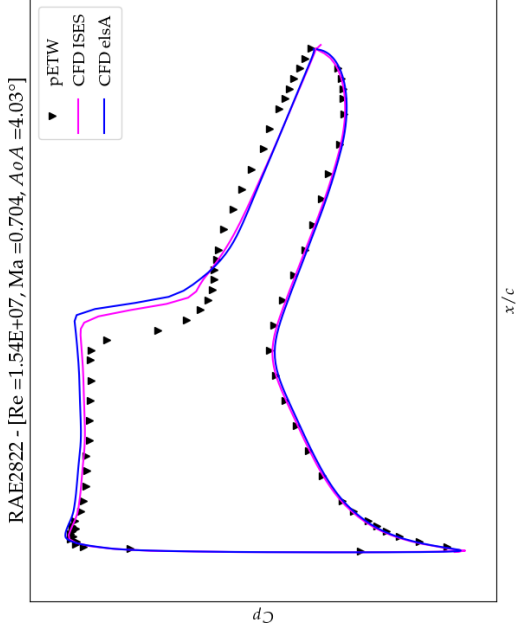
Table 4.8:  $\sigma$  values between numerical simulations and experimental data for airfoils RAE2822, EFT and C2, calculated *jointly* in lower and upper surfaces.

Re	Ma	lower surface					upper surface					lower and upper surface				
<b>RAE2822</b>		<b><math>\sigma</math> : ISES - ELSA</b>														
3.57	0.25	0.03	0.03	0.02	0.01		0.02	0.02	0.02	0.11		0.02	0.02	0.02	0.09	
9	0.25	0.03	0.02	0.02	0.01		0.02	0.02	0.02	0.12		0.02	0.02	0.02	0.10	
11.8	0.5	0.03	0.02	0.02	0.02	0.03	0.02	0.02	0.02	0.03	0.12	0.02	0.02	0.02	0.03	0.10
15.5	0.7	0.03	0.02	0.02	0.02	0.01	0.02	0.03	0.05	0.07	0.06	0.02	0.03	0.04	0.06	0.05
15.8	0.73	0.03	0.03	0.02	0.02	0.02	0.02	0.02	0.03	0.06	0.06	0.03	0.03	0.03	0.05	0.05
15.7	0.75	0.04	0.03	0.03	0.02	0.02	0.02	0.02	0.03	0.05	0.05	0.03	0.03	0.03	0.04	0.04
9.06	0.75	0.04	0.03	0.03	0.02	0.02	0.02	0.02	0.04	0.06	0.06	0.03	0.03	0.03	0.05	0.05
3.57	0.75	0.04	0.03	0.03	0.03	0.02	0.02	0.03	0.04	0.06	0.08	0.03	0.03	0.04	0.05	0.07
<b>EFT</b>		<b><math>\sigma</math> : ISES - ELSA</b>														
3.67	0.25	0.03	0.03	0.04			0.02	0.02	0.07			0.03	0.02	0.07		
9	0.25	0.03	0.03	0.02	0.02	0.01	0.02	0.02	0.02	0.03	0.18	0.02	0.02	0.02	0.03	0.14
11.7	0.5	0.03	0.03	0.02	0.02		0.02	0.03	0.03	0.04		0.03	0.03	0.03	0.03	
15.5	0.71	0.03	0.02	0.02	0.02	0.01	0.06	0.10	0.10	0.08	0.08	0.05	0.08	0.08	0.07	0.06
15.5	0.73	0.04	0.04	0.03	0.03	0.02	0.03	0.03	0.05	0.12	0.11	0.04	0.04	0.04	0.09	0.09
15.6	0.75	0.05	0.04	0.03	0.02	0.02	0.03	0.04	0.05	0.11	0.08	0.04	0.04	0.05	0.09	0.06
8.94	0.75	0.05	0.04	0.04	0.03	0.02	0.04	0.04	0.06	0.13	0.09	0.04	0.04	0.05	0.10	0.07
3.57	0.75	0.06	0.05	0.04	0.03		0.04	0.05	0.06	0.14		0.05	0.05	0.06	0.11	
<b>C2</b>		<b><math>\sigma</math> : ISES - ELSA</b>														
3.57	0.25	0.06	0.05	0.05	0.04		0.05	0.05	0.05	0.05		0.05	0.05	0.05	0.05	
9	0.25	0.06	0.05	0.04	0.04	0.04	0.05	0.05	0.05	0.04	0.04	0.05	0.05	0.05	0.04	0.04
11.8	0.51	0.07	0.05	0.05	0.04	0.03	0.05	0.06	0.06	0.07	0.11	0.06	0.06	0.06	0.06	0.09
15.8	0.71	0.19	0.16	0.08			0.08	0.11	0.08			0.13	0.13	0.08		
15.8	0.71	0.06	0.04	0.03	0.03		0.12	0.20	0.19	0.16		0.10	0.16	0.16	0.13	
15.7	0.72		0.18	0.07	0.04	0.03		0.11	0.11	0.23	0.12		0.14	0.10	0.18	0.10
15.7	0.75	0.22	0.12	0.09	0.05		0.13	0.13	0.14	0.15		0.17	0.13	0.13	0.13	
9.01	0.75	0.24	0.13	0.10	0.07	0.04	0.13	0.13	0.14	0.19	0.14	0.18	0.13	0.13	0.16	0.12
3.57	0.75	0.27	0.18				0.14	0.15				0.19	0.16			
<b>Profil_12</b>		<b><math>\sigma</math> : ISES - ELSA</b>														
3.57	0.25	0.05	0.04	0.04			0.03	0.03	0.03			0.04	0.04	0.03		
9	0.25	0.05	0.04	0.04	0.03	0.03	0.03	0.03	0.03	0.03	0.03	0.04	0.03	0.03	0.03	0.03
11.8	0.51	0.05	0.04	0.03	0.03	0.03	0.04	0.04	0.04	0.04	0.08	0.04	0.04	0.04	0.04	0.07
15.8	0.71	0.06	0.05	0.03			0.07	0.09	0.12			0.07	0.08	0.10		
15.7	0.72	0.09	0.08	0.07	0.03		0.06	0.07	0.09	0.14		0.08	0.08	0.09	0.11	
15.7	0.75	0.10	0.08	0.07			0.09	0.10	0.16			0.10	0.10	0.14		
9.01	0.75	0.11					0.09					0.10				
3.57	0.75	0.13					0.10					0.11				

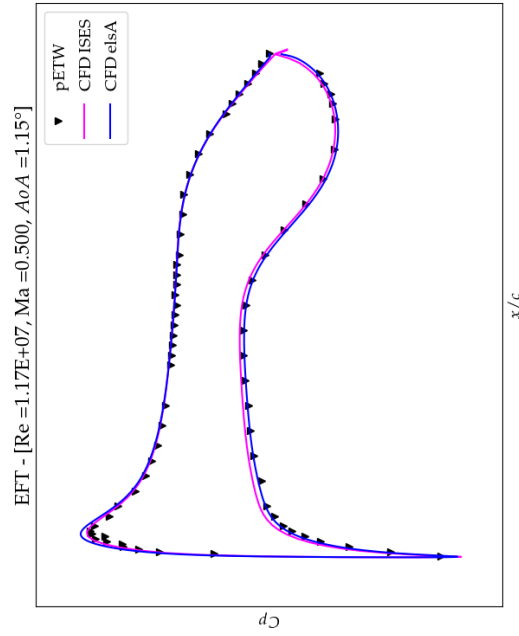
Table 4.9:  $\sigma$  values between elsA and ISES numerical simulations for airfoils RAE2822, EFT, C2 and Profil\_12 calculated *separately* in lower and upper surfaces, first 2 columns from left, and *jointly* in lower and upper surfaces, rightmost column .



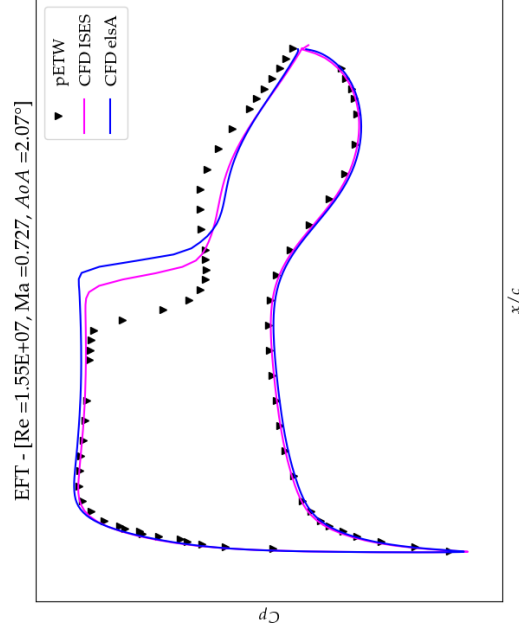
(a) smallest  $\sigma$  for RAE2822. ( $\sigma_{EXP-elsA} = 0.02, \sigma_{EXP-ISES} = 0.02$ )



(b) biggest  $\sigma$  for RAE2822. ( $\sigma_{EXP-elsA} = 0.17, \sigma_{EXP-ISES} = 0.14$ )

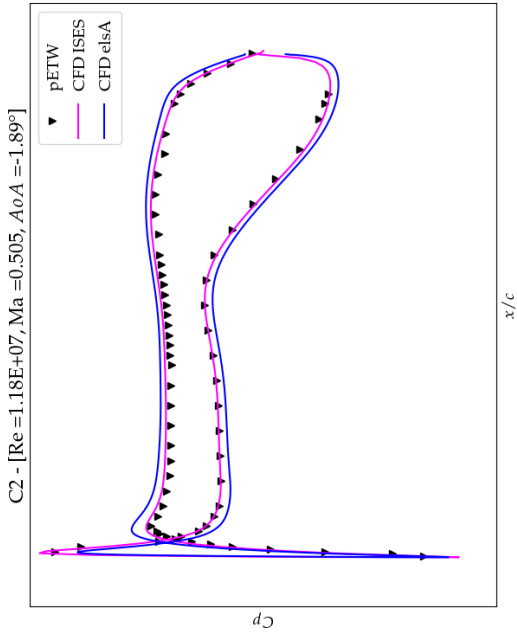


(c) smallest  $\sigma$  for EFT. ( $\sigma_{EXP-elsA} = 0.04, \sigma_{EXP-ISES} = 0.03$ )

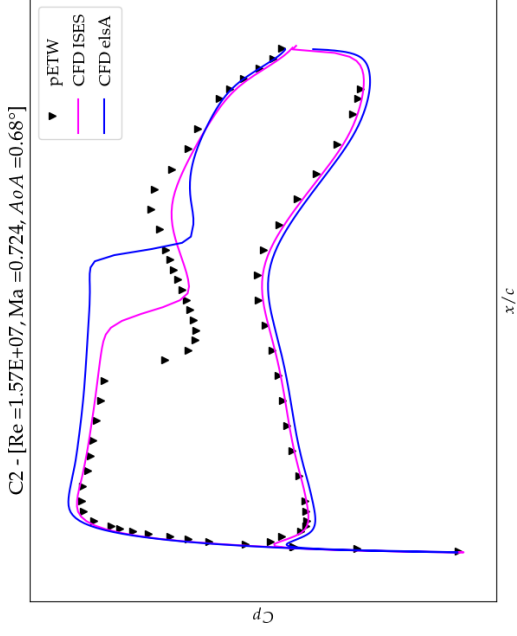


(d) biggest  $\sigma$  for EFT. ( $\sigma_{EXP-elsA} = 0.21, \sigma_{EXP-ISES} = 0.16$ )

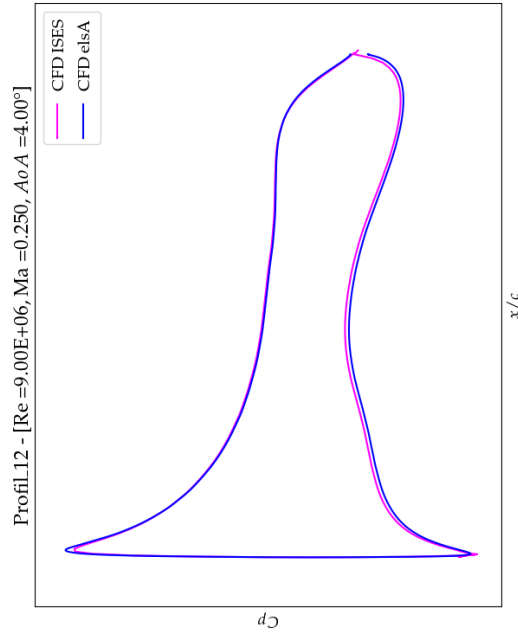
Figure 4.12: Pressure coefficient distribution for best and worst cases of RAE2822 and EFT airfoils



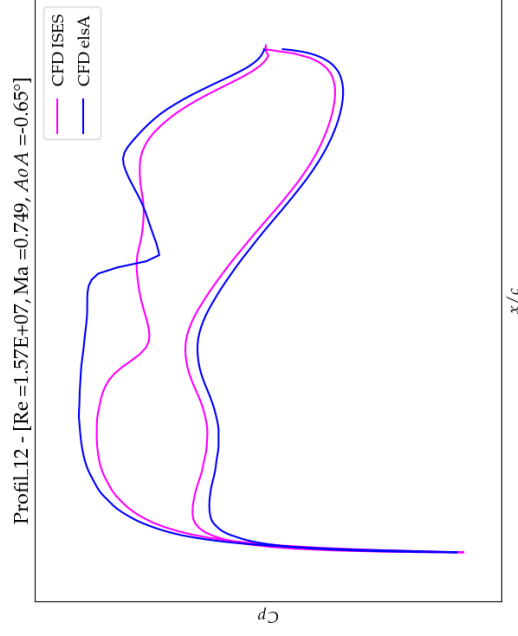
(a) smallest  $\sigma$  for C2. ( $\sigma_{EXP-elsA} = 0.08, \sigma_{EXP-ISES} = 0.03$ )



(b) biggest  $\sigma$  for C2. ( $\sigma_{EXP-elsA} = 0.26, \sigma_{EXP-ISES} = 0.16$ )

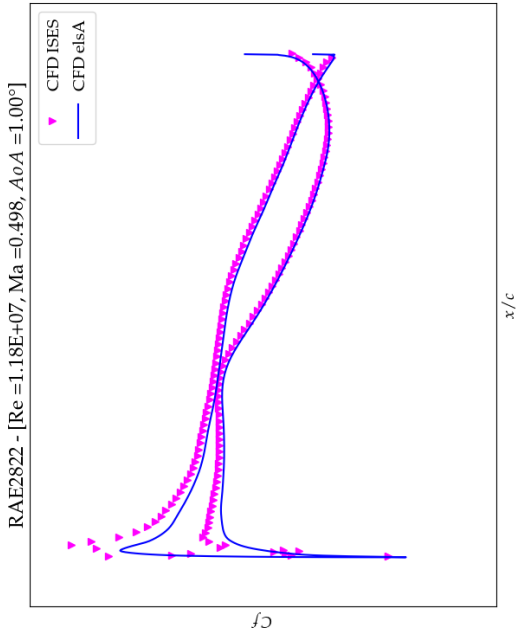


(c) smallest  $\sigma$  for Profil\_12.  $\sigma_{ISES-elsA} = 0.03$

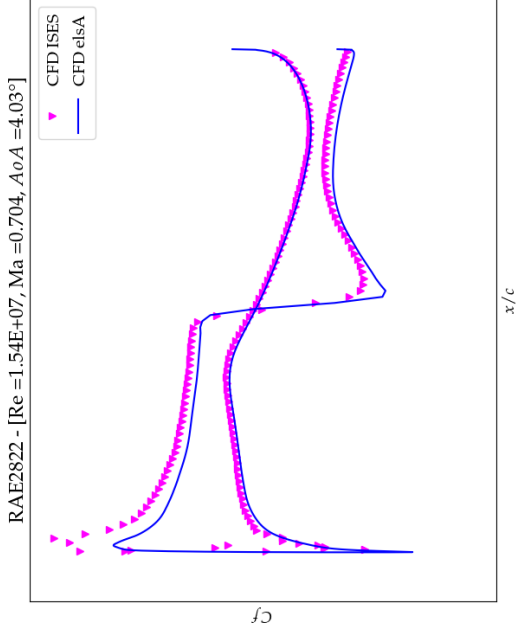


(d) biggest  $\sigma$  for Profil\_12.  $\sigma_{ISES-elsA} = 0.21$

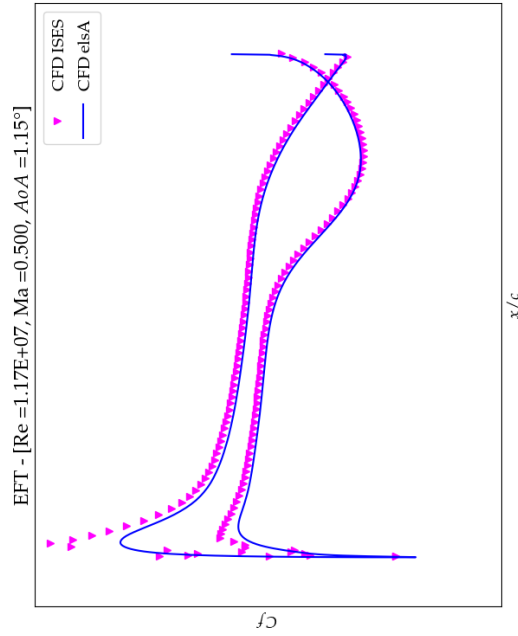
Figure 4.13: Pressure coefficient distribution for best and worst cases of C2 and Profil\_12 airfoils



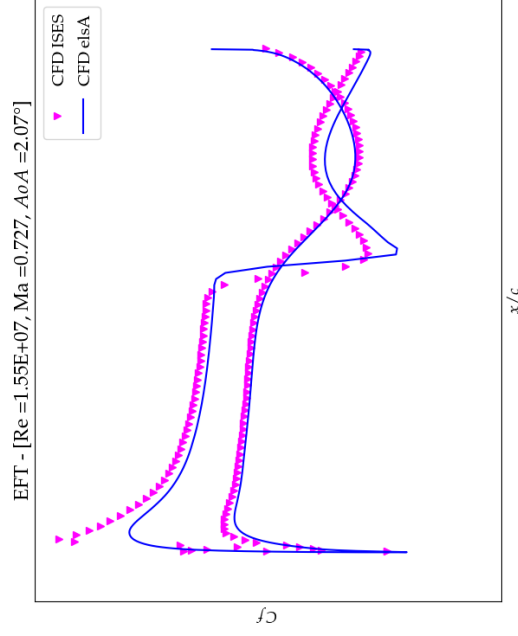
(a) smallest  $\sigma$  for RAE2822. ( $\sigma_{EXP-elsA} = 0.02, \sigma_{EXP-ISES} = 0.02$ )



(b) biggest  $\sigma$  for RAE2822. ( $\sigma_{EXP-elsA} = 0.17, \sigma_{EXP-ISES} = 0.14$ )

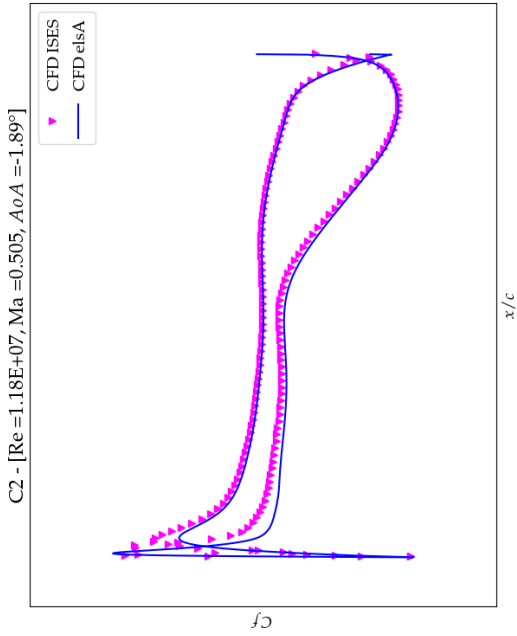


(c) smallest  $\sigma$  for EFT. ( $\sigma_{EXP-elsA} = 0.04, \sigma_{EXP-ISES} = 0.03$ )

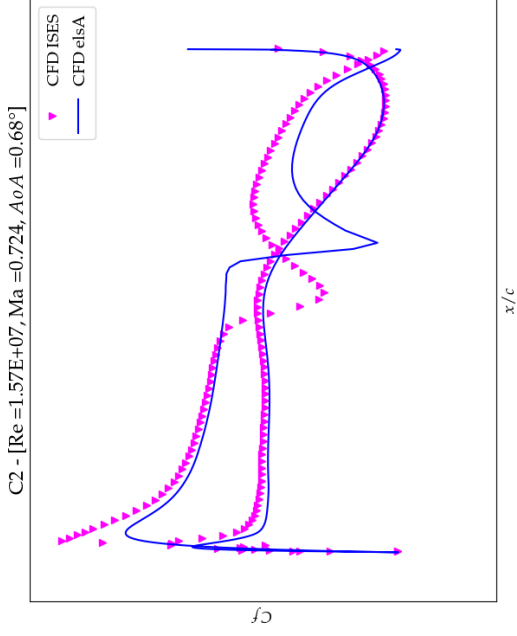


(d) biggest  $\sigma$  for EFT. ( $\sigma_{EXP-elsA} = 0.21, \sigma_{EXP-ISES} = 0.16$ )

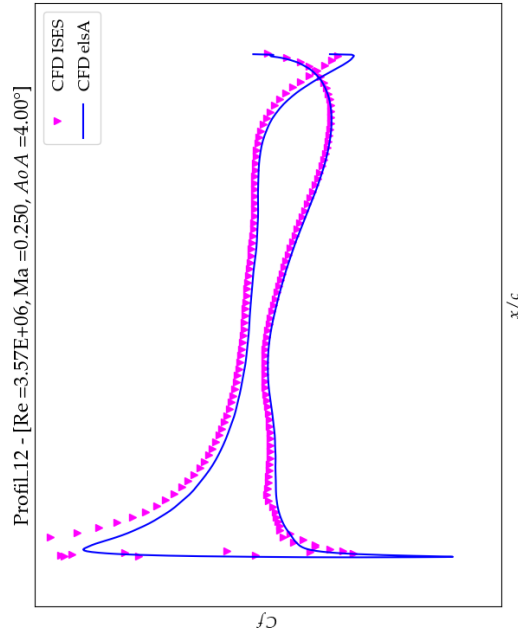
Figure 4.14: Skin friction coefficient distribution for best and worst cases for RAE2822 and EFT airfoils



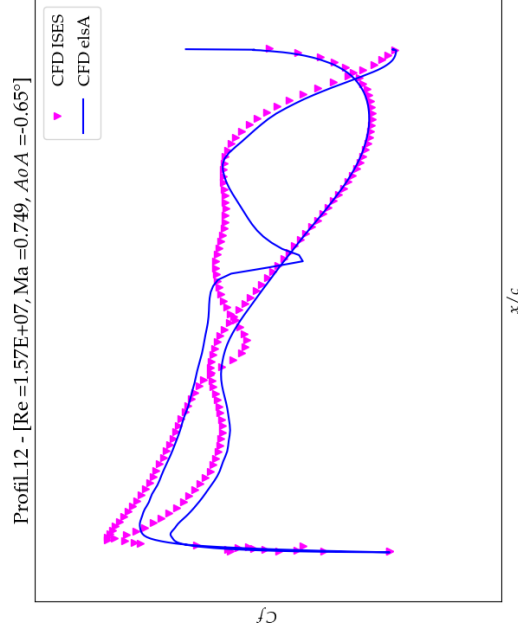
(a) smallest  $\sigma$  for C2. ( $\sigma_{EXP-elsA} = 0.08, \sigma_{EXP-ISES} = 0.03$ )



(b) biggest  $\sigma$  for C2. ( $\sigma_{EXP-elsA} = 0.26, \sigma_{EXP-ISES} = 0.16$ )

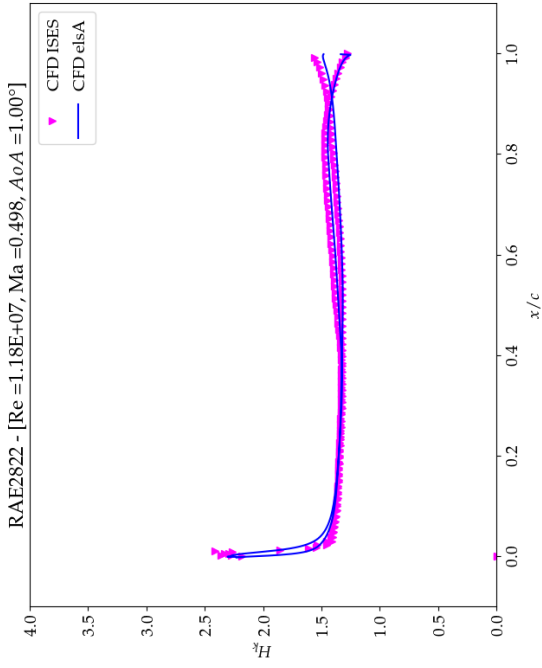


(c) smallest  $\sigma$  for Profil\_12.  $\sigma_{ISES-elsA} = 0.03$

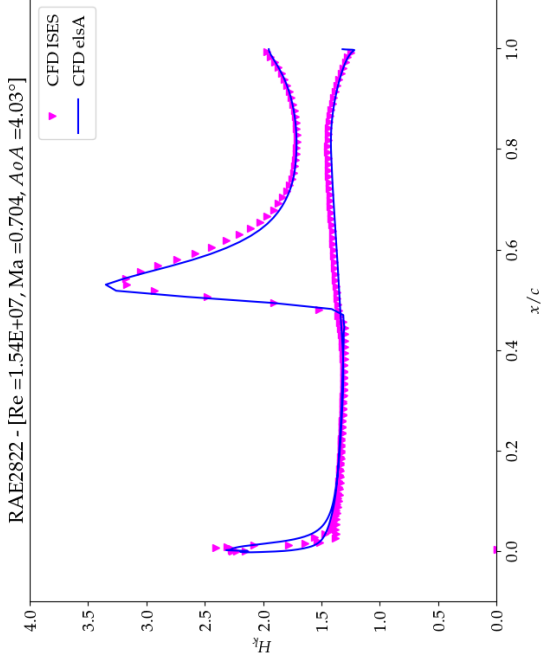


(d) biggest  $\sigma$  for Profil\_12.  $\sigma_{ISES-elsA} = 0.21$

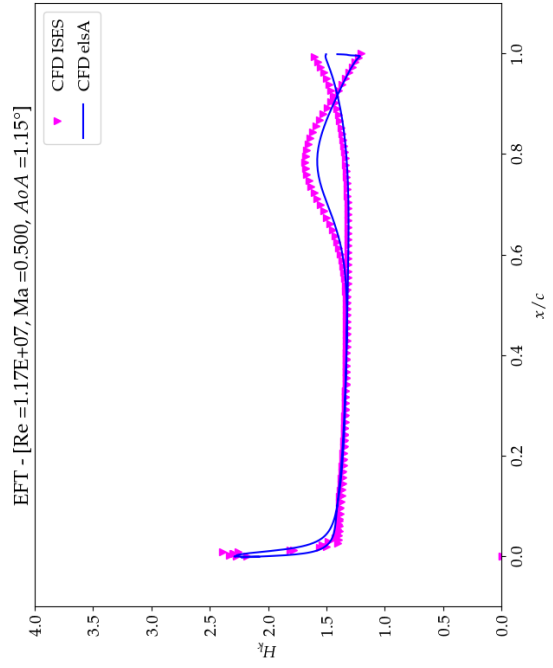
Figure 4.15: Skin friction coefficient distribution for best and worst cases for C2 and Profil\_12 airfoils



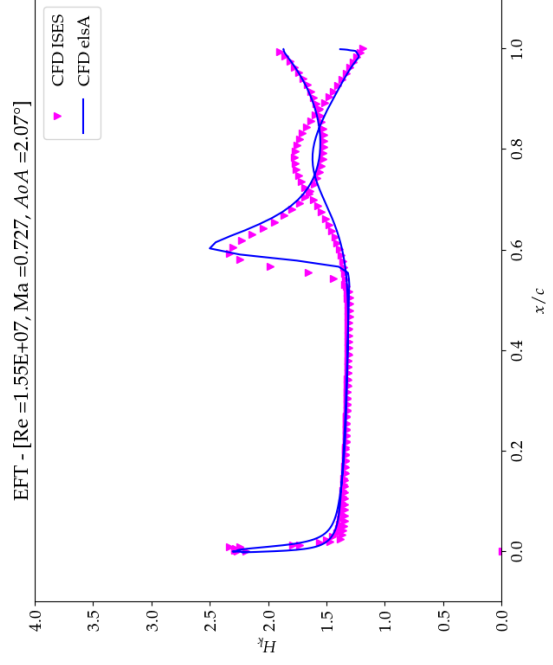
(a) smallest  $\sigma$  for RAE2822. ( $\sigma_{EXP-elsA} = 0.02, \sigma_{EXP-ISES} = 0.02$ )



(b) biggest  $\sigma$  for RAE2822. ( $\sigma_{EXP-elsA} = 0.17, \sigma_{EXP-ISES} = 0.14$ )

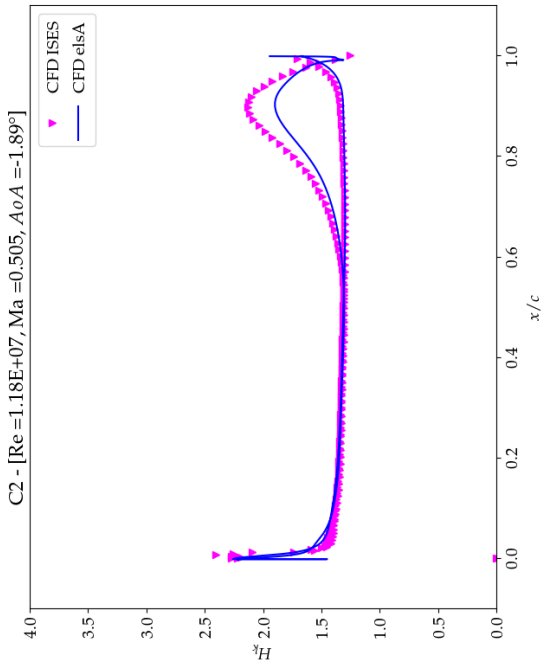


(c) smallest  $\sigma$  for EFT. ( $\sigma_{EXP-elsA} = 0.04, \sigma_{EXP-ISES} = 0.03$ )

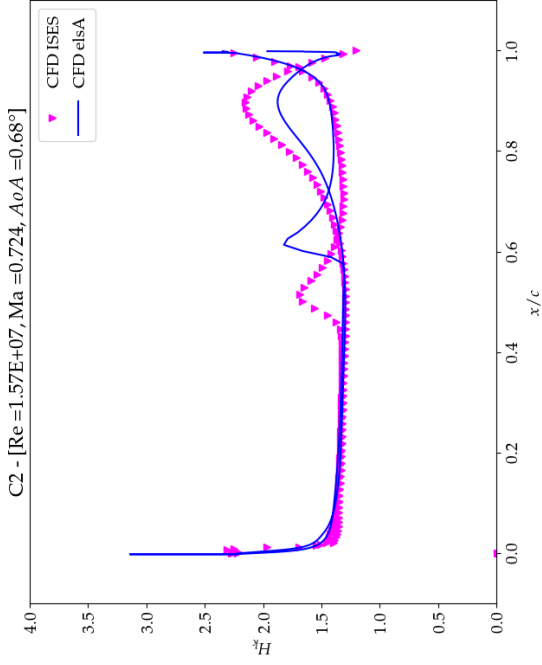


(d) biggest  $\sigma$  for EFT. ( $\sigma_{EXP-elsA} = 0.21, \sigma_{EXP-ISES} = 0.16$ )

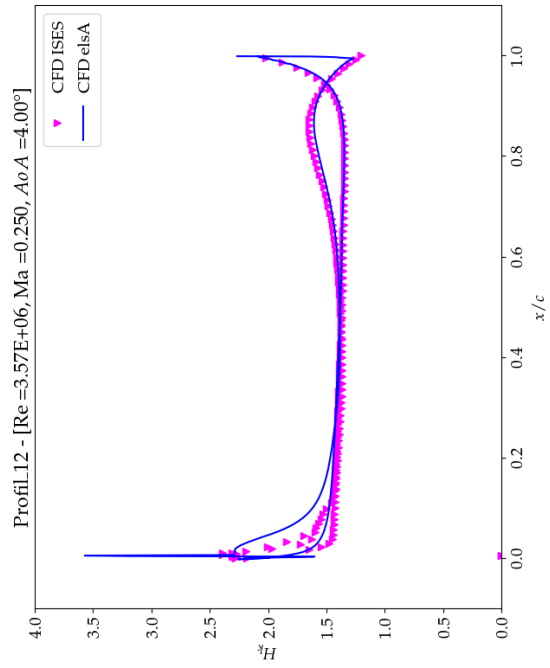
Figure 4.16: Kinematic shape factor distribution for best and worst cases for RAE2822 and EFT airfoils



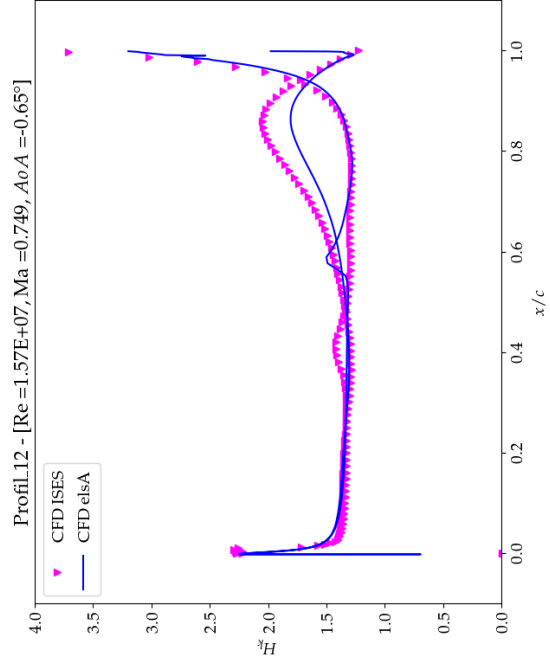
(a) smallest  $\sigma$  for C2. ( $\sigma_{EXP-elsA} = 0.08, \sigma_{EXP-ISES} = 0.03$ )



(b) biggest  $\sigma$  for C2. ( $\sigma_{EXP-elsA} = 0.26, \sigma_{EXP-ISES} = 0.16$ )



(c) smallest  $\sigma$  for Profil\_12.  $\sigma_{ISES-elsA} = 0.03$



(d) biggest  $\sigma$  for Profil\_12.  $\sigma_{ISES-elsA} = 0.21$

Figure 4.17: Kinematic shape factor distribution for best and worst cases for C2 and Profil\_12 airfoils

## 4.4 Data Assimilation

This section presents the results obtained by applying the procedure described in 3.5, and thus the four optimisation problems previously introduced. A brief summary of these problems is given here.

In the first problem, a variety of sets of "coefficients" (it seems inappropriate call them constants) of the Spalart-Allmaras (SA) model were tested, having as target the experimental  $C_p$  and  $C_f$  of ISES and as BIRDIE input those both computed with elsA.

In the second problem the parameters found previously have been assimilated for C2 and EFT airfoils in diverse aerodynamic conditions.

In the third problem the  $C_f$  of RAE2822 airfoil in subsonic conditions was added as target, since it was found that the assimilated parameters caused an overestimation of  $C_f$ . Hence, the latter calculated by elsA has been settled as an input for BIRDIE.

In the fourth one we added as target the velocity profile in the boundary layer of a flat plate in subsonic conditions calculated by elsA with SA standard constants. In fact, important discrepancies were discovered between the theoretical velocity profile and the one obtained with the assimilated coefficients. The input velocity profile of the flat plate calculated with the assimilated coefficients has been imposed as the input for BIRDIE.

### 4.4.1 Optimisation Problem 1

A recapitulative table of the Optimisation Problem 1 is presented in 4.10.

Geometry	C2 airfoil
Grid	Grid 7
Aerodynamic conditions	$Re = 15.7 \cdot 10^6$ , $Ma = 0.724$ and $\alpha = 0.68^\circ$
target $X$	$C_p$ from pETW database, $C_f$ from ISES
vectors to optimise $\tilde{X}$	$C_p$ from elsA, $C_f$ from elsA
parameters to optimise $\tilde{\Theta}$	different combinations of SA turbulence model constants

Table 4.10: Optimisation Problem 1 synthesis

#### 4.4.1.1 Convergence Criterion

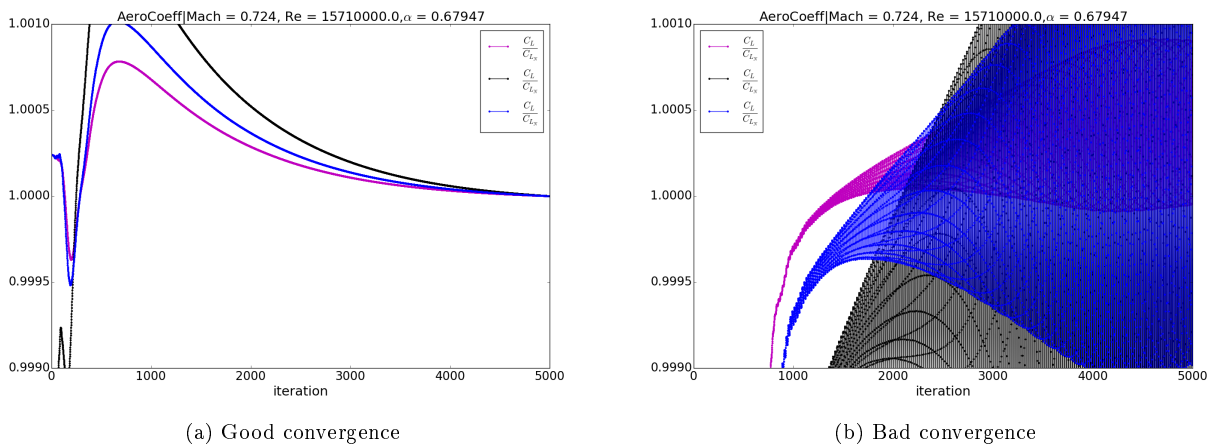


Figure 4.18: Instances of good and bad convergence results

In figure 4.18, instances of good and bad convergence obtained during the data assimilation are shown. On the left, the aerodynamic coefficients that vary less than 0.1 % over temporal iterations are shown, while on the right the trend of these coefficients in case of divergent solution.

In table 4.11, the results on the convergence of the different previously defined sets are summarised. These results do not refer to all the simulations, since there were cases where some combinations of coefficients converged and other diverged, throughout the same assimilation. Instead, it is the convergence of the simulation

performed with the optimal result of that set. The optimal results will be shown below. It can be seen from the table that some coefficients are particularly destabilising for the SA model. For instance, "Set3" obtained convergent results whilst adding  $c_{w2}$  to this set (and then "Set4"), divergent ones. Curiously it can be seen that  $c_{b1}$  and  $c_{b2}$ , if optimised individually, obtain convergent results, but divergent results if optimised in pair. However, to comment about the interrelations on convergence trends between the various constants of the SA model is quite complicated considering the non-linear phenomena involved.

Name	$\tilde{\Theta}$	Converged Results?
Set1	$c_{v1}, c_{w2}, c_{w3}$	No
Set2	$c_{b1}, c_{b2}, \sigma_P$	No
Set3	$c_{b1}, c_{b2}, c_{v1}$	Yes
Set4	$c_{b1}, c_{b2}, c_{v1}, c_{w2}$	No
Set5	$c_{b1}$	Yes
Set6	$c_{b2}$	Yes
Set7	$c_{v1}$	Yes
Set8	$c_{b1}, c_{b2}$	No
Set9	$c_{b1}, c_{b2}, c_{w3}$	No

Table 4.11: Convergence results of the SA coefficient combinations

#### 4.4.1.2 Results

Table 4.13 shows the results of the data assimilation. The leftmost column shows the data assimilation name and the parameters used, the central column the standard values of the paramaters before the optimisation with the corresponding  $\sigma$  value (discrepancy metric) and the rightmost column the best combination obtained and the  $\sigma$  resulting from the optimal point found.

Firstly, one can note that the best  $\sigma$  obtained is with Set3, with a value of 0.114. This set had already been assimilated in the preliminary investigations introduced in *Section 2.3.8* and it had brought interesting results. Set2 is the second best case but, unfortunately, had diverging results as well as the third best case, Set4. All the other assimilations, on the other hand, did not achieve such excellent results as those of Set3. In fact, the  $\sigma$  value for all the others data assimilation is around 0.19.

An attempt to find a certain pattern in the variation of the variables is done below.

$c_{b1}$ , which multiplies the turbulent production term in the SA equation, decreased in all cases apart Set9 (which is the one that presented the worst results). In fact, in the best 3 assimilations (set 3,2,4) there is a reduction of this variable by an order of magnitude.

$c_{b2}$ , which multiplies the turbulent diffusion, has a fluctuating trend. In the best assimilation it obtains a value of about 3 times the standard one, in the second one a zero value. Like  $c_{b2}$ ,  $c_{v1}$  has a fluctuating trend.

The destruction term has been intentionally presented in a different table, 4.12, since it was not an assimilated variable but rather a constraint. It also has high fluctuations and has a bigger value for Set3 compared to the standard one. If one wanted to make an attempt to give an interpretation to these values, Set4, the best case, has coefficients that increase turbulent diffusion and destruction while decreasing turbulent production.

	ref	Set2	Set3	Set4	Set5	Set6	Set8	Set9
$c_{w1}$	3.239	1.000	4.522	1.833	2.986	2.306	2.171	3.307

Table 4.12: Destruction term for the assimilated set of SA model parameters

In figure 4.21, a comparison between the pressure and wall friction coefficients distributions obtained with the standard SA parameters (on the left) and those optimised in Set3 data assimilation (on the right) is made. The results of the assimilation are quite satisfactory. The pressure coefficient has greatly improved the position of the shock as well as the distribution upstream of the shock and over the airfoil PS. The  $C_f$  evolution over the airfoil SS rose downstream the shock, approaching the ISES evolution. On the airfoil PS, on the other

hand, the elsA simulation with the optimised parameters overestimates the wall friction in the front part of the profile and then underestimate it in the rear part comparing to ISES results. All considered, the local flow field characteristics are better predicted.

Table 4.14 shows the convergence history of Set3 optimisation. On the left hand side of the table, N represents the iteration step and  $c_{b1}$ ,  $c_{b2}$  and  $c_{v1}$  are the parameters to be optimised.

On the right hand side different discrepancy metric ( $\sigma$ ) values are represented with respect to different vectors. Total target represents  $\sigma$  values computed between the target  $X$  ( $C_p$  from pETW and  $C_f$  from ISES) and the vectors to be optimised  $\tilde{X}$  ( $C_p$  and  $C_f$  from elsA) corresponding to the set of parameters in the same row. The same has been done for the distribution of the pressure coefficient on the pressure side ( $C_p$  PS), suction side ( $C_p$  SS) and on the whole profile ( $C_p$ ) as well as for the skin friction distribution ( $C_f$  PS,  $C_f$  SS and  $C_f$ ). The columns related to the calculation of  $\sigma$  with respect to the total target, the pressure coefficient and skin friction coefficient were colour-formatted for ease of reading. The larger the bar, the more distant the target and the BIRDIE inputs are and vice versa.

The first 4 rows represents the BIRDIE initialisation. In fact, it is necessary to provide BIRDIE with the vector to be optimised for the standard values of  $\tilde{\Theta}$  and the vector corresponding to the variation of each single parameter contained in  $\tilde{\Theta}$ , as already introduced in *Section 3.2*.

BIRDIE achieved a fairly smooth optimisation, with large variations in the first iterations and small ones in the final ones. One interesting thing to note is at iteration number 12. For this iteration,  $\sigma$  with respect to  $C_p$  is quite low (then good agreement with the experimental data) but the constraint of having the friction coefficient of ISES as the second target, which has a large  $\sigma$  in this iteration, pushes BIRDIE to look for another optimal point. A similar thing happens at iteration number 24.

In figure 4.20 are shown the results obtained from Set5, Set6 and Set7 data assimilations. No satisfactory results have been obtained for these assimilations.

As a result of this exercise, Set3 will be use to carry out the next assimilations.

Set	Constants	Reference SA		After Optimisation	
		Constant Values	$\sigma$	Constant Values	$\sigma$
1	$c_{v1}, c_{w2}, c_{w3}$	7.1, 0.3, 2.0	0.205	6.739, 0.390, 4.997	0.189
2	$c_{b1}, c_{b2}, \sigma_P$	0.1355, 0.622, 0.666	0.205	0.061, 0.441, 2.263	0.151
3	$c_{b1}, c_{b2}, c_{v1}$	0.1355, 0.622, 7.1	0.205	0.077, 1.709, 3.921	0.114
4	$c_{b1}, c_{b2}, c_{v1}, c_{w2}$	0.1355, 0.622, 0.666, 0.3	0.205	0.056, 0.000, 7.394, 2.108	0.149
5	$c_{b1}$	0.1355	0.205	0.093	0.196
6	$c_{b2}$	0.622	0.205	0	0.195
7	$c_{v1}$	7.1	0.205	5.11	0.180
8	$c_{b1}, c_{b2}$	0.1355, 0.622	0.205	0.105, 0.031	0.187
9	$c_{b1}, c_{b2}, c_{w3}$	0.1355, 0.622, 2.0	0.205	0.147, 0.000, 10.680	0.196

Table 4.13: Data assimilations results

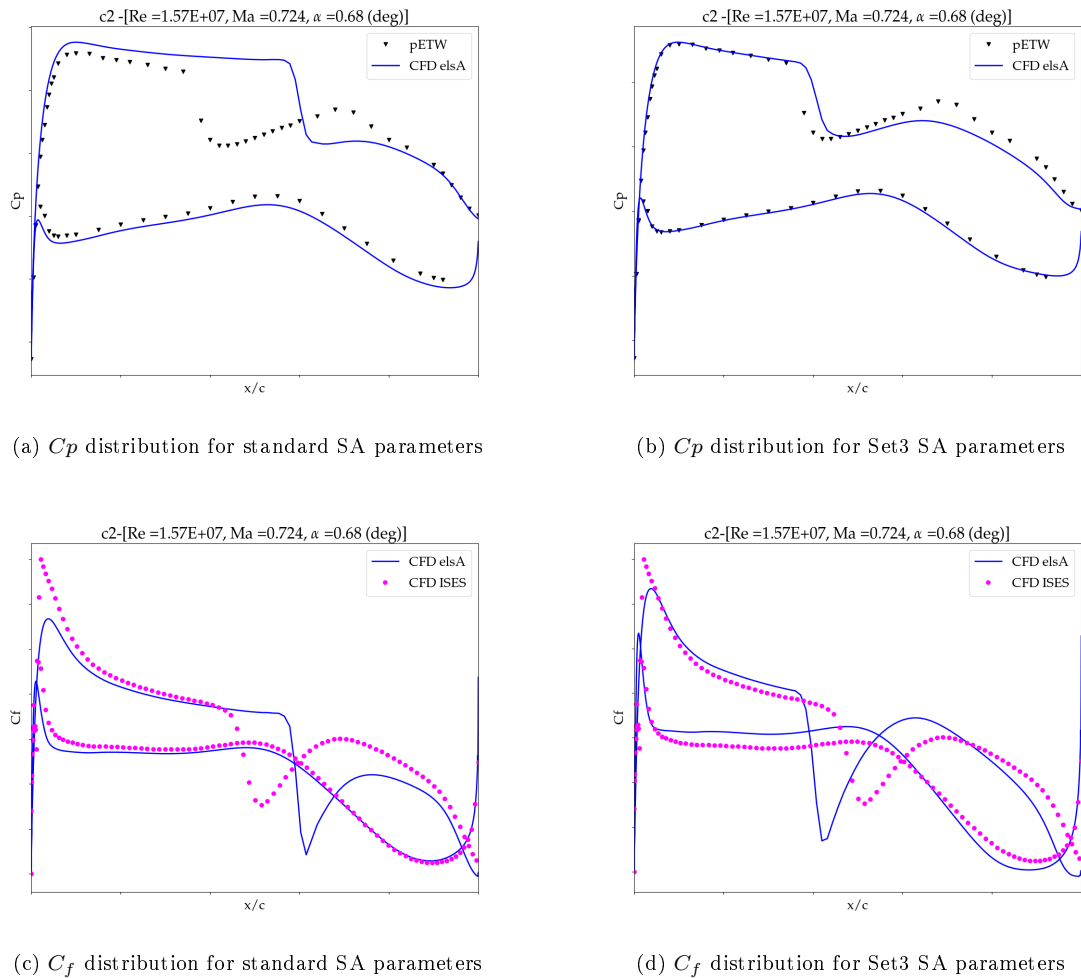


Figure 4.19: Comparison between  $C_p$  and  $C_f$  distributions obtained with SA standard coefficients and with assimilated ones in Set3

N					$\sigma$							
	cb1	cb2	cv1	Totatl target	Cp PS	Cp SS	Cp	Cf PS	Cf SS	Cf		
1	0.136	0.622	7.100	0.205	0.076	0.320	0.257	0.080	0.159	0.135		
2	0.169	0.622	7.100	0.211	0.085	0.340	0.274	0.084	0.134	0.118		
3	0.136	0.778	7.100	0.207	0.077	0.324	0.260	0.080	0.158	0.134		
4	0.136	0.622	8.875	0.242	0.086	0.343	0.276	0.102	0.243	0.202		
5	0.152	0.031	6.395	0.188	0.076	0.298	0.240	0.095	0.125	0.115		
6	0.136	0.378	5.834	0.180	0.072	0.283	0.228	0.104	0.121	0.115		
7	0.021	2.957	2.290	0.418	0.277	0.384	0.348	0.318	0.552	0.478		
8	0.105	1.203	5.440	0.165	0.062	0.249	0.200	0.100	0.131	0.120		
9	0.108	1.105	5.395	0.166	0.063	0.251	0.202	0.103	0.127	0.119		
10	0.122	0.720	5.526	0.174	0.067	0.268	0.216	0.107	0.122	0.117		
11	0.089	1.620	5.197	0.151	0.054	0.211	0.170	0.099	0.145	0.130		
12	0.084	1.701	4.894	0.141	0.050	0.186	0.150	0.106	0.144	0.131		
13	0.145	0.000	5.159	0.173	0.065	0.257	0.207	0.135	0.128	0.131		
14	0.098	1.254	4.627	0.147	0.053	0.205	0.165	0.126	0.127	0.126		
15	0.109	0.855	4.227	0.156	0.053	0.204	0.165	0.155	0.142	0.147		
16	0.048	3.035	6.700	0.220	0.045	0.094	0.079	0.140	0.365	0.301		
17	0.075	1.865	4.365	0.120	0.045	0.121	0.100	0.118	0.146	0.137		
18	0.076	1.796	4.148	0.116	0.044	0.112	0.093	0.128	0.140	0.135		
19	0.076	1.796	4.148	0.116	0.044	0.112	0.093	0.128	0.140	0.135		
20	0.077	1.716	3.890	0.114	0.044	0.101	0.084	0.141	0.136	0.138		
21	0.077	1.716	3.890	0.114	0.044	0.101	0.084	0.141	0.136	0.138		
22	0.075	1.828	4.247	0.117	0.044	0.116	0.096	0.124	0.142	0.136		
23	0.077	1.708	3.867	0.114	0.044	0.100	0.084	0.142	0.136	0.138		
24	0.077	1.708	3.867	0.114	0.044	0.100	0.084	0.142	0.136	0.138		
25	0.077	1.708	3.872	0.114	0.044	0.100	0.084	0.142	0.136	0.138		
26	0.077	1.708	3.872	0.114	0.044	0.100	0.084	0.142	0.136	0.138		
27	0.057	1.708	4.517	0.168	0.054	0.086	0.075	0.112	0.272	0.225		
28	0.077	1.709	3.922	0.114	0.044	0.102	0.085	0.139	0.136	0.137		
29	0.077	1.709	3.921	0.114	0.044	0.102	0.085	0.139	0.136	0.137		

Table 4.14: Convergence history of Set3 optimisation. Parameters value are on the leftmost column, discrepancy metric on the right one.

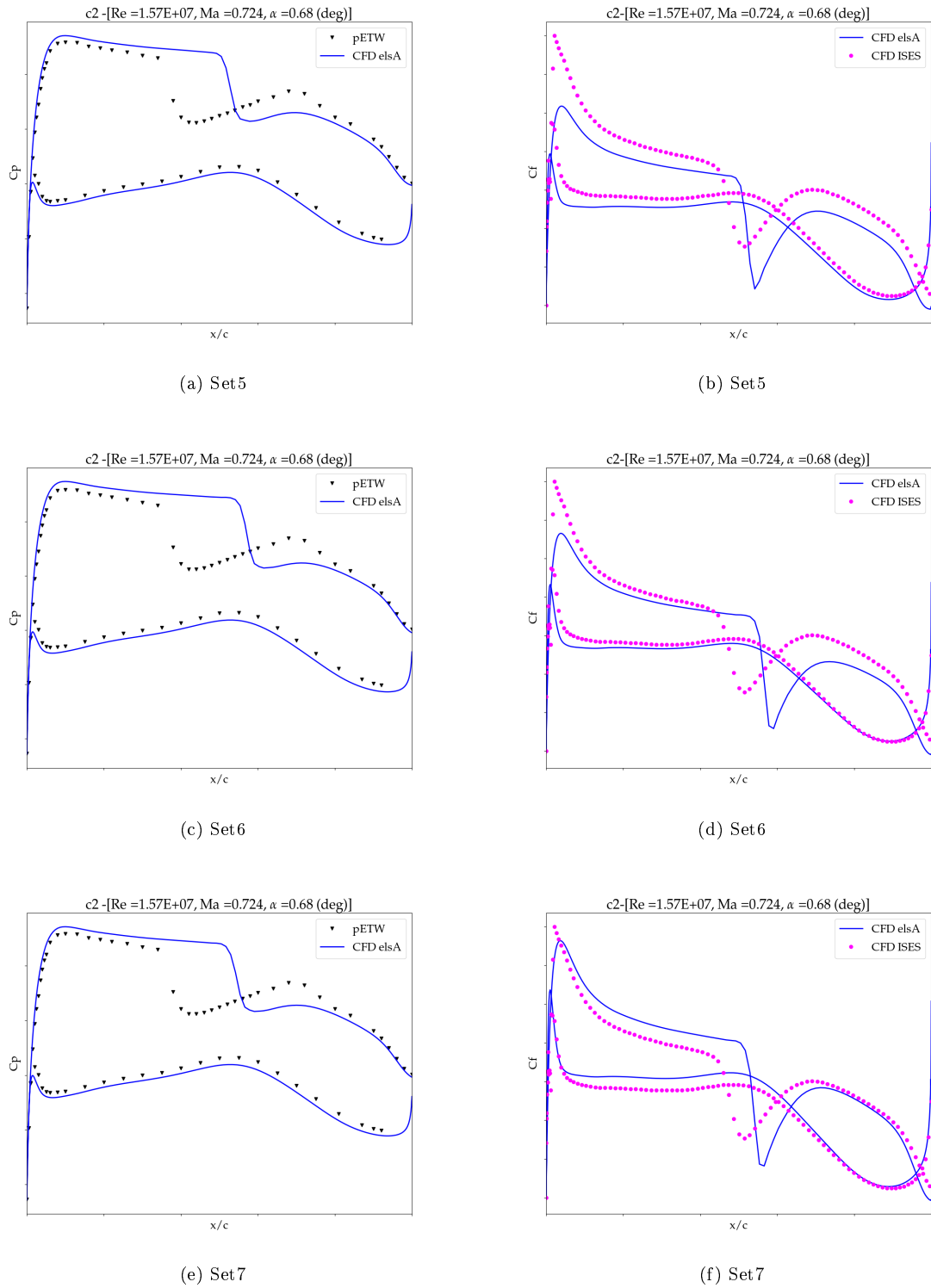


Figure 4.20:  $C_p$  and  $C_f$  distributions obtained with assimilated SA coefficients in Set5, Set6 and Set7

## 4.4.2 Optimisation Problem 2

### 4.4.2.1 Introduction

This section presents the results obtained from the application of the method described in *Section 3.5.3*.

Two different geometries at a variety of aerodynamic conditions have been assimilated through the method described in Optimisation Problem 1. The effects of  $\alpha$ , Mach number and Reynolds number on the Spalart Allmaras model coefficients and the discrepancy metric  $\sigma$  have been studied. For the sake of brevity, not all flowfield characteristics will be depicted in this section, but we will rely on the  $\sigma$  trend, which has shown to be a reliable tool for analysis.

### 4.4.2.2 Results

In table 4.16, the results of this exercise are shown. In the leftmost column the name of the assimilation can be found. Centre-left one shows the aerodynamic conditions and the type of profile, centre-right shows the  $\sigma$  result with respect to the total target (TT) obtained with the standard constants of the SA model. The Rightmost one shows the values of the assimilated parameters and the relative  $\sigma$  calculated with respect to the total target.

We recall the standard values of the SA constants:  $c_{b1} = 0.1355$ ,  $c_{b2} = 0.622$ , and  $c_{v1} = 7.1$ .

In general, all simulations improved the  $C_p$  and  $C_f$  distributions. The largest difference between  $\sigma$  values, and thus the best optimisation, is for assimilation 4, while the second is assimilation 2.

It can be seen that in this case  $c_{b1}$  does not vary as much as it did in the assimilation of the previous problem. In fact, it always remains in the order of 0.1.  $c_{b2}$  decreases in all assimilations, except for 6, most of the cases reaching a zero value. The reason of this behaviour is presented hereafter. It has been imposed to BIRDIE that this parameter must be between 0 and 100. If this had not been the case, BIRDIE would have looked for the optimum point with negative  $c_{b2}$  values. This lower limit was imposed because the modified version of elsA, that permit to vary the constants of the SA model, does not accept negative  $c_{b2}$  values, even though the physical limit detailed by Spalart and Allmaras in the original article is -1. The value of  $c_{v1}$  tends to decrease, up to a maximum of 2 units for the best assimilation obtained. The destruction term, whose trend is described in table 4.15, decreases for all assimilations, excepting Assimilation6 .

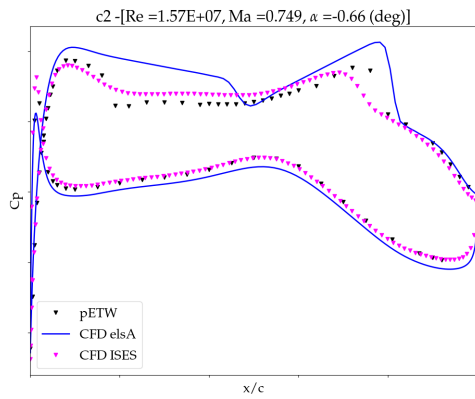
The figure shows the distribution of  $C_p$  and  $C_f$  for the best results, compared with those obtained with the standard SA constants. A general improvement of  $C_p$  distribution can be noted, in the same manner as in the previous section. In fact, the minimum  $C_p$ , the distribution over the PS and the position of the shock are closer to the experimental data. The  $C_f$  evolution over the airfoil is similar enough the one calculated with ISES. Conclusively, while assimilation4 achieved excellent results, the others have obtained marginal ones.

	ref	Ass1	Ass2	Ass3	Ass4	Ass5	Ass6	Ass7
$c_{w1}$	3.24	2.36	2.33	2.37	2.43	2.48	3.86	2.53

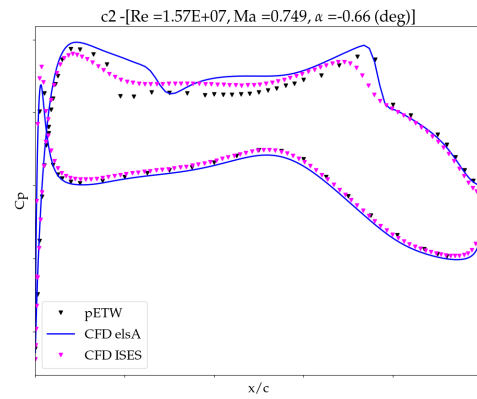
Table 4.15: Destruction term for the different assimilations

Name	Geometry e Aerodynamic Conditions				Standard SA	Assimilated SA			
	Airfoil	$Re \cdot 10^6$	$M_a$	$\alpha^\circ$	$\sigma_{TT}$	$c_{b1}$	$c_{b2}$	$c_{v1}$	$\sigma_{TT}$
assimilation1	C2	15.7	0.724	-1.87	0.136	0.144	0.000	6.905	0.126
assimilation2	C2	11.8	0.505	2.15	0.180	0.139	0.000	5.622	0.162
assimilation3	C2	9.0	0.745	0.79	0.161	0.146	0.000	7.122	0.152
assimilation4	C2	15.7	0.749	-0.66	0.136	0.109	0.184	5.740	0.087
assimilation5	EFT	15.6	0.727	1.09	0.127	0.164	0.000	6.517	0.118
assimilation6	EFT	15.6	0.747	0.98	0.166	0.106	1.153	6.195	0.157
assimilation7	EFT	8.9	0.747	0.98	0.173	0.173	0.000	7.012	0.168

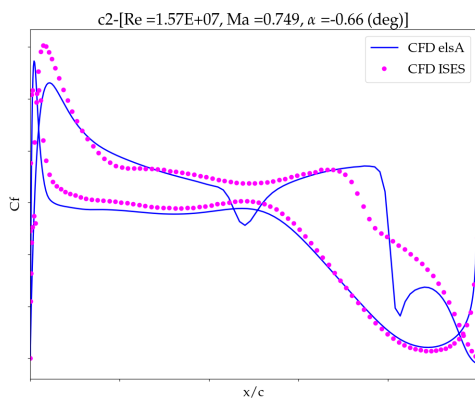
Table 4.16: Data assimilation results of Optimisation Problem 2



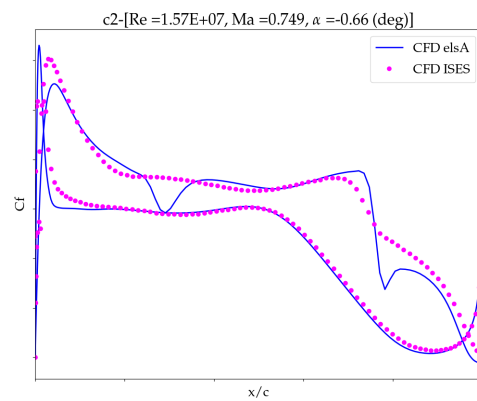
(a)  $C_p$  distribution for standard SA parameters



(b)  $C_p$  distribution for Assimilation4 SA parameters



(c)  $C_f$  distribution for standard SA parameters



(d)  $C_f$  distribution for Assimilation4 SA parameters

Figure 4.21: Comparison between  $C_p$  and  $C_f$  distributions obtained with SA standard coefficients and with assimilated ones in Assimilation4

### 4.4.3 Optimisation Problem 3

#### 4.4.3.1 Introduction

In this section, the results obtained in Optimisation problem 3 will be described. The followed procedure is described in *Section 3.5.4*. The coefficients found in Optimisation problem 1 have been used to perform a simulation of RAE2822 profile in subsonic conditions, to analyse its flowfield and boundary layer properties. A large discrepancy between the skin friction coefficient calculated for standard and assimilated constants has been found. The two curves are shown in fig 4.22. It has been decided to add to the target and input vectors of BIRDIE, the  $C_f$  distribution calculated on RAE under these conditions with the standard constants of SA model and with those assimilated constants, respectively.

A synthesis of the optimisation problem is presented in table 4.17.

Geometry	C2 airfoil	RAE2822
Grid	Grid7	Grid 7
Aerodynamic conditions	$Re = 15.7 \cdot 10^6$ , $Ma = 0.724$ and $\alpha = 0.68^\circ$	$Re = 3.57 \cdot 10^6$ , $Ma = 0.246$ and $\alpha = 2.65^\circ$
target $X$	$C_p$ from pETW database, $C_f$ from ISES	$C_f$ from elsA with standard SA constants
vectors to optimise $\tilde{X}$	$C_p$ from elsA, $C_f$ from elsA	$C_f$ from elsA
parameters to optimise $\tilde{\Theta}$	$c_{b1}, c_{b2}, c_{v1}$	$c_{b1}, c_{b2}, c_{v1}$

Table 4.17: Optimisation Problem 3 synthesis

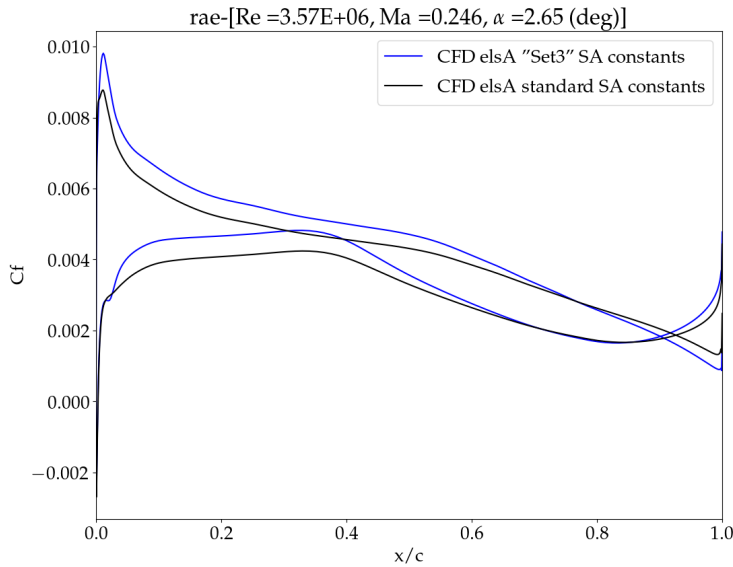


Figure 4.22: Discrepancy between  $C_f$  calculated with SA standard constants and with those assimilated in Set3 for RAE2822 airfoil

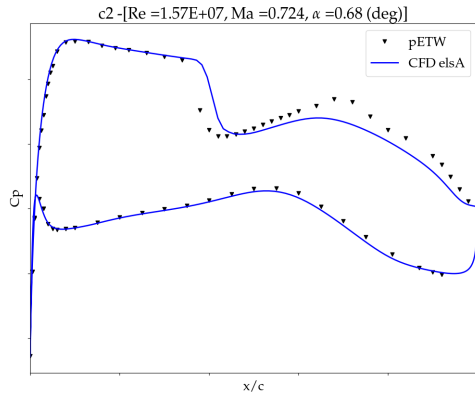
#### 4.4.3.2 Results

The table 4.18 shows the convergence history calculated from this exercise. A similar table was shown in *Section 4.4.1*. On the left side, the iteration number  $N$  and the variation of the assimilated coefficients  $c_{b1}$ ,  $c_{b2}$ ,  $c_{v1}$  are shown. On the right side, the calculation of  $\sigma$  with respect to 4 different vectors: the total target (distribution of  $C_p$  along C2,  $C_f$  along C2 and  $C_f$  along RAE2822), and each contribution of the total target considered individually. The cells have been coloured to make them easier to read.

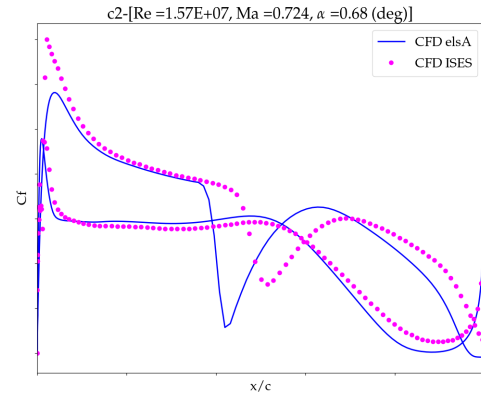
The first row of the table shows the results for the standard constants and the last row shows the results for the optimum point. Through  $\sigma$  values analysis, a significant improvement of the pressure coefficient distribution, a wall friction coefficient one that remains about constant for C2 and quite low for RAE can be noted. These three distributions, calculated with the optimal SA parameters, are shown in fig. 4.23.

N				$\sigma$			
	cb1	cb2	cv1	Total target	Cp C2	Cf C2	Cf RAE
	0.136	0.622	7.100	0.168	0.257	0.135	0.000
	0.169	0.622	7.100	0.176	0.274	0.118	0.065
	0.136	0.778	7.100	0.169	0.260	0.134	0.004
	0.136	0.622	8.875	0.214	0.276	0.202	0.141
0	0.152	0.031	6.395	0.159	0.240	0.115	0.073
1	0.136	0.378	5.834	0.160	0.228	0.115	0.107
2	0.021	2.957	2.290	0.493	0.348	0.478	0.617
3	0.105	1.203	5.440	0.142	0.200	0.120	0.077
4	0.108	1.105	5.395	0.145	0.202	0.119	0.090
5	0.122	0.720	5.526	0.156	0.216	0.117	0.112
6	0.089	1.620	5.197	0.127	0.170	0.130	0.049
7	0.084	1.701	4.894	0.120	0.150	0.131	0.058
8	0.145	0.000	5.159	0.176	0.207	0.131	0.181
9	0.098	1.254	4.627	0.143	0.165	0.126	0.135
10	0.109	0.855	4.227	0.177	0.165	0.147	0.214
11	0.048	3.035	6.700	0.265	0.079	0.301	0.337
12	0.075	1.865	4.365	0.106	0.100	0.137	0.071
13	0.076	1.796	4.148	0.109	0.093	0.135	0.093
14	0.076	1.796	4.148	0.109	0.093	0.135	0.093
15	0.077	1.716	3.890	0.117	0.084	0.138	0.123
16	0.077	1.716	3.890	0.117	0.084	0.138	0.123
17	0.075	1.828	4.247	0.107	0.096	0.136	0.083
18	0.077	1.708	3.867	0.118	0.084	0.138	0.125
19	0.077	1.708	3.867	0.118	0.084	0.138	0.125
20	0.077	1.708	3.867	0.118	0.084	0.138	0.125
21	0.077	1.708	3.872	0.118	0.084	0.138	0.125
22	0.077	1.708	3.872	0.118	0.084	0.138	0.125
23	0.057	1.708	4.517	0.163	0.075	0.225	0.153
24	0.077	1.709	3.922	0.116	0.085	0.137	0.119
25	0.077	1.709	3.921	0.116	0.085	0.137	0.119
26	0.000	1.774	21.666	0.760	0.297	0.832	0.977
27	0.077	1.709	3.924	0.116	0.085	0.137	0.118
28	0.077	1.709	3.924	0.116	0.085	0.137	0.118
29	0.069	0.921	100.000	0.689	0.255	0.731	0.908
30	0.077	1.708	4.070	0.111	0.090	0.136	0.103
31	0.077	1.708	4.086	0.111	0.090	0.136	0.100
32	0.070	1.722	4.557	0.104	0.085	0.148	0.061

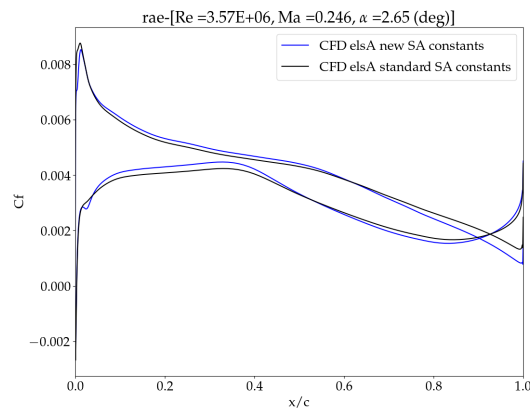
Table 4.18: Convergence history of Optimisation Problem 3



(a)  $C_p$  of C2 airfoil



(b)  $C_f$  of C2 airfoil



(c)  $C_f$  of RAE2822 airfoil

Figure 4.23: Pressure coefficient and skin friction distribution relative to the optimised parameters

## 4.4.4 Optimisation Problem 4

### 4.4.4.1 Introduction

The results obtained by applying the procedure described in 3.5.5 are here detailed.

First the influences of the parameters through Optimisation Problem 1 (OP1) and Optimisation Problem 3 (OP3) on the flowfield and boundary layer characteristics of a flat plate simulation will be described. Hence the results obtained from the optimization process will be introduced.

It is recalled that this Optimisation Problem 4 corresponds to the previous one with the addition of a target, and therefore an additional vector to be optimised. The target is the velocity profile of the flat plate calculated with the standard SA coefficients, while the BIRDIE input is the latter calculated with the parameters to be optimised. A summary of the optimisation problem is presented in table 4.19.

Geometry	C2 airfoil	RAE2822 airfoil	Flat Plate
Grid	Grid7	Grid 7	$258 \times 33 \times 2$
Aerodynamic conditions	$Re = 15.7 \cdot 10^6$ , $M_a = 0.724$ and $\alpha = 0.68^\circ$	$Re = 3.57 \cdot 10^6$ , $M_a = 0.246$ and $\alpha = 0.0^\circ$	$Re = 5.0 \cdot 10^6$ , $M_a = 0.2$ and $\alpha = 0.0^\circ$
target $X$	$C_p$ from pETW database , $C_f$ from ISES	$C_f$ from elsA with standard SA constants	$U^+$ at $x = 0.97$ from elsA with standard SA constants
vectors to optimise $\tilde{X}$	$C_p$ from elsA, $C_f$ from elsA	$C_f$ from elsA	$U^+$ at $x = 0.97$ from elsA with non-standard SA constants
parameters to optimise $\tilde{\Theta}$	$c_{b1}, c_{b2}, c_{v1}$	$c_{b1}, c_{b2}, c_{v1}$	$c_{b1}, c_{b2}, c_{v1}$

Table 4.19: Optimisation Problem 4 synthesis

### 4.4.4.2 Assimilated Parameters Effects on Flate Plate Simulations

The coefficients obtained in OP1 ( $c_{b1} = 0.077$ ,  $c_{b2} = 1.709$ , and  $c_{v1} = 3.921$ ) and OP3 ( $c_{b1} = 0.070$ ,  $c_{b2} = 1.722$ , and  $c_{v1} = 4.557$ ) were used to perform simulations on a NASA flat plate under subsonic conditions and compare with the standard constants of the SA model.

Figure 4.24 shows the results obtained from the simulation performed with the standard constants of the SA model, figure 4.25 with the constants obtained from OP1 and figure 4.26 obtained from optimisation problem 3.

For all the figures are shown:

- the trend of the momentum thickness  $\theta$  as a function of the axial coordinate  $x$  (top-left);
- the velocity profile  $U$  (in linear scale) normalised with the outer velocity  $U_e$  in relation with the wall normal axis  $y$  normalised with the BL thickness  $\delta$  at  $x = 0.97$  and  $x = 1.97$  (top-right);
- the non dimensional velocity  $U^+$  (x-axis) in relation with the  $\log_{10}(y^+)$  (y-axis) (bottom left);
- the skin friction coefficient  $C_f$  as a function of  $x$  (bottom-right).

In addition, the momentum thickness is compared with the one calculated with standard correlations. The velocity profiles, both in linear and logarithmic scale, are compared with the results obtained from the NASA simulation and/or the theoretical profile. The theoretical profile was extracted from [4]. Finally, the wall friction coefficient is also compared with the NASA results and standard correlations. All the correlations are taken from the lectures of Eric Goncalves in [23].

Concerning the results obtained with standard SA constants, elsA finds results very similar to other references. The momentum thickness (fig. 4.24a) and velocity profiles (fig. 4.24b and 4.24c) are almost superimposed. The elsA friction coefficient (fig. 4.25d) is slightly overestimated compared to the NASA one and quite similar compared to the experimental correlation.

The results obtained with elsA simulation using the OP1 parameters are quite different from those described above. The momentum thickness (fig 4.25a) is much higher than the previous results. The velocity trend is significantly dissimilar to NASA and theoretical one, in fig.4.25b and 4.25c. The friction coefficient (fig. 4.24d) is

considerably overestimated compared to NASA and correlations results, by around 15%. The same trend can be noted in the results obtained with the OP3 parameters. However, a smaller discrepancy between the elsA results and the references curves is found.

One can note that both sets of the assimilated coefficients increase  $C_f$  distribution. This was also found for the RAE2822 profile results for the simulations performed with OP1 coefficients. Very interesting is instead their influence on the boundary layer. The  $U^+$  evolution in fig. 4.25c and fig. 4.26c reminds of the effects of the adverse pressure gradient on the latter, whereas the flow is under uniform conditions.

A plausible explanation to this phenomenon may be the following.

SA turbulence model struggles in taking into account the adverse pressure gradient for simulations of aft-cambered profiles in transonic conditions. Through two data assimilations, the parameters obtained can better reproduce these effects when the adverse pressure gradient is strong. However, the effect of the latter is kept even when this is absent, as in the tested flat plate with uniform flow. In support of this thesis, the shift downward of the non-dimensional velocity within the buffer layer and its larger slope in the outer layer are typical effects of the adverse pressure gradient, as demonstrated in [16].

However, further verifications are necessary to confirm this hypothesis.

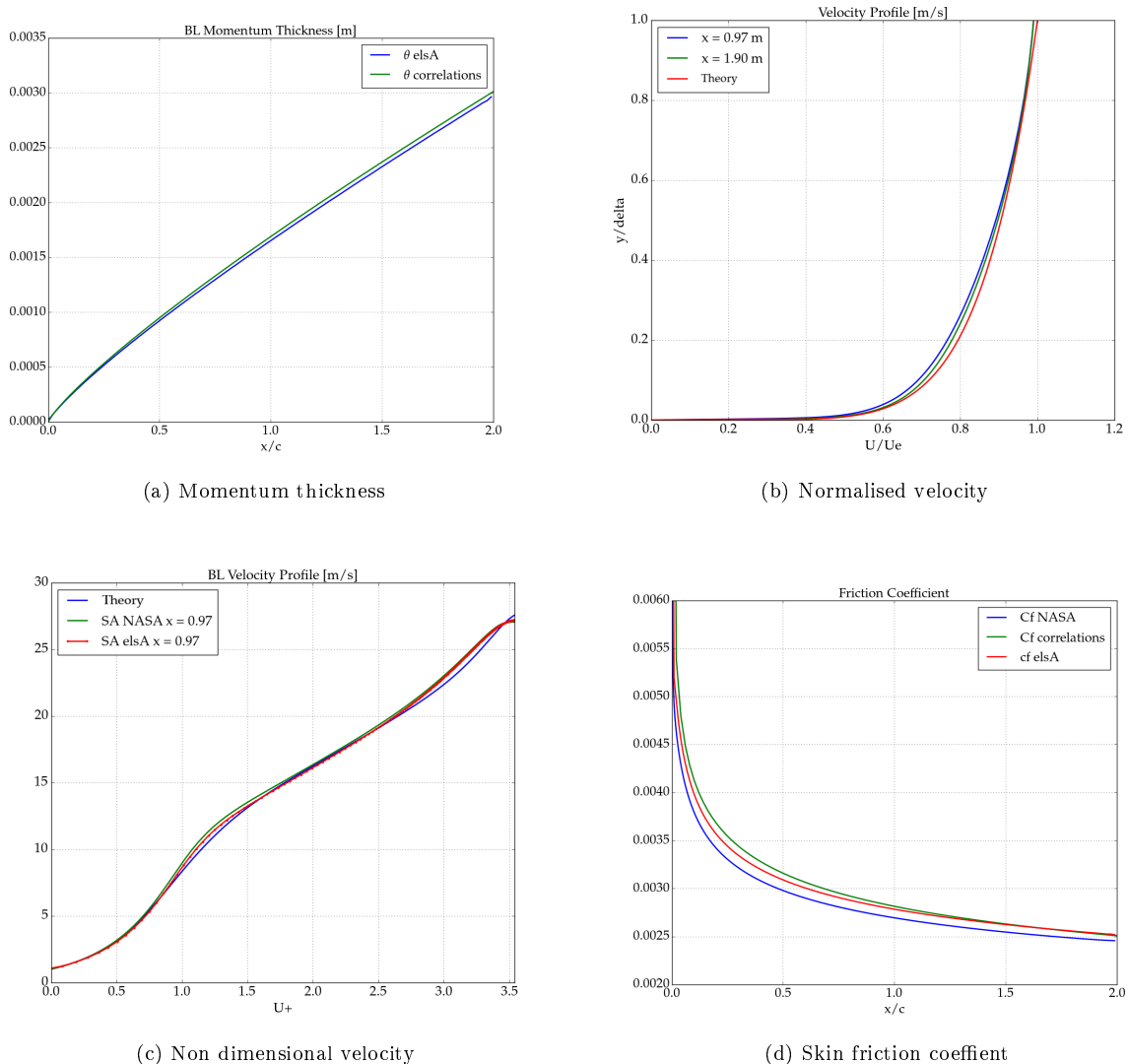
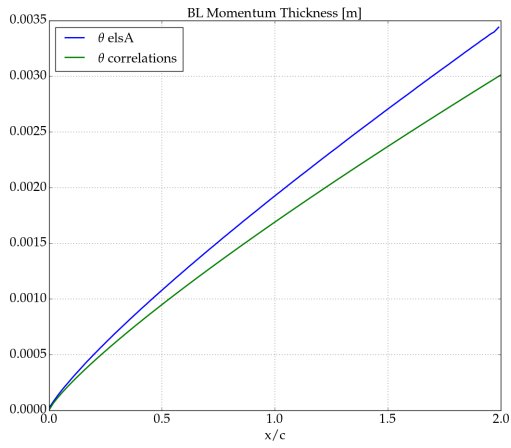
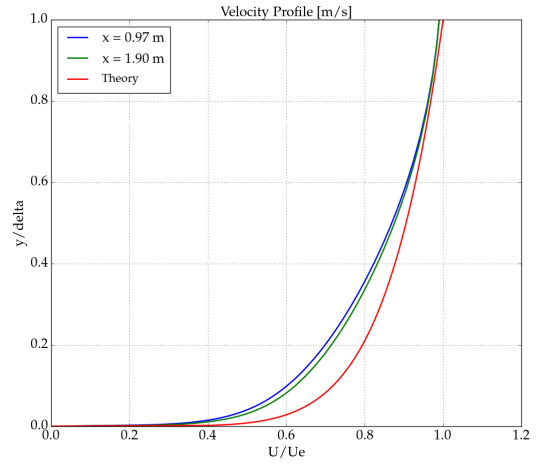


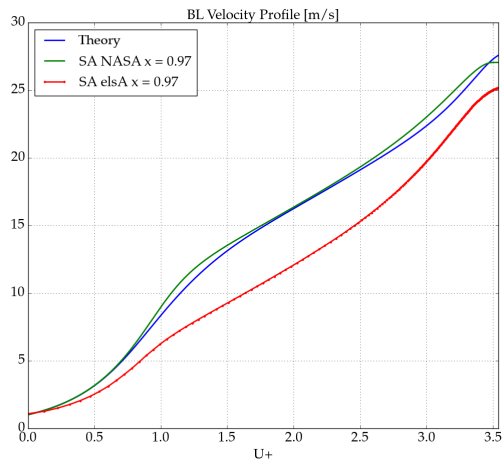
Figure 4.24: Simulations results obtained with SA standard parameters



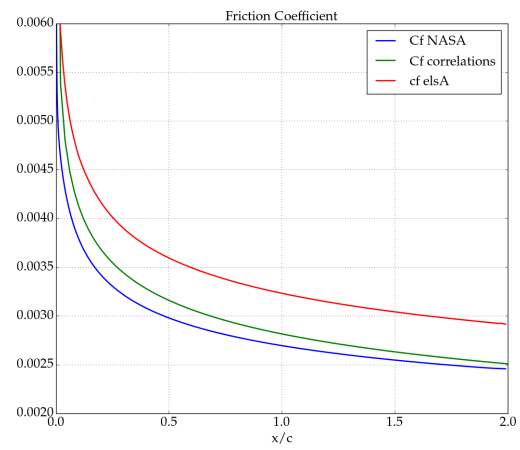
(a) Momentum thickness



(b) Normalised velocity



(c) Non dimensional velocity



(d) Skin friction coefficient

Figure 4.25: Simulations results obtained with SA standard parameters

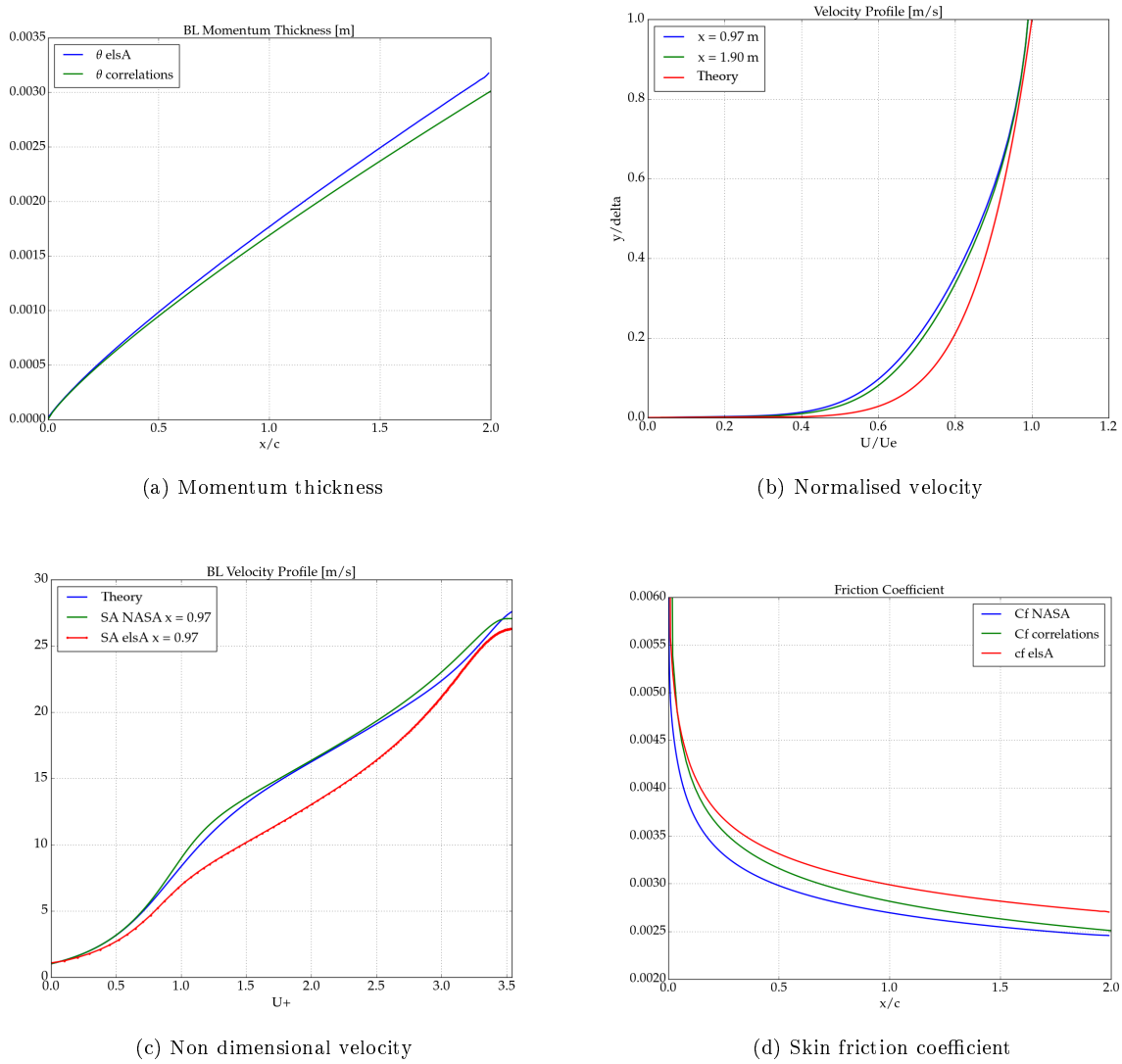


Figure 4.26: Simulations results obtained with SA standard parameters

#### 4.4.4.3 Results

Unfortunately, Optimisation Problem 4 did not obtain satisfactory results and further investigations were not carried out due to time constraints. In fact, the coefficient  $c_{b2}$  reached the zero value after a few iterations, as it happened several times for OP2 and OP3. The convergence history is shown in figure 4.20

<b>N</b>	<b>cb1</b>	<b>cb2</b>	<b>cv1</b>	<b><math>\sigma_{TT}</math></b>
	0.136	0.622	7.100	0.168
	0.169	0.622	7.100	0.176
	0.136	0.778	7.100	0.169
	0.136	0.622	8.875	0.214
0	0.145	0.031	7.121	0.162
1	0.149	0.031	7.136	0.163
2	0.145	0.000	7.119	0.162
3	0.145	0.000	7.119	0.162
4	0.145	0.000	7.119	0.162

Table 4.20: Convergence history of Optimisation Problem 4

### 4.4.5 Conclusion

The aim of this section has been to assimilate, via to BIRDIE code, the constants of the SA model in order to improve the prediction capabilities of elsA on C2 profiles under transonic conditions. In addition, tests about the effects of new assimilated constants on other academic flows have been carried out and eventually added to the assimilation. All in all, the data assimilation has achieved good results.

In Optimisation Problem 1 (OP1), the experimental pressure field and the viscous stresses, predicted by ISES cose, around C2 under transonic conditions has been set as the target.

Nine different parameter combinations (the constants of the SA model) were tested, but only three of them had tangible improvements on the pressure field. From these three, only one had convergent simulations.

One may deduce that the parameters to be assimilated are quite limited, which reduces the degrees of freedom of the optimisation problem and, consequently, a possible optimal combination of parameters that can reproduce a large range of physical phenomena.

With this set of coefficients, which is  $(c_{b1}, c_{b2}$  and  $c_{v1})$ , the same formulation of OP1 has been performed under a variety of aerodynamic conditions and two airfoil geometries. This formulation has been called Optimisation Problem 2 (OP2).

A total of seven cases were tested, of which only one achieved important improvements. However, one thing needs to be highlighted. For five remaining cases out of six, the optimisation process was not completed due to technical problems concerning the elsA CFD code. In fact, the version utilised does not accept negative values of the **diffusion** term  $c_{b2}$  (its value, according to Spalart-Allmaras article, should be between -1 and 1), but BIRDIE during the optimisation process pointed towards an optimal point with a negative value of this parameter (i.e. as this value decreased, the discrepancy between elsA and the experimental results decreased). The link between APG and a lower, or even negative, turbulent **diffusion** has been detected in [14].

However, the improvements in both OP1 and OP2 were remarkable. The resulting pressure field of elsA is much closer to the experimental one, whilst the friction coefficient has a distribution closer to ISES one.

The set of coefficients of OP1 have been used to perform a simulation on RAE2822 airfoil under subsonic conditions. An overestimation of the skin friction coefficient evolution, compared to the one calculated with standard Spalart-Allmaras constants, has been detected. In light of this, RAE2822 airfoil skin friction coefficient distribution has been added to the previous formulation as a target. In similar vein as above, this process has been called OP3 .

OP3 results have been successful.

In addition, the velocity profile within the boundary layer on a flat plate, under subsonic conditions and calculated with the assimilated coefficients, has been analysed. Through this analysis, similar peculiarities of a velocity profile under adverse pressure gradient have been encountered: a downward shift in the buffer layer and a more pronounced slope in the outer layer, according to [16].

Hence, the velocity profile has been added to the previous target but BIRDIE did not converged for the same reason as before (i.e.  $c_{b2}$  not be able to be negative).

The addition of the velocity profile of a flat plate as a BIRDIE target is certainly an interesting idea that should be tested with other turbulence models.

# Chapter 5

## Conclusion

Recently, a large inconsistency between supercritical airfoil performances extracted from wind tunnel tests and predictions of CFD simulations has been encountered. In light of the crucial interest of predicting profile performance, for instance shape design purposes, an investigation has been previously carried out in ACI group at ONERA. The hypothesis that this discrepancy was due to turbulence models inability to handle an important adverse pressure gradient was made and tested.

Thereafter, assimilations of the SA model constants were made to analyse its effects, with interesting results. On this basis, the objectives of this internship have been to quantify and thoroughly investigate this issue.

A profile, called in the text "Profil\_12", has been designed with the intention of replicating this issue, thus producing contrasting results between diverse CFD codes (in particular between elsA and ISES codes). The airfoil main characteristic is a pronounced aft-camber, comparable to the one of the profiles measured in wind test tunnels. Thanks to a reverse-engineering method, called BIRDIE, and manual adjustments of the airfoil geometry, the previous objective has been achieved, confirming the hypothesis above.

In order to exclude any spurious mesh numerical effects on this issue, a grid convergence exercise was considered imperative. Twelve grids have been utilised and the global (aerodynamic coefficients) and local (pressure and skin-friction coefficient distributions, velocity profiles picked from airfoil wall) results derived from them were compared. In addition, Grid Convergence Index and Far-Field Drag analysis have been performed to select the most appropriate grid. Hence, taking into account accuracy and computational cost, an optimal grid has been selected.

A "reliability" mapping of elsA and ISES capabilities to predict the pressure field around supercritical profiles with strong rear-loading was carried out. Simulations and wind tunnel tests over a suitable range of aerodynamic conditions and for airfoils with variable aft-camber were compared through a discrepancy metric, ad hoc formulated. The results confirmed the prior suspicions and a general inadequacy of CFD codes in predicting performance for rear-loaded airfoils has been detected. Also, this inadequacy worsen with Mach number and angle of attack, while no tangible Reynolds number effects have been detected. In particular, RANS equations solver producing worse results compared to a Euler equation solver coupled with a boundary layer model. In addition, considerations on the properties of the turbulence model, i.e. friction and boundary layer integral quantities, have been carried out.

Furthermore, a data assimilation on the Spalart-Allmaras model constants was attempted. This exercise aims both to improve the predictive capabilities of the model and to investigate how the boundary layer physics varies with the constants of the turbulence model. Several optimisation problems have been formulated and test cases with different physical characteristics have been imposed as the their target.

The pressure field and the viscous stresses around a profile with strong rear loading under transonic conditions for the first two problems. While in the first problem a variety of Spalart-Allmaras parameters have been tested, in the second one diverse aerodynamic regimes and airfoil geometries have been assimilated.

The viscous stress around a more canonical airfoil in subsonic regime has been added to the former formulation. Lastly, a flat plate velocity profile, within the boundary layer thickness, has been integrated to the previous formulation to impose a proper model behaviour without adverse pressure gradient in subsonic conditions.

Simultaneously, considerations of the effects of the assimilated coefficients on the boundary layer properties have been made.

The first three data assimilations yielded several improvements to the flow field. In fact, the numerical pressure field of the aft-cambered profile was significantly closer to the one measured in the wind tunnel, as well as the shear stress had a better agreement with ISES results. However, only a combination of constants produced satisfactory results.

This combination with the values previously assimilated, has been tested on a canonical case, in order to study its effect: a flat plate under subsonic conditions. The velocity profile has been compared to a NASA reference

and discrepancies have been found. In particular, a downward shift in the buffer layer and a more pronounced slope in the outer layer have been observed, which are typical effects of the adverse pressure gradient, as specified in [16].

The velocity profile has been added to the targets of the formulation, not obtaining good results due to a elsA technical problem. In fact, while the optimisation was pointing forward a negative value of the diffusion constant, this elsA version did not accept negative values Spalart-Allmaras constants, causing an interruption of the optimisation. It must be reminded that Spalart and Allmaras, in their original article, indicated as the diffusion constant lower limit a value of -1. Hence, it is suitable in the future to remove this constraint in elsA code.

Further investigations are envisaged by ACI unit at ONERA, through a PhD proposal. The aim is to pursue data assimilations by formulating optimisation problems targeting different canonical cases, which cover a wide variety of flow physical effects, for a reformulation of the RSM turbulent models. Unlike the "one-by-one" calibration of classical turbulence models constants through experimental measurement, which does not take into account the non-linear interrelations between physics phenomena, this approach may cover a wide range of physical situations at once. RSM model has been indicates as a suitable model for this purpose since its wide variety of parameter adds degrees of freedom to the optimisation problem, allowing to model, a priori, a larger variety of fluid phenomena, including strong adverse pressure gradients.

# Bibliography

- [1] D. Bailly, “PR Chyne / Méthode géométrique,” tech. rep., ONERA, 2015.
- [2] M. Carini and J.-L. Hantrais-Gervois, “elsAASO-2017 - CP-2.7 - Validation of transonic performance predictions,” confidential, ONERA, 2018.
- [3] A. Rizzi and H. Viviand, “Numerical methods for the computation of inviscid transonic flows with shock waves,” 1981.
- [4] NASA, “SA Expected Results - 2D Zero Pressure Gradient Flat Plate,” [https://turbmodels.larc.nasa.gov/flatplate\\_sa.html](https://turbmodels.larc.nasa.gov/flatplate_sa.html).
- [5] “Decadal survey of civil aeronautics: Foundation for the future,” *The National Academies Press*, 2006.
- [6] “Flightpath 2050 - europe’s vision for aviation.” Advisory Council for Aviation Research and Innovation in Europe <https://www.acare4europe.org/documents/latest-acare-documents/acare-flightpath-2050>, 2011.
- [7] “Strategic research and innovation agenda 2017 update, volume 1.” Advisory Council for Aviation Research and Innovation in Europe <https://www.acare4europe.org/sria/exec-summary/volume-1>, 2017.
- [8] L. Cambier, S. Heib, and S. Plot, “The onera elsA CFD software: input from research and feedback from industry,” *Mechanics & Industry*, vol. 14, no. 3, pp. 159–174, 2013.
- [9] M. Drela and M. Giles, “Ises-a two-dimensional viscous aerodynamic design and analysis code,” in *25th AIAA Aerospace Sciences Meeting*, p. 424, 1987.
- [10] J. Bailly and Y. Delrieux, “RGC 2017 : Suite PR CHYNE - Influence des paramètres optimaux déterminés par la méthode géométrique BIRDIE sur l’estimation du bruit BVI du rotor BO105 par calculs CFD,” tech. rep., ONERA, 2017.
- [11] P. Spalart and S. Allmaras, “A one-equation turbulence model for aerodynamic flows,” 1992.
- [12] L. Cambier, M. Gazaix, S. Heib, S. Plot, M. Poinot, J. Veillot, J. Boussuge, and M. Montagnac, “An overview of the multi-purpose elsA flow solver,” *AerospaceLab*, no. 2, pp. p–1, 2011.
- [13] F. H. Clauser, “Turbulent boundary layers in adverse pressure gradients,” *Journal of the Aeronautical Sciences*, vol. 21, no. 2, pp. 91–108, 1954.
- [14] P.-Å. Krogstad and P. E. Skåre, “Influence of a strong adverse pressure gradient on the turbulent structure in a boundary layer,” *Physics of Fluids*, vol. 7, no. 8, pp. 2014–2024, 1995.
- [15] J.-H. Lee and H. J. Sung, “Effects of an adverse pressure gradient on a turbulent boundary layer,” *International Journal of Heat and Fluid Flow*, vol. 29, no. 3, pp. 568–578, 2008.
- [16] Á. Tanarro, R. Vinuesa, and P. Schlatter, “Effect of adverse pressure gradients on turbulent wing boundary layers,” *Journal of Fluid Mechanics*, vol. 883, 2020.
- [17] B. Launder and D. Spalding, “The numerical computation of turbulent flows,” *Computer Methods in Applied Mechanics and Engineering*, vol. 3, no. 2, pp. 269–289, 1974.
- [18] M. Carini, J.-L. Hantrais-Gervois, D. Bailly, and P. Bardoux, “ELSA ASO-2020- Task CP-1.2 - On the prediction of transonic airfoil performance against pETW experimental database,” confidential, ONERA, 2020.
- [19] D. Destarac, “ELSA ASO-2015- Task CP-2.10 - Airfoil RANS Computations Good and Bad Practice for Airfoil RANS Computations,” tech. rep., ONERA, 2015.

- [20] T. Sederberg, “Bézier curve.” <http://encyclopediaofmath.org/>, 2006.
- [21] NASA, “Examining spatial (grid) convergence,” 2021.
- [22] C. Benoit, S. Péron, and S. Landier, “Cassiopee: a cfd pre-and post-processing tool,” *Aerospace Science and Technology*, vol. 45, pp. 272–283, 2015.
- [23] E. Goncalves, “Aerodynamique compressible,” 2020.
- [24] J. Slotnick and G. Heller, “Emerging opportunities for predictive cfd for off-design commercial airplane flight characteristics.” Boeing and Airbus report, 2019.